MULTIMODAL MAGNETIC RESONANCE IMAGING PREDICTS REGIONAL AMYLOID BURDEN IN THE BRAIN: A PATTERN RECOGNITION APPROACH TO AMYLOID PREDICTION

by

Anusha Alathur Rangarajan

B.E. Biomedical Engineering, Anna University, 2012

M.S. Biomedical Engineering, Carnegie Mellon University, 2014

Submitted to the Graduate Faculty of

Swanson School of Engineering in partial fulfillment

of the requirements for the degree of

Doctor of Philosophy

University of Pittsburgh

2019

UNIVERSITY OF PITTSBURGH

SWANSON SCHOOL OF ENGINEERING

This dissertation was presented

by

Anusha Alathur Rangarajan

It was defended on

March 18, 2019

and approved by

Charles Laymon, PhD, Assistant Professor,
Departments of Radiology and Bioengineering

George Stetten, MD, PhD, Professor,
Department of Bioengineering

Kim Kang, PhD, Associate Professor,
Departments of Medicine and Bioengineering

Dissertation Director: Howard Aizenstein, MD, PhD, Chair and Professor of Geriatric Psychiatry
Department of Psychiatry and Professor, Department of Bioengineering

MULTIMODAL MAGNETIC RESONANCE IMAGING PREDICTS REGIONAL AMYLOID BURDEN IN THE BRAIN: A PATTERN RECOGNITION APPROACH TO AMYLOID PREDICTION

Anusha Alathur Rangarajan, Ph.D.

University of Pittsburgh, 2019

Alzheimer's disease (AD) is the most common cause of dementia and identifying early markers of this disease is important for prevention and treatment strategies. Amyloid- β ($A\beta$) protein deposition is one of the earliest detectable pathological changes in AD. But in-vivo detection of $A\beta$ using positron emission tomography (PET) is hampered by high cost and limited geographical accessibility. These factors can become limiting when PET is used to screen large numbers of subjects into prevention trials when only a minority are expected to be amyloid-positive. Structural MRI is advantageous; as it is non-invasive, relatively inexpensive and more accessible. Thus it could be widely used in large studies, even when frequent or repetitive imaging is necessary. We used a machine learning, pattern recognition, approach using intensity-based features from individual and combination of MR modalities (T1 weighted, T2 weighted, T2 fluid attenuated inversion recovery [FLAIR], susceptibility weighted imaging) to predict voxel-level amyloid in the brain. The MR- $A\beta$ relation was learned within each subject and generalized across subjects using subject–specific features (demographic, clinical, and summary MR features). When compared to other modalities, combination of T1-weighted, T2-weighted FLAIR, and SWI performed best in predicting the amyloid status as positive or negative. A combination of T2-weighted and SWI imaging performed the best in predicting change in amyloid over two timepoints. Overall, our results show feasibility of amyloid prediction by MRI and its potential use as an amyloid-screening tool for tracking AD. In addition to the amyloid prediction using multimodal MRI, we also present another study for co-registration of

pathologies observed in-vivo with postmortem tissue. The in-vivo pathological changes can be validated using ground truth to understand the underlying lesions. We also present a automated registration approach to co-register in-vivo MRI and post-mortem tissue photographs. The novel approach is that we use an intermediate post-mortem MRI as an intermediate guide to register them.

TABLE OF CONTENTS

LIST OF TABLES

LIST OF FIGURES

PREFACE

I have been very fortunate to have great support throughout my journey as a student and a researcher. This journey as a doctoral student has been the best roller-costar ride I have ever taken. It might have to be a separate document if I have to thank everyone who has significantly contributed to my life journey so far, but I would like to keep this to those who have helped in my journey as a student.

This doctoral dissertation especially, I have had immense contribution from several people. I am very grateful to my advisor Dr. Howard Aizenstein, firstly for adopting me midway through my PhD and secondly for guiding me through the past few years to bring my dissertation to successful completion. I have also had the privilege to have wonderful and friendly committee members; Dr. Charles Laymon, Dr. George Stetten, and Dr. Kim Kang. I have had the opportunity to interact with them on a more personal level. Dr. Laymon has been very helpful in this work, sitting beside me for hours to help me get the data I needed and clarifying any questions I might have. He has always been very accommodative and friendly, as I would just drop by his office casually and ask for help and he would do it. I have always looked up to Dr. Stetten even while as a graduate student at Carnegie Mellon University. It has always been humbling to see him work hard in research still like an enthusiastic student. Dr. Kang has been very supportive since I took his class in my first semester at University of Pittsburgh. He has always been encouraging and enthusiastic to help me out. I would like to thank the members of Geriatric Psychiatry and Neuroimaging lab (GPN) for helping me either contributing to thesis which has stirred the work in the right direction or entertaining me so that my brain doesn't get fried too much working. I am thankful to Minjie Wu for brainstorming ideas, helping me analyze

play. I am/will be grateful for all the lovely things given to me and I am geared up for everything

I can give back going forward. Here's to many more.

1.0 INTRODUCTION

1.1   ALZHEIMER'S DISEASE

Alzheimer's disease (AD) is neurodegenerative disorder affecting more than 5 million people in the world and is the sixth leading cause of death (Alzheimer's, 2016). AD is the most common form of dementia affecting ages 65 years and older, characterized by memory loss, reduced cognitive and behavioral ability which affects the person's ability to perform everyday activities. It is a slow progressing disease and worsens with age (Alzheimer's, 2016).
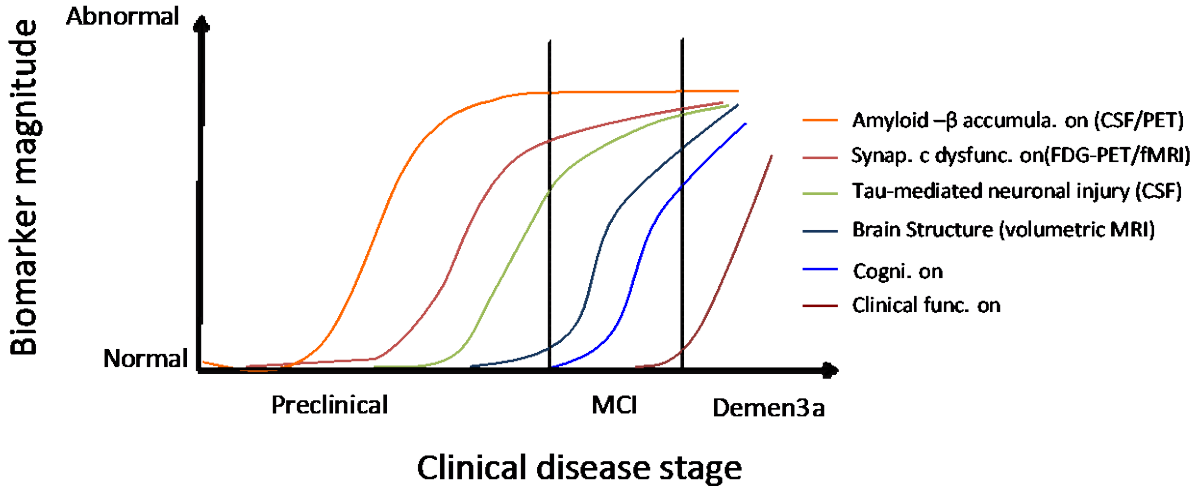
Figure 1 Hypothetical model for biomarkers of Alzheimer's disease

(Jack et al., 2010), figure adapted from (Sperling et al., 2011)

1

Early detection of Alzheimer's is important in developing effective prevention and treatment strategies. In the preclinical stage there are no cognitive or memory loss but as the disease progresses it leads to severe cognitive dysfunction. This is due to neuronal loss and damage to synapses. There are several hypotheses as to how the disease progresses. The most widely used model described by Jack et al (Jack et al., 2010) (shown in figure. 1) proposes that amyloid-β (Aβ) is the earliest detectable pathological change in Alzheimer's disease. Although the disease has no cure, novel prevention and treatment strategies are being developed and tested to delay the progression from Aβ accumulation to AD.

1.2 BIOMARKER'S OF ALZHEIMER'S DISEASE

Biomarkers are objective indications of medical signs measured in the body that help to predict the incidence of a disease. In AD, cerebrospinal fluid and neuroimaging biomarkers help in characterizing AD. The changes in these biomarkers however do not happen at the same time. The commonly studied biomarkers include amyloid-β 42 ($A\beta 42$) peptides and tau protein in CSF (Tapiola et al., 2009), and PET imaging markers amyloid-β plaques (example: Florbetapir (Carpenter, Pontecorvo, Hefti, & Skovronsky, 2009; Okamura & Yanai, 2010), Pittsburgh compound –B) (Klunk et al., 2004) (Klunk, 2011) and neurofibrillary tangles (NFT) (example: AV-1451)(Mishra et al., 2017). The biomarkers are believed to change in a specific pattern and these changes occur before clinical symptoms set in. The changes occur at three different stages, initial preclinical stage, mild cognitive impairment and finally diagnosis of severe Alzheimer's. Preclinical Alzheimer's occurs several years before clinical decline where gradual

pathophysiological changes begin to occur without any clinical symptoms of illness. Mild cognitive impairment is a syndrome defined as cognitive decline greater than expected due to normal aging. MCI patients are at a high risk of dementia with an annual conversion rate of 3–10% (Bruscoli & Lovestone, 2004; Farias, Mungas, Reed, Harvey, & DeCarli, 2009). The final stage, when all the biomarkers reach a ceiling, is associated with severe dementia.

The biomarker model in figure 1 shows the pattern of common biomarkers of AD where they follow a sigmoid shape. Amyloid-β protein accumulation in the brain is the earliest pathological change occurring in the brain before the clinical symptoms. The other biomarkers begin to occur with a lag from the onset of Aβ. The lag is dependent on the patient but in general the clinical symptoms may develop years or decades after the onset of Aβ. Amyloid biomarkers include reduction in CSF $A\beta 42$ and increased tracer retention in the brain when imaged in vivo using positron emission tomography(Klunk, 2011). Synaptic dysfunction is the second most noticeable biomarker change after amyloid. Synaptic activity can be detected using 2-[(18) F] fluoro-2-Deoxy-D-glucose-positron emission tomography (FDG-PET) as brain glucose metabolism is determined by synaptic activity. Functional magnetic resonance imaging (fMRI) is another functional neuroimaging technique which is sensitive to changes in synaptic function (Brickman, Small, & Fleisher, 2009). Synapses are the fundamental information processing units, comprises of a pre-and post-synaptic regions. It is believed that Aβ affects the synaptic transmission and plasticity. Structural MRI is thought to become abnormal subsequent to the synaptic changes. The structural MRI changes include gray matter atrophy (often measured as cortical thinning). Each of the biomarkers exhibits different rates of change and occurs over a span of several years. These imaging biomarkers provide information about the various stages of the disease.

1.2.1 Amyloid $-\beta$ protein plaques

AD is characterized by abnormal amyloid protein deposition in the brain. Amyloid-β is a smaller portion of amyloid precursor protein (APP). It is believed that abnormal processing or ineffective clearance leads to the accumulation of amyloid plaques in the brain. Beta-amyloid slowly starts to accumulate in the brain and is considered a neuropathological hallmark of AD. When they start to accumulate in the brain they form clusters called oligomers, which further forms chain-like structure called fibrils(Irvine, El-Agnaf, Shankar, & Walsh, 2008). The fibrillar structure form beta-sheets clumps together with other substances to form beta amyloid plaques. These plaques were initially discovered in autopsy of brain (Maurer, Volk, & Gerbaldo, 1997) but after the invention of amyloid imaging compounds amyloid can be visualized in vivo using PET (Sojkova & Resnick, 2011). The final stage is plaques, which contain clumps of beta-sheets and other substances. Cerebral beta-amyloid levels are in a dynamic equilibrium; levels of amyloid represent a balance between biosynthesis of APP and its degradation and clearance (Tapiola et al., 2009). In AD the amyloid depositions in the brain increases. The conventional view is that the soluble Aβ disrupts synaptic transmission and the plaques contribute to local inflammation and neurodegeneration (Mucke & Selkoe, 2012). These pathways disrupt the communication between neurons and ultimately activate immune cells. It is critical to study the role of Aβ in progression of AD and detecting increased amyloid deposition is crucial in preventing the disease(O'Brien & Wong, 2011).

1.2.2 Tau protein neurofibrillar tangles

Tau is the microtubule-associated protein (Chapman et al.) of a neuron (Dehmelt & Halpain, 2005). Tau protein plays a critical role in neurodegenerative disorders, especially AD(Iqbal, Liu, Gong, & Grundke-Iqbal, 2010). Along with Aβ plaques, abnormal tau protein is also present at

the synapses. In AD, tau protein is abnormally hyperphosphorylated and aggregated into bundles of filaments, which is seen as neurofibrillary tangles. Tau protein starts to accumulate in the neurons slowly disrupting the neuronal activity and release into extracellular spaces, which appear in CSF. Total tau (t-tau) and phospho-tau (p-tau) levels increase in CSF much before the clinical symptoms occur. Presence of increased levels of tau protein pathological changes is associated with neuronal injury (Gendron & Petrucelli, 2009). FDG-PET is used to measure brain metabolism, which, although including many neural and glial functions, largely indicates synaptic activity. Decreased FDG-PET uptake is an indicator of impaired synaptic function.

1.2.3 Structural changes in Alzheimer's disease

Structural changes are observed as cerebral atrophy, which is caused by neuronal cell death and loss of synapses and neurons(Gorelick et al., 2011; Hilbert et al., 2015; K. A. Johnson, Fox, Sperling, & Klunk, 2012; Meier et al., 2012). Volumetric measurements from MRI show significant decrease in brain atrophy (figure 2) and based on disease severity show severe cognitive decline. Studies have found significant decreases in the grey matter in medial temporal lobe, precuneus, tempo-parietal cortex, insular and cingulate cortex, and caudate nucleus (Frisoni, Fox, Jack, Scheltens, & Thompson, 2010; Frisoni et al., 2002; Guo et al., 2014). Both whole brain atrophy and hippocampal atrophy (Henneman et al., 2009) distinguish patients with AD from controls and correlate with cognitive decline (Nelson et al., 2012).
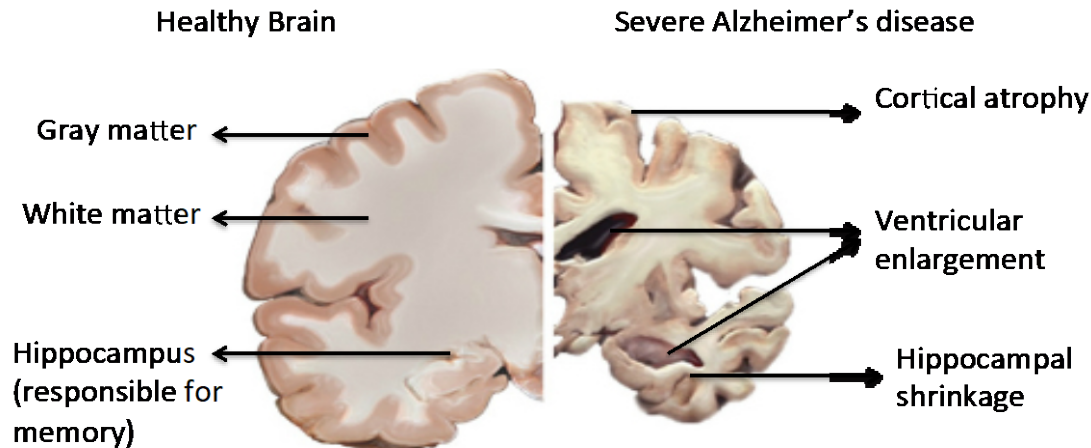
Figure 2 Brain changes in severe Alzheimer's disease compared to healthy brain

adopted from nia.nih.org

1.3 CHALLENGES IN EARLY DETECTION OF AD

Early detection of biomarkers changes in the preclinical stage of the disease is essential for developing preventive therapies for Alzheimer's disease (AD). PET imaging of amyloid and metabolism have proven to be a promising tool in the early diagnosis of AD. PET imaging biomarkers appear during the preclinical stages of AD and can predict decline years before the onset of symptoms (Cohen & Klunk, 2014; Jack et al., 2012; Marcus, Mena, & Subramaniam, 2014; Sperling et al., 2011). In vivo brain amyloid imaging using PET demonstrates accurate detection of amyloid deposition in the brain, which helps to identify AD with higher accuracy. Screening for amyloid is needed to improve the early detection of AD. But the radioactive exposure restricts the frequency of use of the imaging technique and is also very expensive. One possible alternative is structural MRI, which is advantageous, as it does not expose patients to radiation and is relatively inexpensive. Structural MRI can characterize brain changes that

6

related to AD but the MR signal can also carry information about amyloid. Due to this, it could be used in studies where frequent or repetitive imaging is necessary. With increased accumulation of amyloid plaque in the brain, the structural brain integrity is slowly affected throughout the pre-clinical AD period and thus may predict amyloid burden in the brain. Volumetric changes show significant changes towards the late stages of the disease but voxel level information can capture some information that may predict amyloid. Animal studies have shown that MR signal can carry information about amyloid (figure 3). This involves scanning the animal inside the scanner for long duration and dissecting them immediately after scanning. This study is not feasible in humans but it validates that MR signal can carry some information about amyloid. Although currently structural MRI cannot visualize amyloid in-vivo in humans combining the multiple MR modalities may help predict amyloid. Machine learning techniques can capture the subtle patterns in the MR modalities that may be helpful in amyloid prediction.
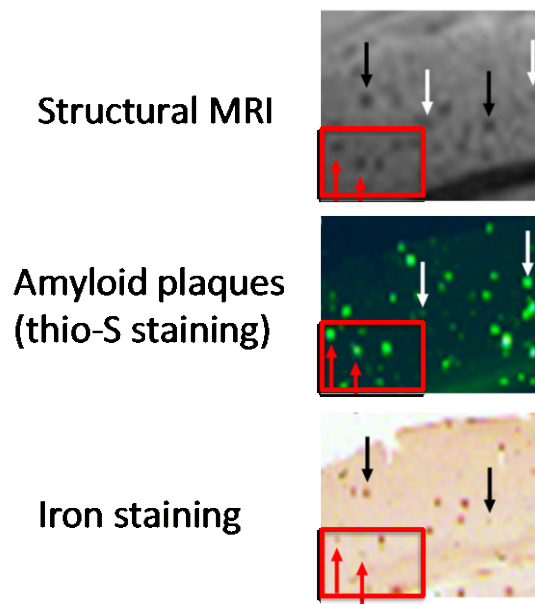
Figure 3 Amyloid deposition detected using MRI in mouse model

The red box shows amyloid plaques common between MRI, amyloid staining and iron staining (adapted from

(Chamberlain et al., 2009)

1.3.1 Specific Aims

The aim of this study is to use a pattern recognition baxsed approach to predict amyloid using multimodal magnetic resonance imaging (MRI). In addition to amyloid, in AD, there is an occurrence of brain atrophy (tissue loss) and loss of structural integrity in both white and gray matter, which can be, detected using MRI. Studies have shown that hippocampal atrophy, regional specific cortical thinning, vascular and microstructural changes in gray matter volume are associated with progression of AD. Different MR imaging sequences and contrasts exist, including magnetization prepared rapid gradient echo (MP-RAGE), a high resolution T1-weighted imaging; T2-weighted fluid attenuated inversion recovery (FLAIR), which enhances white matter lesions and suppresses signal from CSF; Susceptibility weighted imaging (Moller et al.) which highlights tissue magnetic susceptibility differences; and diffusion tensor imaging (DTI), which measures directional diffusion of water molecules. Each of these contrasts/sequences characterizes different aspects of brain structural integrity. Characterizing the structural imaging relation to amyloid deposition could increase the accessibility of amyloid imaging. These MR modalities can be used individually or combined with other modalities to estimate regional amyloid burden. To achieve this, we propose the following aims:

Aim 1: Explore the relationship between Aβ deposition and multimodal MRI within subject

<u>Hypothesis 1.1:</u> We hypothesize that regional amyloid burden will be associated with regional multi-modal MR features.

<u>Approach 1.1:</u> Features defining the multimodal MR structural changes like intensity gradient filters, Gabor filters, and local binary patters will be extracted from each modality.

Lasso regression will be used to predict voxel-level amyloid burden using the aligned voxels from multimodal MR and filtered images.

Hypothesis 1.2: Within an individual, progression of Aβ deposition will be associated with changes in multi-modal MR markers.

Approach 1.2: Imaging data across time-points, and the learned MR-Aβ relation from baseline cross-sectional data will be extended to the longitudinal time points to predict and measure the progression of amyloid burden for each subject.

Aim 2: Extrapolate the within subject MR- Aβ relationship to predict amyloid burden across subjects.

Hypothesis 2.1: MR- Aβ relationship across subjects can be optimized using subject specific information.

Approach 2.1: The MR- Aβ relationship (learned lasso parameters) is estimated using subject demographics and summary MR features (gender, race, age, weight, hippocampal volume, gray matter index etc.) from which the voxel and regional amyloid burden can be obtained.

Hypothesis 2.2: MR estimated amyloid burden is a better predictor of amyloid status (overall positive or negative) than using cognitive or MR global variables

Approach 2.2: Subject demographic and global MR summary features are used along with machine learning models to predict amyloid status. The predictions are compared to the performance of the classifier based on local MR estimated amyloid burden from approach 2.1.

In MR research it is rare to find post-mortem ground truth to validate the pathological changes that we observe in-vivo MRI and PET imaging. It is however feasible to perform these

correspondences between in-vivo and post-mortem tissue in the elderly subject population. The subjects are recruited late life and are scanned in-vivo. At post-mortem, their tissue is scanned using MRI and photographs of tissue slices are taken. We developed an automated non-linear registration method to co-register the in-vivo MRI and post-mortem tissue photographs.

1.3.2 Clinical Impact

1.3.2.1 Study 1: Amyloid Prediction

If successfully developed, the amyloid prediction algorithm will use only multimodal MRI and subject-level information to predict voxel level distribution of amyloid. The amyloid voxel level distribution during the preclinical stage can help screen the risk patients and also plan treatment strategies. It can serve as an alternative tool for screening patients that are showing increasing amyloid burden. Identifying the risk patients can then be further monitored using PET. This will reduce the exposure to radiation by injecting a radio-active tracer into the body.

1.3.2.2 Study 2: Co-registration of in-vivo MRI and post-mortem tissue photographs

The method involves using a whole hemisphere post-mortem MRI that can guide the registration process. Due to tissue deformation after death having an additional whole hemisphere MRI can act as an intermediate step in the co-registration process. Although there is gap between acquisition of in-vivo and post-mortem imaging this method has immense potential to reduce significant time for manual registration and can aid in the histology analysis. The information that can be gained from understanding the underlying pathology is very useful to understand the disease as well.

1.4 THESIS ORGANIZATION AND CONTRIBUTIONS

1.4.1 Thesis Organization

Thesis chapters are organized as follows

Chapter 2 overview of amyloid biomarker and the importance of in-vivo detection techniques, PET physics, PET scanner and amyloid imaging

Chapter 3 provides an overview of structural brain changes in AD, detection using MRI. It deals with MR physics, structural MR contrasts and image preprocessing.

Chapter 4 provides an introduction to pattern recognition techniques in neuroimaging specifically AD and amyloid positivity detection. It also gives a brief overview of the methods used in this work

Chapter 5 addresses the use of multimodal MRI and pattern recognition/ machine learning techniques for detecting voxel-level amyloid in the brain

Chapter 6 addresses non-linear registration method for co-registration of in-vivo MRI Post-mortem photographs

Chapter 7 provides an overall conclusion and possible future work

1.4.2 Thesis contribution

Our contributions include

1. Analysis to prove that the multimodal MRI can predict amyloid imaging voxel-level

2. Amyloid change detection within subject (using longitudinal data)

3. Amyloid prediction and status classification across subjects (using cross-sectional data)

4. A co-registration method to aid in the co-registration of in-vivo MRI and post-mortem photographs for correspondence studies.

2.0 AMYLOID: NEUROPATHOLOGICAL BIOMAKER

Amyloid plaques are a key neuropathological criterion for diagnosis of Alzheimer's dementia(Serrano-Pozo, Frosch, Masliah, & Hyman, 2011). It helps distinguish from other dementia types like frontal-temporal dementia, Lewy body dementia(Karantzoulis & Galvin, 2011). The diagnosis of Alzheimer's disease was mainly based on the clinical manifestation of symptoms and detection of amyloid plaques was needed at autopsy for definite diagnosis. After the development of amyloid binding compounds, the in-vivo detection became feasible using positron emission tomography. The in-vivo detection of amyloid can help in developing medical intervention for clearing amyloid. Amyloid clearance therapies have raised new avenues for improving cognitive function and potentially reversing the underlying disease. Immunotherapy includes intravenous immunoglobulins (IVIG) containing Aβ antibodies(Kile & Olichney, 2007)'(Loeffler, 2013; Relkin, 2014) and specifically developed monoclonal antibodies for Aβ(Panza et al., 2011; van Dyck, 2018). In this work amyloid imaging is obtained from positron emission tomography and these images are used as ground truth for the prediction analysis discussed in the chapters to follow. This chapter gives a brief overview of postmortem detection of amyloid, introduction to PET physics, process of PET image production and its utility in amyloid imaging. The focus of PET and its utility in neuroimaging is broad but for this work we will be focusing only on in-vivo amyloid imaging.

2.1 AMYLOID DEPOSITION IN ALZHEIMER'S DISEASE

2.1.1 Histological detection of brain protein deposition

Pathological changes like amyloid plaque deposition, associated with AD are confirmed using post-mortem studies (figure 4). The post-mortem studies are also helpful in understanding the involvement of amyloid deposition in cognitive impairment (Nelson et al., 2012; Nelson, Braak, & Markesbery, 2009). The neuropathological abnormalities of Alzheimer's disease can also be seen in brains of cognitively normal aging individuals. Studying the correlations between the extent and distribution of such changes in brain specimens in aged individuals who had intact cognitive performance have started gaining attention (Ikonomovic et al., 2008; Seo et al., 2017). The in-vivo accumulation of amyloid in the brain also needs to be confirmed using post-mortem studies(Perl, 2010). In order to correspond anatomical locations of the in-vitro tissue changes with in-vivo imaging, it is important to register them together. Registration of in-vivo MR imaging with tissue photographs has its own limitations. Since tissue deformation happens at post-mortem the registration process is more difficult to match MR in-vivo images with the post-mortem tissue photographs. To aid in the registration process ex-vivo MR imaging before histology can be used as an intermediate for better registration of ex-vivo photographs to the in-vivo MR imaging (described in chapter 4).
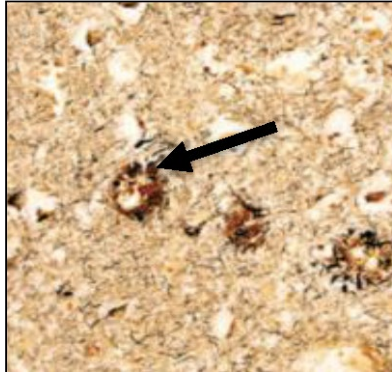
Figure 4 Amyloid plaques (black arrow) histology (figure adapted from (Perl, 2010))

2.1.2 Amyloid imaging using Positron emission tomography

PET allows the visualization of radioactivity distribution within a subject using the emitted radiation by linking the interior distribution with an exterior (and measurable) radiation pattern. When a biological target is tagged with a radioactive atom (called a tracer) then the biological process or condition can be visualized.

2.1.2.1 Tracers in PET

The tracer is a radioactive pharmaceutical, which is a positron emitting nuclide. The tracer molecule consists of positron emitting isotope that is bound to an organic ligand (targeting agent). In PET imaging, a small amount of tracer is injected into the patient, intravenously. The tracer is chosen based on the target region measured. The tracer binds to the subject target tissue and the radioactivity in the target region is measured and quantified. Essentially any biologic process, for which a suitable probe can be isolated/synthesized and labeled with a positron-emitting isotope, can be quantified using PET. There are many positron-emitting radioactive isotopes used in PET (e.g., ^{11}C, ^{13}N, ^{15}O, ^{18}F). For example, the commonly used PET radiotracer is fluorodeoxyglucose (FDG) is comprised of ^{18}F isotope that is bound to 2-deoxy-2-glucose which is a glucose analog molecule. Chemically FDG is involved in cellular metabolic activity.

15

In neuroimaging, FDG-PET is used to measure cerebral metabolic rates of glucose (CMRglc), which is an indirect measure of neuronal activity in AD(Mosconi et al., 2010).

For imaging amyloid a ^{11}C labeled ([N-methyl-^{11}C] 2-(4'-methylaminophenyl)-6-hydroxybenzothiazole also known as Pittsburgh compound – B (PiB); (Mathis et al., 2003)) was developed that binds to amyloid. But the half-life of PiB is 20 minutes. In contrast to PiB, ^{18}F labeled compound Fluorbetapir ($C_{20}H_{25}FN_2O_3$ also known as Amyvid) have half life of 110 minutes and bind to amyloid plaques(Klunk, 2011; Klunk et al., 2004).

2.1.2.2 Method of PET image acquisition

PET Physics

PET physics involves the interaction of subatomic particles positron and electron. An electron is negatively charged subatomic particle. While a positron particle has the same mass as an electron but is positively charged. When the electron and positron interact, they produce other particles and this process is termed as annihilation. Here an electron and a positron annihilate to produce two photons, each having an energy of 511 keV, that are emitted at 180° apart in the center-of-mass system. The energy of the photons is sufficient that a substantial fraction can escape from the head and can be detected. This allows for in-vivo scanning biological processes and tissues in neuroimaging.

The line that passes through the subject connecting the relevant detectors of these two photons is called the line-of-response. Knowledge of integrals of radioactivity concentration along a sufficient number of LORs allows reconstruction of the image of radioactivity concentration. The overview of the method of PET image acquisition is shown in figure 5.
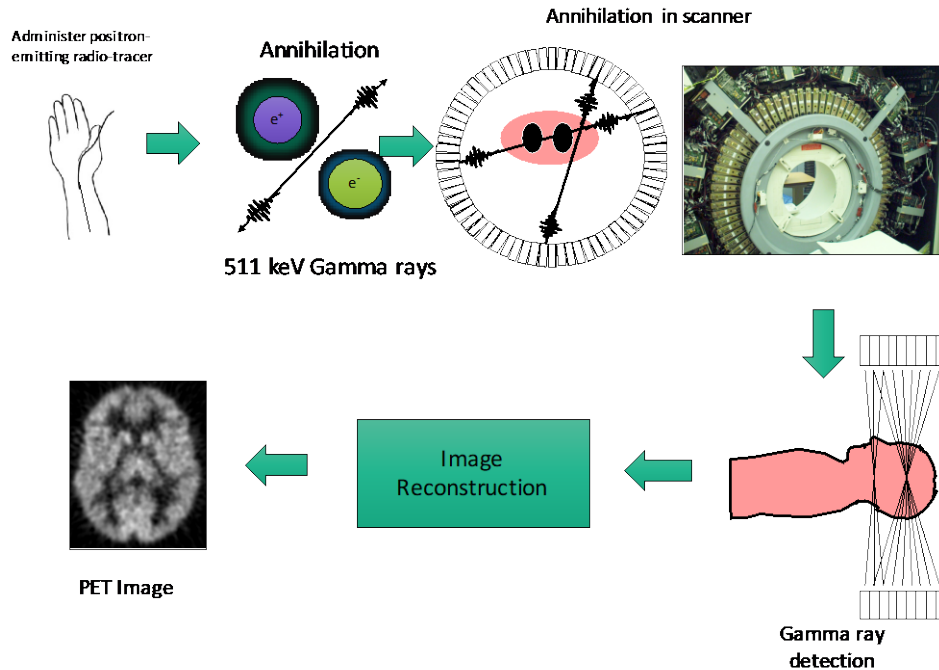
Figure 5 Schematic of PET Scanner

PET Scanner

PET scanner provides the capability to acquire the required image data. The annihilation process ends up with 2 back-to-back 511 keV photons, which provides the required LOR integrals to recreate the image. The detectors are placed in a circular manner around the subject PET scanner contains detectors optimized for detecting 511 keV photons. The coincidence photons count rates are measured (which are proportional to the required activity concentration integrals) along the various LORs.

The PET scanner contains detectors optimized for detecting 511 keV photons. The PET scanner used to obtain the amyloid imaging in this study is a PET system ECAT EXACT HR +, manufactured by Siemens/CTI (Knoxville, TN) (Brix et al., 1997). The scanner has a patient port of 56.2 cm consists of four rings of bismuth germinate (BGO) crystal blocks with an inner diameter of 82.7 cm(Brix et al., 1997). Each of the 72 blocks per ring is cut into an 8 X 8 array of

17

detector elements with dimensions of 4.39 mm X 4.05 mm X 30 mm (axial X transaxial X depth) separated by small slits of 0.46 mm(Brix et al., 1997). The whole system thus consists of 32 detector rings with 576 distinct crystal elements per ring, allowing it to image 63 trans axial slices simultaneously(Brix et al., 1997). The maximum field of view (FOV) is 15.5 cm in the axial direction. (Brix et al., 1997)
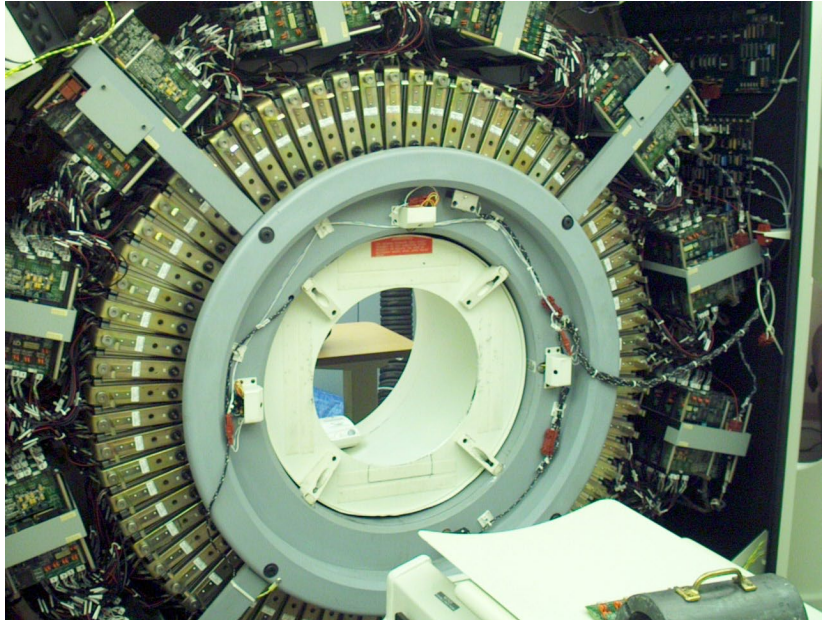
Figure 6 An open PET scanner showing the detector housing and electronics (Photo Courtesy: UPMC PET Center, C. Laymon)

These detectors are arranged in a cylindrical manner (shown in figure 6) and allow for the detection of both emitted photons in coincidence in separate detectors opposite to each other. The distribution of radioactivity is measured by the counting of all the annihilation count rates that are detected along the various LORs. This produces sufficient information for image reconstruction. The gamma rays interact with the detectors to produce scintillation light. Scintillation light is detected by photomultiplier tubes (PMTs) and once struck the respective crystal is identified by the light distribution within the PMTs. by using coincidence detection of

annihilation events within a short time window of 12ns for the HR+ (Saaidi, Toufique, Merouani, Elbouhali, & El Moursli, 2016) .

Coincidences of photons

When both photons are from an annihilation event without any scattering prior to detection it is termed as a **true coincidence**. In **scattered coincidence**, at least one of the photons undergoes a Compton scattering event prior to detection. The resulting coincidence event will be assigned to the wrong LOR. Random coincidences occur when two photons are detected within the coincidence time window but are from different annihilation event. When **multiple coincidences** occur more than two photons are detected in different detectors within the coincidence time window. In multiple coincidences, it is not possible to determine the LOR of the event hence such events have to be ignored. PET data is processed using back projection and iterative reconstruction algorithms to form an image. Typically, in a clinical setting a combination of PET/CT scanner is used which helps in automatic correlation of the functional image (PET) with the anatomy (Meier et al.). The setup includes PET and CT scanner components as separate units within a single gantry and the scans are acquired sequentially. Note that PET scans are generally of much longer duration than CT scans.

Image reconstruction

After the detection of incidence of the two photons by opposite detectors the coincidence event is assigned to line of response joining the two detectors. With complete set of LORs lines in all directions intersect every point in the tissue in the patient's body. From the line integrals of radioactivity concentration the map of quantity for entire region being image can be reconstructed. The PET image reconstruction is formulated as a linear inverse problem. There were several reconstruction algorithms used in PET. Filtered back projection is an analytical reconstruction method which is fast and direct but cannot model the physical effects of PET scanners or variability in the photon detection(Tong, Alessio, & Kinahan, 2010). Iterative reconstruction algorithms like maximum likelihood estimate and ordered subsets method estimation-maximization (OSEM) can model the statistical noise of the PET scanner and produce more accurate image reconstruction results(Tong et al., 2010). Nowadays, OSEM are the most commonly used methods and some modern scanners (GE and Philips) the FBP reconstruction technique is not available. The PET images used in this study for amyloid imaging are quantified using standardized uptake value ratio (SUVR).

Standard uptake value (SUV) is a relative measure of the tracer uptake and is given by the expression (Kinahan & Fletcher, 2010)

$$SUV = \frac{r}{(a'/w)}$$

where r is the radioactivity activity concentration [kBq/ml] measured by the PET scanner within a region of interest, a' is the decay-corrected amount of injected radiolabeled tracer [kBq], and w is the weight of the patient [g].

Decay correction is needed to account for radioactive decay at a particular time. It mainly involves calculating weighting factors that transform the measured activity values for every time frame to values that would be measured if the activity had remained constant in time(Dawood, Jiang, & Schäfers, 2012). Here r and a' have to be decay-corrected to the same time. Standard uptake value ratio (SUVR) for PiB imaging is calculated as ratio of SUV of cortical tissue to the SUV of reference region (cerebellum). The reference region is chosen such that it has very low specific binding. For amyloid imaging we use the cerebellum because it is known to not accumulate amyloid (to a good approximation). The PiB uptake that we see in the cerebellum gray matter is believed to be nonspecific binding (i.e. to things other than amyloid) and also has similar tracer kinetics to the region of interest.

2.2 IMAGING WITH PITTSBURGH COMPOUND-B

The tracer (PiB) is intravenously injected to the patient. After 25 minutes the patient is placed in the scanner. The image acquired in the first few minutes is neglected as noise. Then the images are acquired continuous over time until about 70 minutes. The final amyloid image is averaged from 50-70 minutes, which is registered with the MR image for anatomical correspondence. The regions of interest are drawn using the registered MRI for the subject and these regions of interest are used to quantify the amyloid burden. The ROI sampling is performed using ROITOOL for the regions shown in figure 7 (Interactive Data Language, Boulder,CO program, ROITOOL)

Pattern of PiB retention is different in AD patients compared to cognitively normal(Cohen & Klunk, 2014) (figure 8). PiB retention in AD patients was more prominent in cortical areas than in white matter. PiB images from CN subjects showed little or no PiB retention in cortical areas. PiB retention is more specific to gray matter and its accumulation is prominent in specific regions in AD patients than CN subjects. PiB retention was broadly observed in frontal cortex, precuneus/posterior cingulate, temporal, and parietal cortices(Cohen & Klunk, 2014). The occipital cortex and lateral temporal cortex were also significantly affected with a relative sparing of the mesial temporal areas(Cohen & Klunk, 2014).

Frontal cortex (FRC)
Anterior cingulate gyrus(ACG)
Precuneus (PRC)
Parietal (PAR)
Anterior ventral striatum (AVS)
Lateral Temporal Cortex (LTC)
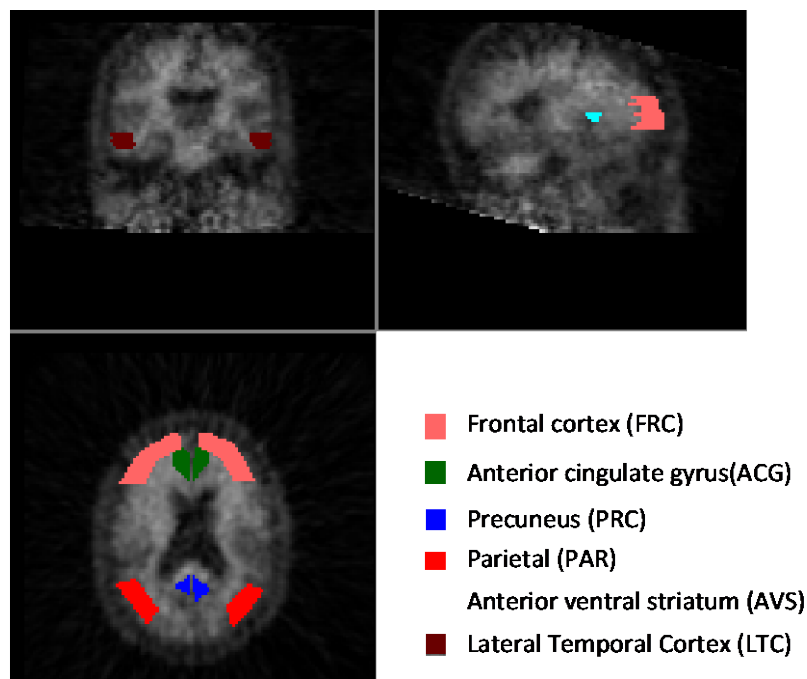
Figure 7 Regions of interest for amyloid imging (PiB)

The region of prominent distribution is found to be consistent with histopathological studies of Aβ plaques in the AD brain (Cohen & Klunk, 2014). With the use of PET (PiB), amyloid PET tracers may be useful in the early detection of AD when clinical symptoms are not fully expressed (Cohen & Klunk, 2014). Amyloid imaging is essential in the diagnosis of AD. A

demented patient without amyloid plaques cannot have AD-dementia by definition. Amyloid-PET is thus helpful to distinguish AD from non-amyloid dementias, such as FTD (Cohen & Klunk, 2014).

Pittsburgh Compound B (PiB)
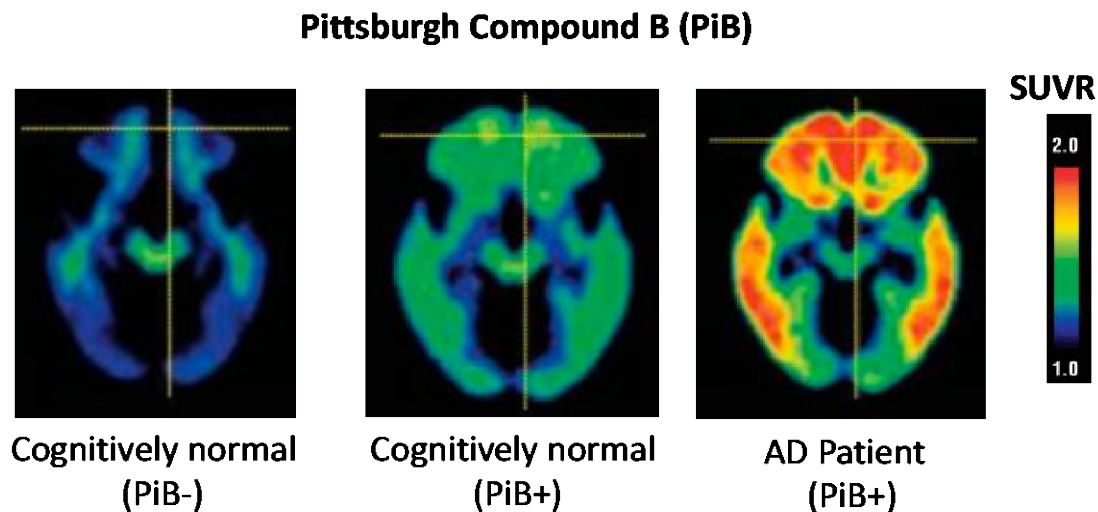
Figure 8 Distribution of brain amyloid deposition visualized using PiB (adapted from (Aizenstein et al., 2008)

2.2.1 Limitations of PET

PET procedures are expensive, time consuming (for PiB acquisition time is 50-70 minutes after injection of tracer). The technique is invasive and PET tracer due to their ionizing radiations pose issues with regard to production and distribution. The PET tracers have short half-life and they must be administered to patients within minutes or hours of being produced. Although the molecular/functional information from PET has helped in understanding several physiological dysfunctions or conditions, the resolution of PET imaging may not be as high as with other imaging techniques, such as MRI. Individuals are at risk due to exposure to ionizing

radiations. Structural MRI on the other hand has no harmful radiations and provide different contrast or modalities that may predict amyloid. It is used to quantify changes that are related to AD. The next chapter we discuss structural neuroimaging using MRI and MRI preprocessing methods that will be used in this thesis work.

3.0 STRUCTURAL NEUROIMAGING: MAGNETIC RESONANCE IMAGING

MRI is a commonly used non-invasive imaging technique, which provides detailed visualization of anatomical structure. They are not associated with any harmful or ionizing radiation and can be frequently utilized to study the structure and function of the human brain with low risk. The technique uses sophisticated technology to generate signal from the tissue based on magnetic properties of protons in the body and different modalities that can be generated for visualizing structure based on different magnetic properties of tissue. In neuroimaging structural MRI has been used for detection and diagnosis of neurological diseases (Frisoni et al., 2010; Wattjes, 2011).

3.1 NUCLEAR MAGNETIC RESONANCE

MRI utilizes free protons in the body which have a characteristic spin called precession. The precessing protons in the absence of a strong magnetic field are randomly aligned and net magnetic moment cancels out. A strong magnetic field forces protons in the body to align in the direction of the field creating a net magnetic moment.

When a radiofrequency pulse is given the aligned protons that are in a low-energy state are then energized into a high-energy state. The amount of rotation of the net magnetization when the RF pulse is applied is called flip angle (FA). The protons spin out of equilibrium, and when the RF pulse is turned off, the protons realign with the magnetic field. There are two types of relaxation: T1 or spin-lattice relaxation, and T2 or spin-spin relaxation. T1 (spin-lattice)

relaxation is the recovery of the net magnetization in the direction of the net magnetic field. T2 (spin-spin) relaxation is due to the de-phasing of the protons as they precess out of phase. Different tissues have differences in the T1 and T2 relaxation time, which can be utilized to produce the contrast between different tissue types. In addition to the two relaxation times there is additional exponential decay that occurs soon after the excitation pulse is stopped. This is called T2* relaxation or T2* decay which is due to non-uniformity in the magnetic field or magnetic susceptibility differences between tissues.

The protons realign with the magnetic field through relaxation process by releasing energy. This relaxation is the basis of the MR signal as an RF receiver coil measures the released RF energy. The repetition time (TR) is the time duration between the applications of one excitation pulse to the next. The frequency information of the signal from each location being imaged is converted to corresponding gray level intensities using Fourier transform. RF pulse generates sinusoidal signal decay called free induction decay to reach equilibrium. Two successive RF pulses produce a spin echo (SE), and the time between the middle of the first RF pulse and the peak of SE is called echo time (TE).

3.2 MR SCANNER COMPONENTS

3.2.1 Magnet

The superconducting magnets are the most important part of the scanner. The field strength is measured in tesla units, and typical clinical MR scanners for scanning humans range from 0.5 to 3T and for research studies from 1.5T to 7T.

3.2.2 Gradient coils

There are three gradient coils located in the MR scanner. Each of these produces three main magnetic fields in three directions (Gx, Gy, Gz), which can be operated to scan different parts of the body.

In the absence of imaging gradient all protons in an imaging plane resonate at near identical frequencies. If an excitation pulse is transmitted into a tissue during the application of magnetic field the tissue that resonates at a particular frequency corresponding to a particular position along the axis of imaging gradient is excited. After application of imaging gradient along one axis of the image plane the variation in resonant frequency occurs. The variation in frequency due to application of the gradient localizes the MR signals in one dimension within selected section. The process of encoding the spatial location of protons based on their positions relative to the gradient applied during this measurement is referred to as frequency encoding, and the gradient itself is referred to as the frequency encoding gradient (Gf). The selective excitation to choose an image section and frequency encoding gradients are used for spatial localization using frequency differences along axis of the magnetic field. The other in-plane axis of the image is localized by a different technique called the phase-encoding gradient.

Phase encoding involves mapping the location of the sources of MR signals based on their phase. The phase-encoding gradient (Gp) is produced by applying a magnetic field pulse perpendicular to the axes of section-selection and frequency encoding. The gradient pulse causes resonant frequencies that vary momentarily on the axis. After the phase encoding gradient has been removed the signal received shows phase differences. The phase-encoding gradient needs to be applied at different strengths to localize different MR signals. Strong phase-encoding gradients are useful for finer resolution but produce lower amplitudes than weak phase-encoding

27

gradients. The number of phase-encoding gradient strengths is proportional to the number of locations mapped along the phase-encoding axis.

3.2.3 Radiofrequency coil

A radio frequency coil is used to transmit and receive RF pulse. The RF transmitter generates the RF energy, which is applied to the coils and then transmitted to the patient's body. After transmission of RF pulses the tissue will respond by returning an RF signal. These signals are picked up by the receiver coils and converted into digital form and transferred to the computer where they are temporarily stored.

3.2.4 Shielding Coil

Shielding coil is used to restrain the region of strong magnetic field surrounding the magnet. There are two types of shielding: passive and active shielding. For passive shielding, iron beams or steel plates that have high permeability are incorporated into the walls, ceiling, and/or floor of the magnet room Active shielding is done by using secondary counteracting coils outside of the primary coils.

3.2.5 Computer System

The computer system performs several operations including acquisition control, image reconstruction, image storage and retrieval, and viewing control. The first step is acquisition of the RF signals from the patient's body. The process of image acquisition consists of repeated cycles of RF pulse that are transmitted and signals received. Images are acquired as K-space,

which is frequency and phase representation of the image from which Fourier transform is applied. Reconstructed images are stored in the computer for additional processing and viewing.

3.3 MRI SEQUENCES

Different types of MRI provide varied image contrasts and highlight specific characteristics of the brain. The most common sequences are T1-weighted and T2-weighted imaging. MR imaging sequences include magnetization prepared rapid gradient echo (MP-RAGE) (Mugler and Brookeman, 1990), a high resolution T1-weighted imaging; T2-weighted fluid attenuated inversion recovery (FLAIR), which enhances white matter lesions (Yoshita et al., 2006) and suppresses signal from CSF; proton density (PD), which measures the density of protons in brain tissue; susceptibility weighted imaging (Breteler et al.), which highlights tissues magnetic susceptibility differences; and diffusion tensor imaging (DTI), which measures directional diffusion of water molecules. In this work, we focus on T1-weighted imaging (3.3.2.1), T2-weighted imaging (3.3.2.2), T2-weighted (FLAIR) imaging (3.3.2.3) and Susceptibility Weighted imaging (3.3.2.4) (figure. 9).

3.3.1 Pulse sequences

By varying TR, TE and FA image contrasts (T1, T2 and T2*) can be altered on gradient echo and spin echo images. The simple spin echo (SE) sequence consists of 90° RF pulse, 180° pulse and an echo, while fast spin echo sequence consists of multiple 180° pulses and echoes following each 90° pulse. The gradient echo (GRE) sequence is produced by applying a single

RF pulse in conjunction with gradient reversal. GREs are used with short TR, TE and low FA. A fast 3D gradient echo pulse sequence designed for rapid acquisition with T1-weighted dominance is a magnetization prepared rapid gradient echo (MPRAGE) sequence. Susceptibility weighted imaging also uses GRE sequences. An inversion recovery (IR) sequence is a conventional spin echo sequence, which is preceded by a 180° inverting pulse. The time between 180° inverting pulse and 90° pulse is called inversion time (TI). The acquisition of T2-weighted imaging used in this work uses a spin echo sequence. A fluid attenuation inversion recovery (FLAIR) is a special inversion recovery sequence, which nulls the signal from cerebrospinal fluid from the resulting images with contrast similar to T2-weighted images.

3.3.2 MR Modalities

3.3.2.1 T1-weighted imaging

T1-weighted images are produced using short TE and TR times and T1 properties of tissue. The images have great contrast between gray and white matter. These images are typically used to segment the gray matter, white matter, and cerebrospinal fluid (CSF) and also quantify volumetric of cortical and subcortical regions in the brain (Chandra, Dervenoulas, Politis, & Alzheimer's Disease Neuroimaging, 2018) (Bozzali, Serra, & Cercignani, 2016). The difference in T1 relaxation between tissues produces different tissue contrasts. In the brain, CSF has longer T1 relaxation times, followed by gray matter, which has a medium T1 relaxation time. White matter, which is the most fibrous part of the brain, has short T1 relaxation time. Short T1 relaxation times correspond to higher intensity in MR image and long T1 relaxation times appear darker. CSF appears dark on T1-weighted images; gray matter intermediate intensity and white

matter has higher intensity values compared to CSF and gray matter. The T1-weighted imaging sequence uses short TR hence there is only short period of time for T1-relaxation, otherwise the protons will reach full-relaxation. T1-weighted imaging is most commonly used for characterizing structural changes, quantifying volumetric changes in the brain related to disease conditions like in AD.

3.3.2.2 T2-weighted imaging

T2-weighted images have long TR and TE and the contrast is opposite to that of T1-weighted imaging. Short T1-relaxation times have brighter intensity. CSF has longest T2-relaxation time, gray matter medium T2-relaxation time and shortest being that of white matter. The corresponding intensities on the MR image CSF hyperintensities and white matter hypointensities, with gray matter showing intermediate intensities. T2-weighted imaging can be used to visualize fluid in the brain.

3.3.2.3 T2-weighted fluid attenuated inversion recovery (FLAIR)

Attenuation of high signal intensity from CSF could help in the visualization of certain tissue abnormalities. Longer T2-relaxation times have brighter intensity. In FLAIR images the brain tissue appear similar to T2 weighted images with grey matter brighter than white matter but CSF is dark instead of bright. T2-weighted FLAIR imaging improves the visualization of age-related tissue lesions, specifically white matter hyperintensities (WMH) (Hajnal *et al*, 1992). WMH appear white (hyperintense) and can be used to segment these lesions more accurately (see section 3.5). This can be used to measure global WMH burden.

3.3.2.4 Susceptibility weighted imaging

SWI is a 3D high-spatial resolution, which are generated from GRE pulse sequences. Susceptibility-weighted imaging (Breteler et al.) uses tissue magnetic susceptibility differences to generate a unique contrast. Different tissue magnetic properties, like paramagnetic, diamagnetic, and ferromagnetic properties interact with the magnetic field distorting it and thus altering the phase of local tissue, which results in loss of signal. SWI helps to visualize and potentially quantify iron in the brain having ferromagnetic properties. Specifically SWI have been useful in studying micro-bleeds in aging brain (Haacke, Mittal, Wu, Neelavalli, & Cheng, 2009). SWI differs from conventional T2* weighted GRE sequences which are also used to detect the blood vessels. Flow compensation in all three directions is used to reduce artifacts due to blood flow. The magnitude and phase information are reconstructed separately and later combined for diagnostic purposes. The raw phase image undergoes further processing when compared to magnitude information. The raw phase information contains low frequency noise due to generalized field inhomogeneities and distortions due to air and bone tissue. Hence these phase images are first filtered using high pass filter and then combined with the magnitude image to produce SW images.
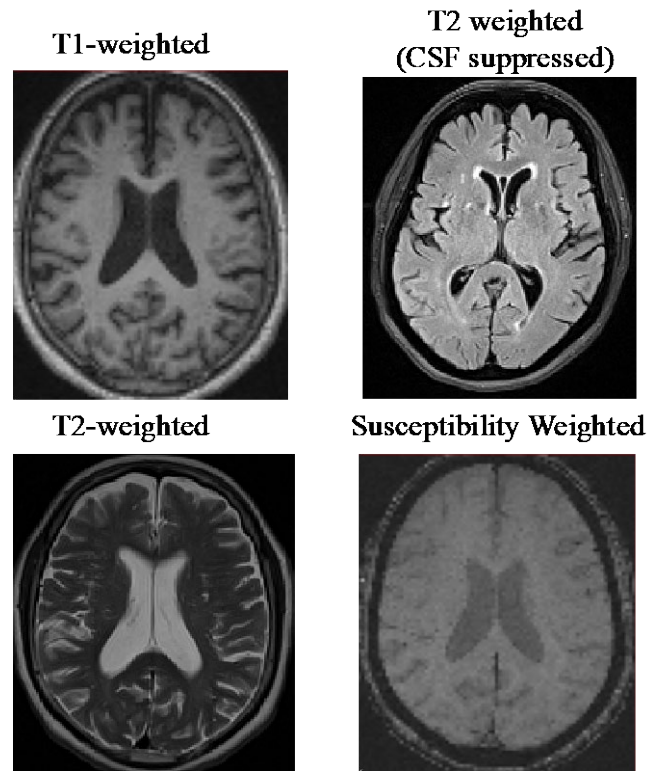
Figure 9 MR image showing a single axial section for T1-weighted, T2-weighted, T2-weighted (CSF suppressed) and Susceptibility weighted imaging

3.4 PRE-PROCESSING NEUROIMAGING DATA

There are several key pre-processing methods that are essential for processing neuroimaging data. Image registration is the process of aligning two images together, image normalization involves non-linear registration to a standard template, and image segmentation classifies voxels into regions of interest.

3.4.1 Image Registration

Registration is a process to obtain a transformation between two images in order to align them spatially. Image registration can be achieved using several different ways. There are four different types of geometric transformation: translation, rotation, scaling and shear that are performed obtain the registration two images. Translation involves movements along the coordinate space. Rotation is movement at an angle to the coordinate space. Scaling is deformation caused by enlarging or shrinking the image, which can be uniform or non-uniform along the coordinate axis. Shear is change in volume by deformation along parallel axes. Typically transformation models are a combination of these four geometric transformations. The two types of linear registration methods are intensity-based and feature-based registration methods.

3.4.1.1 Intensity-based registration

Intensity-based image registration uses a fixed image (reference image) and moving image (source image) where the moving image is transformed to align with the fixed image. The method optimizes the alignment between the two images by minimization (example, sum of squared differences (Myronenko & Song, 2010)) or maximization of cost function (example, normalized correlation (Jeongtae Kim & Fessler, 2004), normalized mutual information (Pluim, Maintz, & Viergever, 2003)) using image intensities. In this study we need to register different types of images (like registration between PET and MRI) and in such cases the maximization of normalized mutual information is a preferred metric.

Mutual information measures the amount of shared-information between the two images that reduces the uncertainty in them. Consider two images M and N where n, m are the voxel intensities; $n \epsilon N$ and $m \epsilon M$. When registered together the joint probability distribution p{m, n}, tells how frequently intensity value pairs occur together from which joint entropy can be calculated,

$$Joint\ entropy\ H(M, N) = -\sum_{n \epsilon N} \sum_{m \epsilon M} p\{m, n\} \log(p\{m, n\})$$

$$Marginal\ entropy\ H(M) = -\sum_{m \epsilon M} p\{m\} \log p\{m\}, \ H(N) = -\sum_{n \epsilon N} p\{n\} \log p\{n\}$$

Mutual information can be obtained as difference between joint entropy and sum of the marginal entropy of two images (M, N)

$$Mutual\ information\ I(M; N) = H(M) + H(N) - H(M, N)$$

$$Normalized\ mutual\ information\ \ Y(M; N) = \frac{H(M) + H(N)}{H(M,N)}$$

There are two types of transformation models: rigid transformation and non-rigid transformation. Rigid transformation allows changes in rotation and translation only and preserves shape and size of the image.

Three dimensional rigid body transformation matrix is defined as:

$$T_{rigid}(x, y, z) = \begin{bmatrix} x' \\ y' \\ z' \\ 1 \end{bmatrix} = \begin{bmatrix} r_{xx} & r_{xy} & r_{xz} & tr_x \\ r_{yx} & r_{yy} & r_{yz} & tr_y \\ r_{zx} & r_{zy} & r_{zz} & tr_z \\ 0 & 0 & 0 & 1 \end{bmatrix} \cdot \begin{bmatrix} x \\ y \\ z \\ 1 \end{bmatrix}$$

where r_{**} are rotation terms and tr_x, tr_y, tr_z are translation terms

Non-rigid or affine transformation matrix uses rotation, translation, scaling and additionally shear with three parameters for each direction in a 3D image (12 parameter affine transformation).

$$T_{affine}(x, y, z) = \begin{bmatrix} x' \\ y' \\ z' \\ 1 \end{bmatrix} = T_{shear}.\, T_{scale}.\, T_{rigid} = \begin{bmatrix} a_{11} & a_{12} & a_{13} & tr_x \\ a_{21} & a_{22} & a_{23} & tr_y \\ a_{31} & a_{32} & a_{33} & tr_z \\ 0 & 0 & 0 & 1 \end{bmatrix} . \begin{bmatrix} x \\ y \\ z \\ 1 \end{bmatrix}$$

where $a_{11} \dots a_{33}\ are\ affine\ parameters$

3.4.1.2 Feature-based registration

Feature based methods use boundary regions, edges, contours, and/or useful landmarks which can be manually (control points) or automatically (example scale invariant features) generated. Landmark-based or control point registration (W.-H. Wang & Chen, 1997) establishes a correspondence between images using distinct matching points between the two images. These pairs of corresponding points (control points or landmarks) are chosen manually or using automated methods. From these points the transformation matrix is calculated. The control point registration performed in this work for co-registration of in-vivo MRI to post-mortem photographs involves use of piecewise linear mapping functions for image registration method (Goshtasby, 1986). Using the corresponding control points in two images a linear mapping or transform is obtained. The piece-wise linear mapping first divides the images into triangular regions by triangulating the control points (Goshtasby, 1986). Then a linear mapping function is obtained by registering each pair of corresponding triangular regions in the images (Goshtasby, 1986). The overall mapping function is then obtained by piecing together the linear mapping functions (Goshtasby, 1986).

3.4.2 Image Segmentation and normalization

Image segmentation involves segregating group of voxels into regions or segments. There are several automated techniques for image segmentation like thresholding method (Mardia & Hainsworth, 1988), region-based segmentation (Adams & Bischof, 1994), watershed-based segmentation (Shafarenko, Petrou, & Kittler, 1997), graph-cut segmentation (Felzenszwalb & Huttenlocher, 2004). Image spatial normalization is used to align images to a standard template so that they can use for comparison across data. For example, in neuroimaging spatial normalization is used for comparison of volumes across subjects. In this work we performed segmentation using SPM12 software, which uses a unified segmentation and normalization method (John Ashburner & Friston, 2005).

3.4.2.1 Unified segmentation and normalization

Tissue segmentation can be done two approaches. The first one involves tissue classification approach where the voxels are assigned to a tissue class (WM, GM, or CSF) by characterizing the distribution of each tissue class. Tissue classification in SPM requires images to be registered with tissue probability maps. These maps represent prior probability of different tissue classes and Bayes rule can be used for classification into probability maps. The voxel based morphometry (VBM) (John Ashburner) in SPM requires images to be spatially normalized, segmented into tissue classes before performing statistical tests on grey matter. This procedure is circular because the registration requires tissue classification and tissue classification needs initial registration step to template. The unified segmentation and normalization aims to combine these two approaches into a single framework. This includes

optimizing for parameters that account for intensity non-uniformity. Estimating these model parameters (maximum posteriori estimate) involves alternating between classification, bias correction, and registration steps combined within same generative model instead of serial application of each of these steps.

The tissue distribution can be modeled by objective function mixture of Gaussians. The standard technique using in Bishop 1995, for tissue classification uses fitting a mixture of Gaussians to the tissue distributions. The mixture of Gaussian is modeled using parameters mean (μ_k), variance (σ_k^2), and mixing proportion of gaussians (γ_k). Tissue priors are used to assist in classification, which is estimated by registering a large number of subjects together, assigning voxels to different tissue types and averaging tissue classes over subjects. These tissue probability maps act as priors of any given voxel into each of the tissue categories (GM, WM or CSF). The number of Gaussians used to represent the distribution for each tissue class can be more than one since the voxel might fall in between intensity of different tissue types. The tissue probability maps are deformed as linear combination of about thousand cosine transform bases functions. The mixture parameters($\mu_k, \sigma_k^2, \gamma_k$) are updated using expectation-maximization approach while keeping bias (β) and deformation fixed (α). The bias is estimated by keeping the mixture parameters and deformation constant using Levenberg-Marquadt (LM) optimization scheme. Similarly, the deformation of tissue probability maps is re-estimated keeping bias and mixture of parameters constant. The optimization of terms for re-estimating the deformation of tissue probability maps involves use of the same LM scheme.

3.4.2.2 WMH Segmentation

White matter segmentation includes a fuzzy seed based segmentation (M. Wu et al., 2006) that identifies hyper intensities in the FLAIR that corresponds to the white matter lesions (Debette & Markus, 2010(Gorelick, 2011 #1813). The major steps of the method include image preprocessing, WMH segmentation and WMH localization. Image pre-processing includes removal of skull from T1-weighted and T2-weighted FLAIR images. For WMH segmentation, the WMH seeds are identified based on the intensity histogram of the FLAIR image. The threshold is selected from the histogram which corresponds to value that is mean + 3 ×standard deviation. The voxels above the threshold are used as seeds in the fuzzy connected algorithm to segment surrounding WMH voxels. The segmentation method is an iterative algorithm, which clusters voxels based on their adjacency and affinity to the seeds. After each iteration, the seeds are updated until the number of seeds becomes zero. The WMH burden is quantified by voxel counts or volume and used as a neuroimaging biomarker. The fully automated WMH segmentation system was implemented in C++ and ITK.

Although currently structural MRI cannot help visualize amyloid deposition in the human brain. The subtle changes or patterns in the different contrasts or modalities can be detected by the machine learning algorithm to predict amyloid. The next chapter deals with use of machine learning and pattern recognition in neuroimaging.

4.0 PATTERN RECOGNITION IN NEUROIMAGING

4.1 INTRODUCTION

Pattern recognition is process of automated recognition and detection of patterns and regularities present in the data. Pattern recognition algorithms are also sometimes referred to as machine learning algorithms because the function of the algorithm is to learn a pattern (Bishop, 2006). Mostly the terms pattern recognition and machine learning are inter-related. The pattern recognition techniques have shown promise for biomarker detection from neuroimaging data (Kambeitz et al., 2015). Pattern recognition/machine learning analysis has been successful in identifying MR imaging biomarkers for schizophrenia(Kambeitz et al., 2015), depression(Kambeitz et al., 2017), multiple sclerosis(Weygandt et al., 2011), dementia(Fan, Resnick, Wu, & Davatzikos, 2008). In these techniques, the data is first transformed into a form that is usable, termed as features, for machine learning algorithms. The algorithm will learn to recognize patterns in the features. For instance, in the amyloid prediction problem, the algorithm will learn the regional amyloid intensity associated with a pattern of MRI features. With advancements in medical image analysis valuable features can be extracted from neuroimaging data. PR and ML methods when applied to neuroimaging data learn the underlying patterns and can applied for prediction of future data. Specifically, in AD determination and amyloid detection machine learning methods have been extensively used which will be discussed in the following sections.

4.2 LEARNING THE ML ALGORITHM

The algorithms learn during a training phase, and the performance is evaluated during a test phase. Learning can be classified as supervised(Kotsiantis, Zaharakis, & Pintelas, 2007), unsupervised(Kotsiantis et al., 2007), semi-supervised(Chapelle, Scholkopf, & Zien, 2009) and reinforcement learning(Sutton & Barto, 1998).

4.2.1 Supervised learning

When the machine-learning algorithm learns from labeled (desired outcome variable) train data, in order to predict the correct response when posed with new examples comes. Each instance of data used for training consists of input-output pair. The learning mechanism is analogous to human learning with examples under the supervision of a teacher. Using each example, the student generates rules, which can be applied on future data for specific application being trained for. Some examples of supervised learning include, support vector machines(Scholkopf & Smola, 2001), neural networks(Hush & Horne, 1993), k-Nearest neighbor(Mucherino, Papajorgji, & Pardalos, 2009), decision trees (described in section 5.3.1.1.) (J. Ross Quinlan, 1986).

4.2.2 Unsupervised learning

In contrast to supervised learning, unsupervised learning algorithm learns from examples without any associated labels. The algorithm determines the patterns in the data and learns from the examples by representing them as new series of variables. They are helpful in understanding the data and can provide additional information related to the application. It resembles the way human brain finds association and connection objects or events by observing the degree of

similarity between objects. The search engines online or online shopping websites use recommendations settings using unsupervised learning on possible items similar to the ones previously bought. Some example of unsupervised learning k-means (Alsabti, Ranka, & Singh, 1997), expectation-maximization algorithm (Moon, 1996; Nolen-Hoeksema, Morrow, & Fredrickson), and self-organizing map (Kohonen, 1990).

4.2.3 Reinforcement learning

In reinforcement learning the algorithm makes decisions and gets negative or positive feedback as error for each decision. It is also called reward based learning each wrong decision is penalized heavily while right decision is rewarded. The real world scenarios where robots learn to adapt functionality are an example of reinforcement learning.

4.2.4 Semi-supervised learning

Semi-supervised learning is a special form of learning. Classifiers typically need labeled data to train. But it is difficult to label instances, which require manual effort, and is time consuming especially when dealing with large amount of data. Unlabeled data on the other hand is easy to obtain. When training labels are present only for part of the data but absent for the rest, a combined supervised and unsupervised learning is employed called semi-supervised learning. Some examples include transductive support vector machines (J. Wang, Shen, & Pan, 2007) and graph-based methods (Chapelle et al., 2009).

4.3 TYPES OF ML ALGORITHMS

Machine learning applications can be categorized on the basis of the outcome as follows

4.3.1 Classification

The data is categorized into two or more classes it is termed as classification. Mostly classification problem uses supervised learning. There are several algorithms, which are used for classification problems in neuroimaging. In this work we use decision trees, which is described, in the section below.

4.3.1.1 Decision trees

Decision Trees (DTs) are learning is most widely used methods since they are very practical and simple (Mitchell, 1997). It is used for approximating discrete valued functions that is robust to noisy data and learning certain decision rules(Mitchell, 1997). The learned function is represented by the tree-like structure(Mitchell, 1997). Learned trees are set of if/then rules to improve the human readability. Each node in the tree specified a test of some feature of an instance/data. Each branch that descends from the node corresponds to one of the possible value of the feature. Classification of data is done by starting at the root node (beginning of the tree), testing the condition at the node and moving to the branch that satisfies the condition. This process is repeated for the next node of the subtree until it reaches the leaf node containing the categories (Mitchell, 1997). After the tree is built to its maximum length, a process called pruning is performed to reduce the tree to generalize the data.

Decision tree learning algorithms

The basic algorithm follows a top-down approach greedy search through the space of possible decision trees. There algorithms used in training a decision tree are discussed below:

Iterative Dichotomiser 3 (ID3) algorithm (J. Ross Quinlan, 1986) is most commonly used decision tree algorithm, which uses the information gain criteria. The tree is created through greedy manner where the feature that provides the largest information gain for the categories is chosen at each node.

C4.5 is an improvement from ID3 (J Ross Quinlan, 1996) algorithm, which can handle continuous and discrete features. In order to handle continuous features the algorithm creates a threshold and then creates a binary tree based on greater or less than threshold. This way the continuous features are discretized. The accuracy of each rule is used to order in which they are applied. Pruning is performed using the accuracy improves without a rule.

C5.0 is an updated version to C4.5 algorithm that improves on the speed and memory usage. C5.0 is more efficient in its memory usage and results in smaller and more accurate decision trees when compared to C4.5.

Classification and Regression trees (or CART) as the name suggests can produce either classification or regression trees depending on the outcome variable as discrete or continuous. It creates binary trees based on the information gain criterion.

Advantages of Decision tress

- The tree can be visualized and can be easily interpreted compared to other black box algorithms like neural networks.

- It replicates simple approach in which humans make decisions with the help of set of simple rules.

- It can be used for both regression and classification since it can handle categorical and numerical data.

- It can used for multiple output categories

- It does not involve an optimization of parameters

Drawbacks of decision trees

- Decision trees although simple can over-fit and might not generalize data well. But this problem can be overcome by pruning, setting certain parameters like minimal samples required at a node or the maximum depth of the tree.

- It has the problem of not attaining the global optimal decision tree due to the underlying greedy algorithm.

- With unbalanced data in each class, the decision trees can create biased trees

Decision tree mathematical formulation is given below (Pedregosa et al., 2011)

Given the training data $x_i \epsilon R_n, i = 1,2, ... N$ and a label vector $y \epsilon R^l$

Decision tree iteratively partitions the feature space such that data with same class are grouped together

At node m the data X is split θ using feature f and threshold t_m, partition the data as X_{left} or X_{right} subsets of data

$$X_{left}(\theta) = (x,y)|x_j \leq t_m$$

$$X_{right}(\theta) = X \backslash X_{left} \ (everything \ else \ not \ X_{left})$$

The impurity at each node is calculated using $H(\ )$,

$$H\left(X_{left}(\theta)\right) - impurity \ at \ left \ node; \ H\left(X_{right}(\theta)\right) - impurity \ at \ right \ node$$

$$G(X,\theta) = \frac{n_{left}}{N_m} H\left(X_{left}(\theta)\right) + \frac{n_{right}}{N_m} H(X_{right}(\theta))$$

The parameters that minimizes the impurity $G(X,\theta)$ are selected for the split at each node

Consider K classes, the proportion of classes observed at node m is given by,

$$p_{mk} = \frac{1}{N_m} \sum_{x_i \epsilon R_m} I(y_i = k)$$

The measure of impurity (Gini index) is given by,

$$\sum_k p_{mk}(1 - p_{mk})$$

And Entropy $= -\sum_k p_{mk} log(p_{mk})$

And,

Misclassification $= 1 - \max(p_{mk})$

4.3.2 Regression

Regression outcome involves predicting a continuous outcome measure and also use supervised learning. Simple regression uses one input or independent variable $x_i, i = 1,2..N$ to predict outcome Y_i.

$$Y_i = (\beta_0 + \beta_1 x_i) + \varepsilon_i$$

where β_0, β_1 $are\ intercept\ and\ slope\ respectively; \varepsilon_i - error\ term$

Multiple regression is an extension of simple regression with more than one independent variable.

$$Y_i = \left(\beta_0 + \beta_1 x_{i1} + \beta_2 x_{i2} \ldots \ldots + \beta_p x_{ip}\right) + \varepsilon_i$$

Partial least square (PLS) regression is a type of multiple regression and is a method for modeling multivariate measurements by means of latent variables. In general PLS creates orthogonal score vectors (latent variables) by maximizing covariance between the different sets if variables. Based on the response (outcome) variables there are two variants PLS1 (one response variable) and PLS2 (more than two response variables). The main advantage of this method is that it finds a parsimonious model even when the predictors are highly collinear or linearly dependent. There are two main algorithm approaches for PLS; non-linear iterative partial least squares (NIPALS) algorithm and another alternative algorithm called SIMPLS for calculating partial least squared regression.

In this work we use SIMPLS algorithm implemented in MATLAB for multivariate analysis and will be discussed in the following section (De Jong, 1993).

4.3.2.1 Partial least squares regression – SIMPLS algorithm

The main objective is to find a predictive linear model $\widehat{Y} = XB$ (De Jong, 1993). In order to stabilize the estimated parameters orthogonal factors are obtained for X as $t_a = X_0 r_a$ to maximize their covariance with corresponding factors of Y, $u_a = Y_0 q_a$ (a = 1,2,…..A). The first pair of singular vectors obtained using singular value decomposition (SVD) of S_0 and P_{a-1} were computed to obtain the solution for r_a and q_a (De Jong, 1993).

There are few constraints for the solutions (De Jong, 1993).

1) The weights r_a and q_a to maximize the covariance of scores t_a and u_a

$$u'_a t_a = q'_a (Y'_0 X_0) r_a$$

2) Normalization of weights, $r_a: r'_a r_a = 1$ and $q_a: q'_a q_a = 1$

3) Orthogonality of $t'_b t_a = 0$ for a>b

Basic concept of SIMPLS algorithm is explained using the pseudo code below described as mentioned in (De Jong, 1993)

Compute cross-product $S = X'_0 Y_0$

For a = 1,2,….A

a=1: compute single value decomposition (SVD) of S

a>1: compute SVD of $S - P(P'P)^{-1}P'S$

The weights r are obtained from the first left singular vector

The scores $t = X_0 r$ and loadings $p = \frac{X'_0 t}{t't}$ are computed and the r,t, and p are stored into R, T,P respectively

END

Compute regression coefficients $B_{PLS} = RT^- Y_0$

4.4 FEATURE SELECTION

The numbers of features are often large and it is important to identify the ones that contribute substantially to the prediction of the class labels. Feature selection aids the algorithm to use only informative features, is an important but not an essential step (Chu et al., 2012, Cuingnet et al., 2011). Feature selection can be performed using prior knowledge or automated methods. Some of the methods are described below:

4.4.1 Feature ranking

The feature ranking method uses statistical measures like Euclidean distance or chi-squared to see how the feature is difference between the group and which has the largest distance between two groups.

4.4.2 Forward Selection

Forward selection is an iterative method, which starts with one feature and keeps adding the feature which best, improves our model until additional of a variable that does not improve the model.

4.4.3 Recursive or exhaustive feature elimination

It is a greedy method, which uses every feature or subset of features in the model and obtains the best performing feature subset. It is iterative and repeatedly creates models to exhaust every feature or combination of features.

4.4.4 Backward elimination

Backward elimination is opposite to forward selection model starts with all features and removes one feature after another until the performance of the algorithm drops.

4.4.5 Embedded Methods

Embedded feature selection method can be implemented using machine-learning algorithms that have their own in-built feature selection. Regularization algorithms perform embedded feature selection.

4.4.5.1 Regularization

Regularization is a way to avoid overfitting by penalizing high-valued regression coefficients. In reduces parameters to obtain a simplified model, which will likely perform better at predictions. The model with the lowest mean squared error score is usually the best choice for prediction. Regularization is necessary because least squares regression methods can be unstable due to multicollinearity in the model.

Regularization works by biasing model parameters by particular values closer to zero. The bias is achieved by adding a *tuning parameter* to encourage those values:

L1 regularization

L1 regularization adds an L1 penalty equal to the absolute value of the magnitude of coefficients. In other words, it limits the size of the coefficients (β) . L1 can yield sparse models (i.e. models with few coefficients) where some coefficients can become zero.

Least **A**bsolute **S**hrinkage and **S**election **O**perator (LASSO) regression uses L1 penalty to generate parsimonious models (i.e. models with fewer parameters) especially good with data with multicollinearity. The regression performs both variable selection and regularization simultaneously using an additional penalty term which affects they value of coefficients of regression. The goal of the minimization algorithm

$$\min_{\beta_0, \beta} (\frac{1}{2v} \sum_{i=1}^{v} (y_i - \beta_0 - x_i^T \beta)^2 + \lambda \sum_{j=1}^{p} |\beta_j|)$$

The tuning parameter λ, controls the amount of shrinkage of coefficient terms. As the regularization parameter increase then bias increases and as it decreases then variance increases. When λ = 0, no coefficients are eliminated and the estimated model is equal linear regression. As λ increases, more coefficients are set to zero and eliminated.

L2 regularization

L2 regularization adds an additional L2 penalty, which is the square of the magnitude of coefficients. Here none of the coefficients are eliminated and all are shrunk by the same factor and hence will *not* yield sparse models. Ridge regression and SVMs use L2 regularization for obtaining optimized model. **Elastic nets** combine L1 & L2 methods.

4.5 BIAS-VARIANCE TRADE-OFF

Bias are assumptions made by a model to make the target function easier to learn. Algorithms which have a high bias have more assumptions on the target function and are fast to learn but less generalizable. Low bias has lower assumptions on the target function. For complex problems when these assumptions are not met they are less suitable. Machine learning algorithms

that have low bias are decision trees, k-Nearest Neighbors and SVM. While linear Regression, linear discriminant analysis and logistic regression are examples of high bias algorithms. Variance is the estimate the target function will change if different training data was used. The target function is estimated from the training data by a machine-learning algorithm, so we should expect the algorithm to have some variance. Machine learning algorithms that have a high variance are strongly influenced by the specifics of the training data. The parameter optimization of machine learning algorithms is often trying to balance between bias and variance. The trade-off between bias and variance is very important to create an optimized and generalized algorithm.

4.6 MACHINE LEARNING IN AD

Machine learning techniques provide tools to analyze neuroimaging data for inherent patterns in the data for classifying disease categories. Machine learning and pattern recognition techniques have been actively utilized to understand AD (Davatzikos et al. 2010; Davatzikos et al. 2008; Fan et al. 2008a; Vemuri et al. 2009). In particular classifiers have been used to discriminate AD patients from healthy control (F. Liu, Zhou, Shen, & Yin, 2014)and also conversion from MCI to AD (Richard, Schmand, Eikelenboom, Van Gool, & Alzheimer's Disease Neuroimaging, 2013). Structural MRI, positron emission tomography, cerebrospinal fluid biomarkers or a combination of multiple modalities have been used to extract features for classification. Machine learning and multivariate data analysis methods are helpful tools for analyzing multiple variables simultaneously. The combination of MRI, FDG-PET, CSF biomarkers (Walhovd et al., 2010), neuropsychological status exam scores (Walhovd et al.,

2010), and APOE genotype data (Walhovd et al., 2010) voxel-based morphometry (Hirata et al., 2005) have used too. There were wide variety of classifiers that were used for classification of AD or amyloid status. A linear support vector machine (SVM) classifier (Magnin et al., 2009), multiple-kernel (SVM) for multimodal data fusion (F. Liu et al., 2014), genetic algorithm (GA) (Beheshti, Demirel, Matsuda, & Alzheimer's Disease Neuroimaging, 2017), deep learning algorithms (Islam & Zhang, 2017; Spasov, Passamonti, Duggento, Lio, & Toschi, 2018), artificial neural networks, k-nearest neighbor and linear discriminant analysis. Regression methods have been used to for continuous monitoring of AD progression using clinical scores and imaging data. MRI (T1 and T2-weighted ratio)(Yasuno et al., 2017), PET (PiB) images have been classified using textural features amyloid, sparse k–means (Cohen et al., 2013) has generally been used to dichotomize PiB retention into presence/absence of amyloid (PiB+ and PiB-) (Cohen et al., 2013).

Textural features were applied to PET images for classification of AD (Garali, Adel, Bourennane, & Guedj, 2018) and also amyloid status (Cattell et al., 2016). The unique element of the AD prediction project in the current thesis is our focus on voxel-wise prediction of amyloid from MRI. These other studies have focused primarily on prediction of clinical status (i.e., AD or MCI). The focus on regional prediction of amyloid is important, as this may help identify pre-clinical AD

.

5.0 USE OF MULTIMODAL MAGNETIC RESONANCE IMAGING AND PATTERN RECOGNITION TECHNIQUE FOR AMYLOID PREDICTION

5.1 INTRODUCTION

Alzheimer's disease (AD) is a neurodegenerative disease about 5.7 million people in the US and has been identified as the most common cause of dementia in people 60 years and older (Alzheimer's, 2016). The disease is believed to begin with pathological changes like accumulation of amyloid protein; followed by tau protein tangles, hypometabolism, inflammation and brain atrophy several years before the cognitive and clinical symptoms set in (Jack et al., 2010; Sperling et al., 2011). As one of the earliest detectable pathological changes in AD, amyloid deposition is a primary target for prevention and treatment strategies(Weninger et al., 2016). In-vivo measurement of Aβ plaques is performed using positron emission tomography (PET)(Villemagne, 2016). There is increased evidence that PET based biomarkers (Aβ and hypo-metabolism), appear during the preclinical stages of AD (Cohen & Klunk, 2014; Jack et al., 2012; Marcus et al., 2014; Sperling et al., 2011) and can predict decline years before the onset of symptoms (Cohen & Klunk, 2014). In-vivo Aβ imaging is essential in definitive diagnosis of AD and important to improve early detection of AD (Adlard et al., 2014). However limited access and high cost restrict the use of amyloid PET scans.

Structural MRI is advantageous, as it is widely accessible and is relatively inexpensive. If MRI predictors of amyloid deposition could be defined, MRI could be used as a screening tool in large prevention studies and where frequent or repetitive amyloid imaging is necessary. It could be used to monitor progress in amyloid deposition and evaluate treatments. Greater levels of amyloid plaque in the brain are associated with worsened structural brain integrity. Aβ

deposition is associated with cortical thinning in parietal, posterior cingulate and precuneus regions (Becker, 2011) (Dore, 2013) and hippocampus (Dore, 2013) more specifically entorhinal cortex (Doherty, 2015). With progressing accumulation of Aβ, the structural integrity of the brain is affected.

Regional changes in brain structure quantified using changes in MR intensities can help predict regional amyloid deposition. The subtle changes in the local pattern of image intensity (textures) across voxels can be detected using image texture analysis (Maani, Yang, & Kalra, 2015). MRI texture analysis studies have shown promise in characterizing brain tumors (Zacharaki et al., 2009) (Bahadure, Ray, & Thethi, 2017), multiple sclerosis (Abbasian Ardakani, Gharbali, Saniei, Mosarrezaii, & Nazarbaghi, 2015) (Harrison et al., 2010) and epileptic seizure prediction (Suoranta et al., 2013) (de Oliveira, Betting, Mory, Cendes, & Castellano, 2013). Textural features were applied to PET images for classification of AD (Garali et al., 2018) and also amyloid status (Cattell et al., 2016). Quantitatively these textures in images can be captured using various spatial or frequency-based filters. There are multiple MR modalities that highlight different tissue properties in the brain. High-resolution T1-weighted images have shown great tissue contrasts from which summary measures like volume and thickness measurements and texture-based measures are obtained. T2-weighted imaging can help detect fluid accumulation in the brain (Vemuri et al., 2017). T2-weighted FLAIR helps visualize white matter lesions (WMLs) as hyperintensities (Moller et al.). These white matter hyperintensities (WMHs) are highly correlated with AD (Brickman, Muraskin, & Zimmerman, 2009; Kandel et al., 2016) and Aβ deposition (Noh et al., 2014; Park et al., 2014). The tissue magnetic susceptibility differences highlighted using susceptibility weight imaging (Moller et al.) helps visualize microbleeds. Clinically SWI has been used for visualizing vasculature in the brain which show T2*

differences in blood and surrounding tissues ((Di Ieva et al., 2015) (Hsu et al., 2017),(S. Liu et al., 2017),(Halefoglu & Yousem, 2018)). These microbleeds are also associated with AD (Sepehry, Lang, Hsiung, & Rauscher, 2016) and amyloid (Graff-Radford et al., 2018). By using voxel-level tissue textural differences from individual or a combination of MR modalities we could potentially estimate voxel-level amyloid burden.

In this study, we use intensity-based voxel-level imaging features extracted from both individual and a combination of modalities to predict voxel-level amyloid. We use regression models to perform amyloid status prediction across subjects (least absolute shrinkage and selection operator (LASSO) and partial least squares (PLS)) and amyloid change prediction within subjects (LASSO). Imaging data from fourteen subjects are used in the within subject prediction and thirty-five different subjects are used for the prediction across subjects. The machine learning algorithm takes advantage of the voxel-wise data. Thus, the effective sample size for machine learning is > 10,000 examples. The MRI based approach proposed here offers promise for characterizing voxel-level amyloid burden on cross-sectional data and also potentially tracking amyloid burden longitudinally.

5.2 METHODS

5.2.1 Parent Study and Participants

This study was part of an ongoing longitudinal study (Amyloid Pathology and Cognition in Normal Elderly, RF1 AG025516) at the University of Pittsburgh. This longitudinal study started in 2007 and used a 1.5T scanner at study onset. In 2011 the MR scanning for this study switched to a Siemens 3T TRIO MR scanner. For the current study we selected all subjects who

underwent at least one scan on the 3T TRIO scanner between 2011 and 2017). If they had more than one session on the 3T scanner then we chose the 1st scan that had all MR sequences (T1-weighted, T2-weighted, SWI, T2 FLAIR). Subjects (for amyloid change prediction, N=14 with two time-points; for amyloid status prediction across subjects, N=35) were scanned using both MRI and PET on separate visits. All subjects signed written informed consent approved by the University of Pittsburgh institutional review board.

5.2.2 MRI Acquisition

All MRI scanning was conducted using a 3T Siemens Trio (Munich, Germany) located at the MR Research Center at the University of Pittsburgh with a 12-channel head coil. An axial, whole brain (3D) MPRAGE was collected with echo time (TE)=2.98ms, repetition time (TR)=2300ms, flip angle (FA)=9, inversion time (Alzheimer's)=900ms, field of view (FOV)=256x240, 1.2x1x1 mm, and 160 slices. An axial, whole brain (2D) T2-weighted image was collected with TE=101ms, TR=5300ms, FA=150, TI=2500ms, FOV=256x256, 1x1x3 mm resolution, and 48 slices. An axial, whole brain (2D) FLAIR was collected with TE=90ms, TR=9160ms, FA=150, TI=2500ms, FOV=256x212, 1x1x3 mm resolution, and 48 slices. An axial, whole brain (2D) SWI was collected with TE=20ms, TR=28ms, FA=15, TI=300ms, FOV=230x179, 0.53x0.53x1.5 mm resolution, and 96 slices.

5.2.3 PET scanning: Pittsburgh Compound-B (PiB)

[11C] PiB was produced as previously described (Price 2005). PET imaging was conducted using a Siemens/CTI ECAT HR + (3D mode, 15.2 cm field-of-view, 63 planes, reconstructed image resolution ~ 6 mm FWHM). The participant's head was immobilized to

minimize head motion. PiB was injected intravenously (12–15 mCi, over 20 s, specific activity ~ 1–2 Ci/μmol) and PET scanning was performed at least 50-70 min post injection.

5.2.4 MRI Preprocessing

All data were preprocessed using statistical parametric mapping software (SPM12). All structural scans (T1-weighted, T2-weighted, FLAIR SWI) were linearly registered (normalized mutual information similarity metric and 4th degree B-spline interpolation) to the MPRAGE. These images were then segmented (using the multi-spectral segmentation that utilizes each channel to improve segmentation) into gray matter (GM), white matter (WM), cerebrospinal fluid (CSF), skull, soft-tissue, and air (outputs a probability map for each class). The GM, WM, and CSF were threshold at a probability of 0.1, and added to create an initial intracranial volume mask, which was then refined using an image filling algorithm as well as an image-closing (disk structuring element of 1 voxel) algorithm in MATLAB. The MPRAGE was then linearly registered (normalized mutual information similarity metric with 4th degree B-spline interpolation) to the PET image and that transformation was applied to all other structural scans as well as the GM, WM, and CSF segmentations.

5.2.5 PET Processing

PET data was corrected for photon attenuation, scatter, and radioactive decay. The final reconstructed PET image resolution was ~6 mm (transverse and axial) based on in-house point source measurements. If subject motion is present then the data is also corrected for inter-frame motion by applying a more extensive registration procedure prior to the PET to MR alignment. The structural MR was re-oriented along the anterior-posterior commissure and coregistering with summed PET images (40-70min or 50-70min) using automated image registration (Nelson

et al.; Woods, Mazziotta, & Cherry, 1993). After co-registration, ROIs defined on MR images and transferred to PET data. The ROI sampling is performed using ROITOOL (Interactive Data Language, Boulder,CO). Regional concentrations are transformed into units of standardize uptake values (SUV) using the injected dose and subject's mass. The SUV ratio (SUVR) is then calculated by dividing by the SUV of cerebellum.

Structural 3D MPRAGE MR series were used to define a hand-drawn set of regions as previously defined, which include frontal cortex (FRC; ventral and dorsal), anterior cingulate gyrus (ACG: subgenual and pregenual), anteroventral striatum (AVS), precuneus/posterior cingulate cortex (PRC; ventral, middle and dorsal thirds), parietal cortex (Miller et al.), lateral temporal cortex (LTC), and cerebellum (Bozzali et al.) (Cohen et al., 2009). A global PiB retention index reflecting cerebral amyloid is computed from a weighted average of the SUVR values from the six most relevant VOIs (ACG, FRC, LTC, PAR, PRC, and AVS). The subjects were classified as amyloid positive or negative using a threshold (1.51) that was determined using a sparse k-means cluster analysis (Cohen et al., 2013).

5.3 ALGORITHM OVERVIEW

Our overall approach is designed to take advantage of the high dimensionality of the within-subject imaging data to predict the MR-amyloid relationship. The MR-amyloid relationship developed within subject is used for prediction on longitudinal change in amyloid. We then generalize the MR-amyloid relationship across subjects, using the subject-level features, to dichotomize amyloid status (overview described in figure. 10).
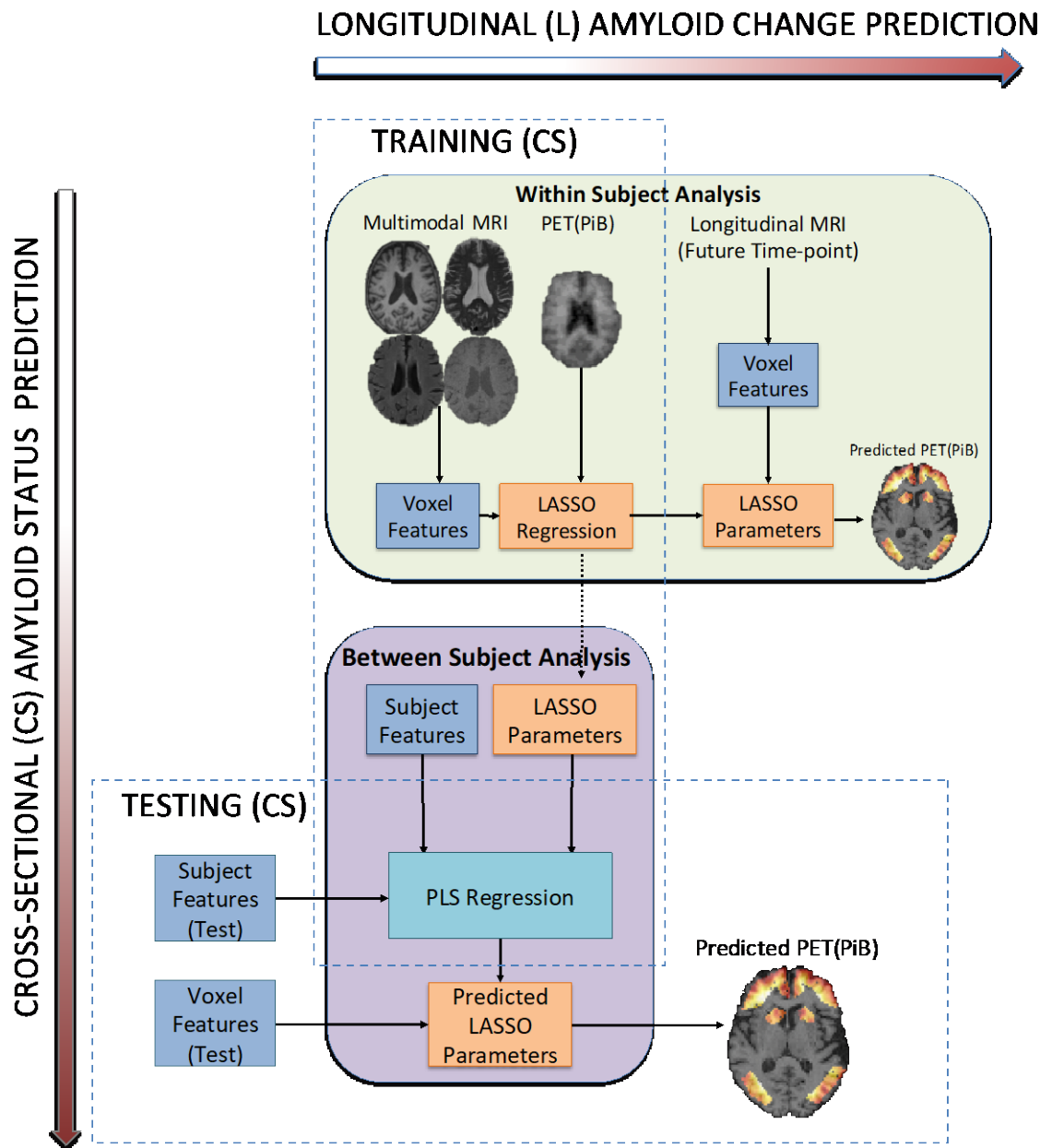
Figure 10 Overview of amyloid prediction

5.3.1 Determining voxel –level association between MR and Aβ

5.3.1.1 Feature Extraction

Features were obtained from MR modalities (i.e., T1, T2, T2 FLAIR and SWI). The specific imaging features used are intensity, 3D gradient, Gabor filter, local binary pattern (intensity-based neighborhood encoding method with detailed description in supplement). Texture can be described as fine or coarse, regular or irregular, and homogeneous or heterogeneous which can be captured using features like Gabor filters, local binary pattern, and 3D gradients. Gabor filters help characterizing homogeneity of texture in the spatial frequency domain. Local binary patterns are a unique way of encoding neighborhood intensity information. 3D gradients highlight regions with rapid change in intensities across voxels. MR signal intensities and Gabor filtered images were obtained from all modalities. 3D gradient features and local binary patterns (LBP) and are usually summarized as histograms. For highlighting voxel-level changes, these features will be most useful in T1-weighted imaging due to its high-resolution with clear contrast in intensities between gray matter and white matter. Hence the voxel-level LBP and 3D gradients are obtained only from T1-weighted imaging. Feature images were then registered to PET (PiB). A combined gray matter and white matter mask (GM+WM) was applied to each of these filtered images for obtaining the feature matrix (X_{vxF}; $F -$ $imaging\ features\ (F = 17\ (T1), 13(T2, T2 - FLAIR, SWI), v - voxels)$. The distributions of the features were skewed hence a $\log_{10}$ transform was performed.

Voxel-level features

The voxel-level features (figure 11) obtained from the MR images highlight distinguishable characteristics like intensity variations and changes. Features were extracted at the native resolution of each modality. Hence in addition to intensities and applying Gabor filters, local binary patterns and 3D gradients were obtained from T1-weighted imaging due to their high-resolution.
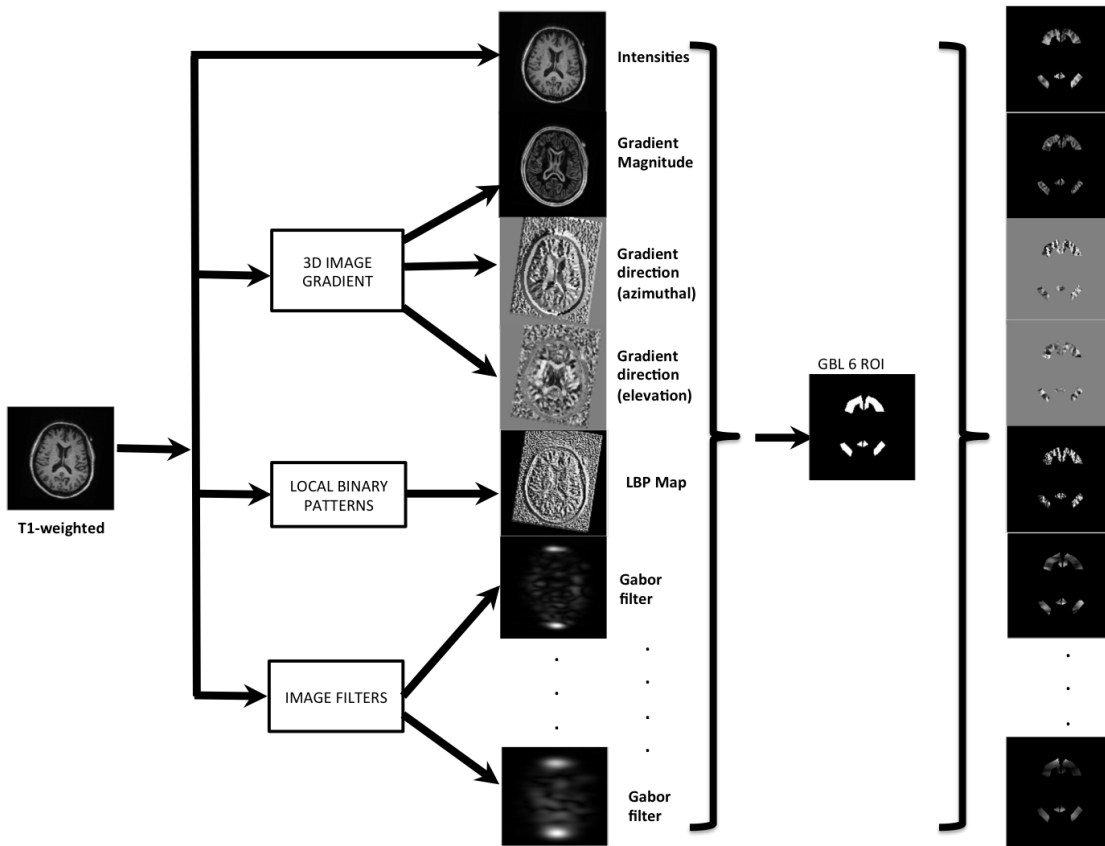
Figure 11 Voxel-level feature extraction for T1-weighted imaging: intensities, 3D gradient magnitude and directions, LBP map and Gabor filters.

Gabor filters

Gabor filters are linear frequency based filters, which highlight frequency contents in specific directions. Features constructed from responses of Gabor filters, Gabor features, have been successful in many computer vision and image processing applications face recognition, fingerprint matching. Gabor filter is the implementation of the Gabor transforms which is a short term Fourier transformation with Gaussian window for analysis in the spatial domain.

For obtaining the gabor residuals $u(x, y)$, convolution of an image $I(x, y)$ is done with 2D Gabor function $g(x, y)$ as represented by

Equation 1 Gabor residual u(Alzheimer's, 2016)

$$u(x, y) = \iint_{\delta} I(\alpha, \beta) g(x - \alpha, y - \beta) \, d\alpha \, d\beta$$

Where x, y are set of image points and α, β are the integrals

Where $g(x, y)$ is the Gabor function and is given by

Equation 2 Gabor function g(x,y)

$$g(x, y) = \exp\left(\frac{-x'^2 + \gamma^2 y'^2}{2\sigma^2}\right) \cos(2\pi \frac{x'}{\lambda} + \varphi)$$

where $x' = x\cos\theta + y\sin\theta, \ y' = -x\sin\theta + y\cos\theta$

They are defined using different parameters (sizes 4 and orientation [45, 90, 180, 270 degrees]) each of these highlighting the change in intensities at different orientations.

$\lambda -\ Wavelength\ of\ Gabor\ function\ cosine\ factor$

$\theta -\ Orientation\ of\ Gabor\ function$

$\varphi -\ Phase\ offset\ of\ the\ Gabor\ function\ coseine\ factor$

$\sigma -\ Standard\ deviation\ signal\ of\ Gaussian\ factor$

$\gamma -\ Ellipticity\ of\ the\ Gaussian\ factor$

3D Image Gradient: Gradient filter applies the 3D Sobel spatial filter that highlights the edges, which are sudden changes in intensity. Sobel filter is a spatial high pass filter that allows visualizing rapid changes in intensities. Sobel filter is convolved with the image to obtain the gradients (Gx Gy and Gz) in x-direction, y-direction and z-direction respectively.

$$Gx = \begin{pmatrix} -1 & 0 & 1 \\ -2 & 0 & 2 \\ -1 & 0 & 1 \end{pmatrix}, \ Gy = \begin{pmatrix} -1 & -2 & -1 \\ 0 & 0 & 0 \\ 1 & 2 & 1 \end{pmatrix}, \ Gz = \begin{pmatrix} -1 & 0 & 1 \\ -2 & 0 & 2 \\ -1 & 0 & 1 \end{pmatrix}$$

From these gradient vectors the gradient magnitude and angles (azimuthal and elevation) are computed.

$$Gradient\ Magnitude = \sqrt{G_x^2 + G_y^2 + G_z^2}$$

$$Gradient\ angle_{azimuthal} = \tan^{-1}\left(\frac{G_y}{G_x}\right) * \left(\frac{180}{\pi}\right)$$

$$Gradient\ angle_{elevation} = \tan^{-1}\left(\frac{G_y}{hypot(G_x, G_y)}\right) * \left(\frac{180}{\pi}\right)$$

Gradient elevation contains angles in degrees within the range [-90 90] measured between the radial line and the x-y plane while gradient azimuthal contains angles in degrees within the range [-180 180] measured between positive x-axis and the projection of the point on the x-y plane.

Local Binary Patterns: The local binary pattern is a texture-based feature which looks at its neighbors. Neighbors that are greater than the voxel value are coded as one and zero otherwise, and a binary value is generated (by going clockwise) – which is then converted to a decimal. Local binary patterns have been previously used for identifying these patterns in MRI (Maani, Kalra, & Yang, 2014; Oppedal, Eftestol, Engan, Beyer, & Aarsland, 2015). Figure 12. shows a 3x3 neighborhood, all values above 4 are considered 1, and rest are labeled 0. This generates a binary pattern clockwise as 11110000. The center value is then replaced with the decimal equivalent of the binary number. Based on the neighboring binary information spot, line edges/corners can be detected. The LBPs are individually obtained for each axial slice and then slices are combined to form the 3D feature image.
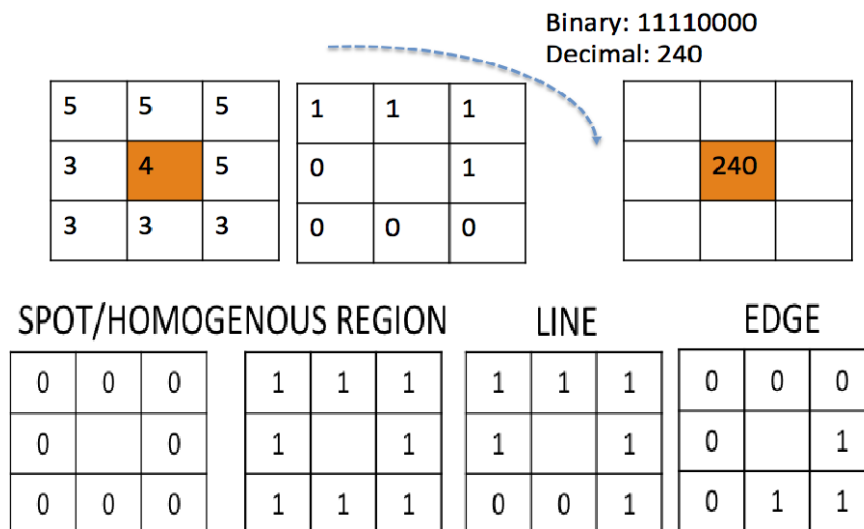
Figure 12 Local binary patterns

LASSO Model

LASSO is a regularized regression that penalizes the number of non-zero parameter estimates and allows for selection of features that are most predictive of the outcome. Features were extracted from voxels within combined gray matter (GM) and white matter (WM) mask (for training LASSO) and 6 volumes of interest (for prediction). For training, voxels from GM+WM mask (~20,000 for each subject) was used to allow space for greater variance in MR features and amyloid to improve the learning of the voxel-level MR-amyloid relationship. The prediction was performed on voxels within 6 VOIs. General equation for LASSO regression has a least square minimization term and penalization term for features that are most predictive, where λ is a regularization parameter, v is the total number of voxels, β_0, β intercept and slopes.

$$\min_{\beta_0,\beta}(\frac{1}{2v}\sum_{i=1}^{v}(y_i - \beta_0 - x_i^T\beta)^2 + \lambda\sum_{j=1}^{p}|\beta_j|)$$

The MR imaging feature matrix, X_{vxF} (where F are imaging features obtained from MR, v are voxels), is used to predict the amyloid (PiB SUVR), y_{vx1}. The regularization parameter λ was estimated via cross-validation using 5% of the voxels. The cross validation was performed by dividing the voxels into k sets and each time one set of voxels are used as test and rest of the voxels are used for training. All the voxels within each subject were then used to predict the LASSO parameters $\beta_0, \beta_1, \ldots \beta_F$. These LASSO model parameters can be applied to MR imaging of the same subject at a future time point for predicting amyloid change (2.6.1.1). The LASSO models can be generalized across subjects for predicting amyloid status (2.6.1.2).

2.6.1.1. Amyloid change prediction within subject

Subjects (N=13) with two time-points were randomized into 50 subsets showing equal decrease and increase in amyloid across the two time-points. All these subjects did not show clinically decreasing amyloid (N=4, show decrease in amyloid due to noise). However, for the purpose of validation we interchanged the chronologically occurring image data. For example if a subject shows increasing amyloid deposition (SUVR) from (timepoint 1 to timepoint 2) we interchanged to obtain a decreasing amyloid (timepoint 2 to timepoint 1). This was to show that at any time if we had the MR-PET data for a subject we can predict its later or previous amyloid to obtain its change. For each subject, LASSO parameters $(\beta_0, \beta_1, \dots \beta_F)$ were obtained from MR features and amyloid data from time-point 1 and applied on MR imaging features on time-point 2 to predict amyloid. Predicted voxel-level amyloid deposition can be obtained as a weighted sum of the MR imaging features.

$$y_{amyloid} = \beta_0 + X_1\beta_1 + X_2\beta_2 + \cdots + X_f\beta_f,$$

The change in mean SUVR (time-point 1 – time-point 2) was calculated for original and predicted amyloid image at the time point. The change in amyloid (mean SUVR) was labeled as a positive (decrease) or negative (increase) change. Each subset was evaluated using F-score and area under the curve (AUC). **F-score** was defined using **Precision** (positive prediction rate) $P = \frac{TP}{TP+FP}$ and **Recall** (specificity) $R = \frac{TP}{TP+FN}$, $F - score = \frac{2PR}{(P+R)}$.

2.6.1.2. Amyloid status prediction across subjects

Subject-level features of the training data include demographics (age, weight, sex, race), white matter hyper intensities (WMH), hippocampal volume, normalized gray matter and white matter.

Subject-level features

Participant demographics: Demographic information included features such as age, sex, race, education, weight, and height (Tang et al., 2015)

White Matter Hyperintensities (WMH): White matter segmentation includes a fuzzy seed based segmentation(M. Wu et al., 2006) that identifies hyper intensities in the FLAIR that corresponds to the white matter lesions (Debette & Markus, 2010(Gorelick, 2011 #1813)). These are often seen in healthy older adults, and are more extensive in individuals with dementia. The automated WMH segmentation method is an iterative algorithm that involves an automated selection of "seeds" of possible WMH lesions and fuzzy connectedness, which clusters voxels based on their adjacency and affinity, to segment WMH lesions around the seeds. Tahe fully automated WMH segmentation system was implemented in C++ and ITK. The total WMH volume divided by intracranial volume (ICV) was calculated as a marker of WMH burden.

Hippocampal Volume: Volume of the hippocampus is obtained using Automated Labelling Pathway algorithm. ALP produces voxel counts for a large number of anatomically defined brain regions, including all the Brodmann areas and subcortical structures, which have been hand-drawn on the atlas brain from the Montreal Neurological Institute (MNI).

Normalized gray matter and white matter: Gray matter and white matter probabilities were obtained using SPM12 (as described in 2.3. MRI preprocessing) and a binary image is obtained by using threshold of 0.6. Gray matter and white matter voxel counts were normalized by ICV.

Partial least squares (PLS) regression (described in chapter 5) was used to learn the relationship between subject-level features and LASSO parameters. Since there are a greater number of amyloid negative participants, we followed the cross-validation scheme established in previous literature (Mathotaarachchi et al., 2017) for rebalancing the data set. We split the data into subsets with equal representation of positives and negatives and for each subset all PiB+ (9) subjects were combined with random combinations of PiB- (9) subjects.

5.3.1.2 Stratified LOOCV for amyloid prediction across subjects

The subject-level analysis involves a nested leave-one-out-cross validation (LOOCV) with stratified rule for maintain balanced PiB+ and PiB- subjects. Each subset consists of 18 subjects (9 PiB- and 9 PiB+). There are two LOOCV loops, outer LOOCV, for amyloid status prediction and inner LOOCV for obtaining the threshold used for prediction. The outer LOOCV 17 subjects are used for training and 1 subject is left out. From 17 subjects, once again LOOCV is performed for predicting a threshold using linear regression. In the inner LOOCV, 16 subjects are used for training the PLS model and 1 subject is left out. Using subject features of left out test data and trained PLS model LASSO parameters are predicted. Predicted LASSO parameters are fit on the voxel level features from the test subject to obtain voxel-level amyloid prediction. This is repeated for all 17 subjects as test data and regression model is fit between mean original and predicted amyloid. Linear regression model acts as mapping from the original amyloid data

to the predicted data, by means of which the threshold is obtained. The voxel-level amyloid is predicted on the outer test data from PLS model (obtained on all 17 subjects) and the respective subject-level and voxel-level features.

The amyloid voxel-prediction through the subject-level learning method described above is shown in figure 13. (Note: The original amyloid PET (PiB) images are also normalized from 0 to 1 for representation)

5.3.1.3 Amyloid prediction using only subject-level features

Decision trees were used to see if the subject demographics, summary MR features alone and combined performed better than the voxel-level learning amyloid prediction. For this again a LOOCV scheme was used to obtain the evaluation metrics.
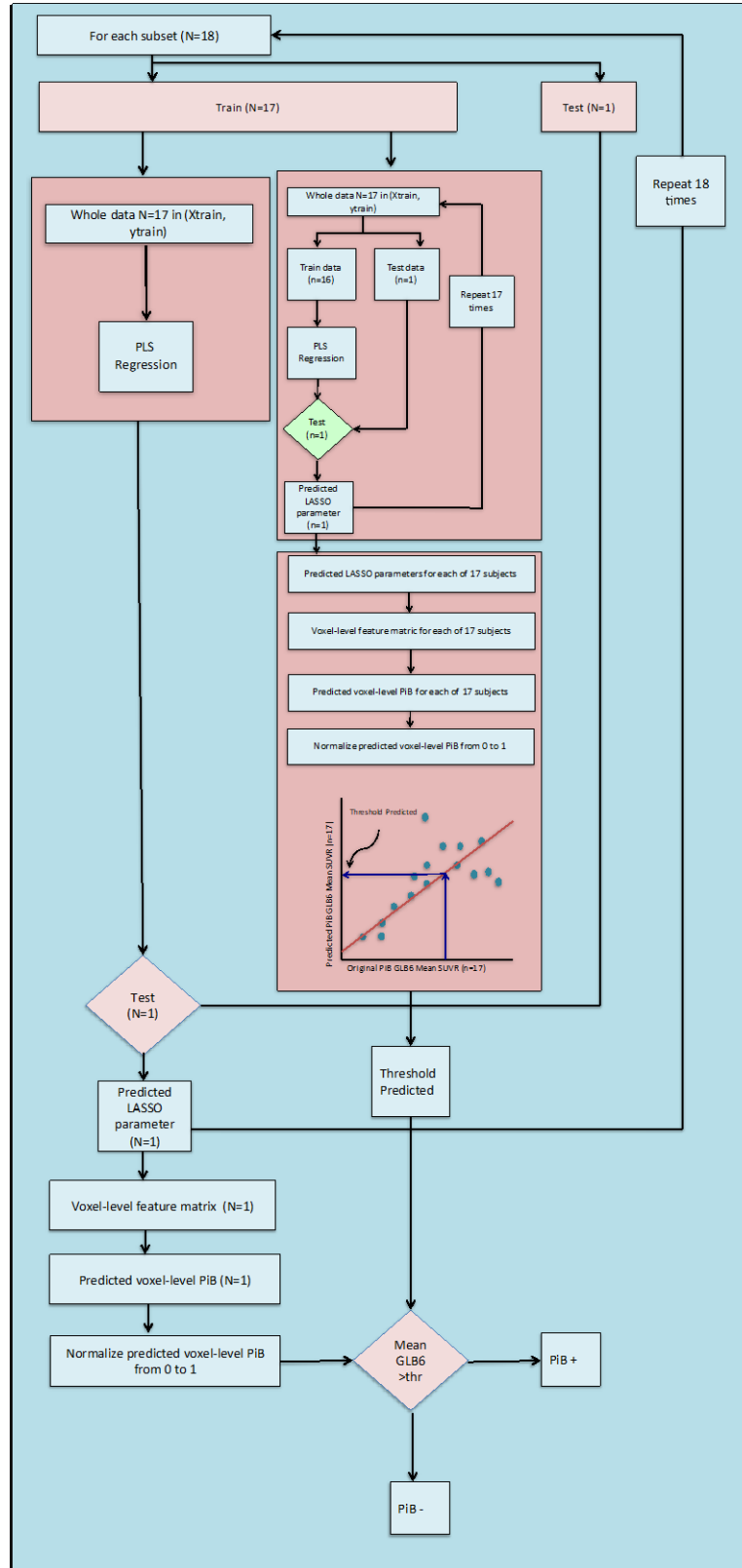
Figure 13 Subject-level analysis with nested LOOCV

5.4 RESULTS

5.4.1 Amyloid change prediction

The features from multimodal magnetic resonance imaging were able to predict regional amyloid. The original and the predicted change in amyloid images show similarities in regional distribution. T2-weighted imaging with SWI performed best for change in amyloid deposition [Average over 20 subsets: F-score (Mean (SD)): 79.67 (6.95), Accuracy (Mean (SD)): 78.57 (6.35); AUC 0.79 (0.06); Spearman correlation coefficient (Mean (SD)): 0.56 (0.06)] (Table 1.). Qualitatively normalized predicted amyloid images were comparable to the original amyloid image and could aid in visualization of brain regional amyloid distribution (figure 14).
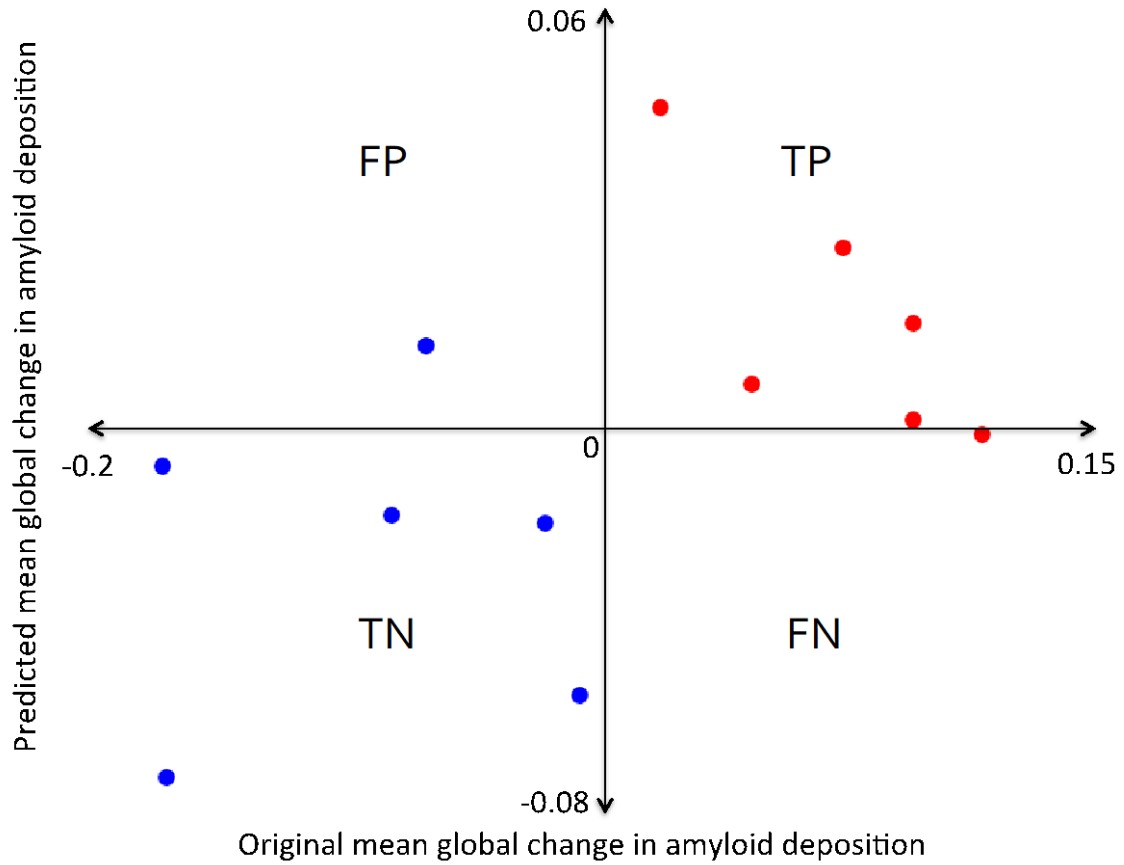
Figure 14 Mean global original and predicted change in amyloid deposition.

Colors represent the ground truth: original positive change (blue) original negative change

5.4.1.1 Evaluation of amyloid change prediction within subject for varying subsets

Subsets were created for N=20 (Table. 1), 50 (Table. 2), 100 (Table. 3), for evaluating the within subject model. The results were consistent across the subsets further confirming that the same combination of modalities (SWI, T2) has produced the best prediction

74

Table 1 Prediction performance of amyloid change prediction within subject using individual and combination of modalities (N=20)

Modality	Accuracy (Mean(SD))	F-score (Mean(SD))	AUC (Mean(SD))	Correlation (Mean(SD))	Rank
SWI, T2	78.75 (6.3263)	79.6845 (6.958)	0.7979 (0.0622)	0.5598 (0.0728)	1.5
T2-FLAIR, T2	72.5 (6.6776)	73.7903 (7.6315)	0.7343 (0.0667)	0.5734 (0.0584)	2
T2	71.6667 (7.3548)	72.162 (9.0372)	0.7286 (0.068)	0.7161 (0.0783)	2.5
T2-FLAIR	68.75 (9.3169)	71.2822 (9.5822)	0.6893 (0.0943)	0.3608 (0.1169)	4.75
T2-FLAIR, SWI	69.5833 (9.8509)	70.2075 (11.0028)	0.7079 (0.0944)	0.3486 (0.1172)	4.75
T2-FLAIR, SWI, T2	66.6667 (8.5498)	68.2839 (9.7638)	0.6729 (0.0832)	0.4329 (0.0883)	5.5
SWI	62.0833 (10.2865)	63.5483 (12.1263)	0.6264 (0.0967)	0.1776 (0.1289)	7
T1, T2-FLAIR, SWI, T2	56.6667 (9.2084)	60.2542 (13.1786)	0.56 (0.081)	0.0444 (0.1304)	8
T1, T2-FLAIR, T2	47.9167 (9.7013)	53.88 (12.2314)	0.4664 (0.0945)	-0.0678 (0.1592)	10.25
T1, SWI, T2	47.5 (9.0078)	57.4889 (9.2)	0.4457 (0.0908)	-0.0629 (0.1593)	10.5
T1, T2	47.5 (9.0078)	57.4889 (9.2)	0.4457 (0.0908)	-0.2427 (0.1635)	11
T1, T2-FLAIR	47.5 (10.5062)	56.8073 (12.9701)	0.4457 (0.0976)	-0.0822 (0.1763)	11.5
T1, SWI	45.4167 (8.3224)	57.2213 (8.2543)	0.4179 (0.082)	-0.1343 (0.2166)	12.5
T1, T2-FLAIR, SWI	43.3333 (10.3308)	52.1486 (12.3558)	0.41 (0.1001)	-0.078 (0.1429)	13.25
T1	37.5 (8.3333)	49.5198 (8.7967)	0.3429 (0.0813)	-0.4003 (0.1362)	15

Table 2 Prediction performance of amyloid change prediction within subject using individual and combination of modalities (N=50)

Modality	Accuracy (Mean(SD))	F-score (Mean(SD))	AUC (Mean(SD))	Correlation (Mean(SD))	Rank
SWI, T2	79.5 (6.7784)	81.2805 (6.46)	0.7991 (0.0673)	0.542 (0.062)	1.5
T2	72.5 (8.118)	74.1752 (8.9714)	0.7294 (0.083)	0.6905 (0.065)	1.75
T2-FLAIR, T2	72 (8.2065)	73.9718 (9.0248)	0.7223 (0.0797)	0.5796 (0.0748)	2.75
T2-FLAIR, SWI	69.3333 (7.9753)	70.5715 (8.746)	0.7029 (0.0796)	0.3389 (0.1012)	4.5
T2-FLAIR, SWI, T2	67.8333 (8.2496)	70.2416 (9.1351)	0.6803 (0.0802)	0.4164 (0.0786)	4.75
T2-FLAIR	64.6667 (7.8174)	68.1358 (8.1814)	0.6434 (0.0817)	0.3845 (0.1081)	5.75
SWI	62.3333 (8.6242)	63.383 (10.1886)	0.6326 (0.0855)	0.1506 (0.1166)	7
T1, T2-FLAIR, SWI, T2	56 (9.2275)	61.8473 (10.4893)	0.5457 (0.0901)	0.0379 (0.1435)	8
T1, T2-FLAIR	51.1667 (10.5153)	60.074 (10.7663)	0.4849 (0.1032)	-0.0789 (0.2014)	9.75
T1, T2-FLAIR, T2	49.6667 (10.5086)	56.3081 (10.7784)	0.4823 (0.106)	-0.0477 (0.1788)	11
T1, SWI, T2	50.5 (11.3452)	59.5261 (10.5015)	0.4791 (0.1137)	-0.0603 (0.1456)	11
T1, T2	50.5 (11.3452)	59.5261 (10.5015)	0.4791 (0.1137)	-0.262 (0.2175)	11.25
T1, T2-FLAIR, SWI	46.8333 (10.8966)	55.1048 (10.9655)	0.4477 (0.1084)	-0.0669 (0.1683)	13
T1, SWI	47.5 (11.5728)	58.5565 (10.0023)	0.4414 (0.1176)	-0.1867 (0.2763)	13
T1	36.8333 (11.6752)	47.8884 (12.1911)	0.3397 (0.1123)	-0.3996 (0.206)	15

Table 3 Prediction performance of amyloid change prediction within subject using individual and

combination of modalities (N=100)

Modality	Accuracy (Mean(SD))	F-score (Mean(SD))	AUC (Mean(SD))	Correlation (Mean(SD))	Rank
SWI, T2	78.4167 (6.0505)	79.8443 (6.1565)	0.7919 (0.061)	0.5309 (0.0802)	1.5
T2	72.0833 (7.7103)	73.7119 (8.6386)	0.7261 (0.0755)	0.6874 (0.0919)	2
T2-FLAIR, T2	72.0833 (7.7103)	73.979 (8.2535)	0.7253 (0.0793)	0.5606 (0.0825)	2.5
T2-FLAIR, SWI	69.3333 (8.1098)	69.6138 (9.5638)	0.7077 (0.0795)	0.3198 (0.1146)	4.5
T2-FLAIR, SWI, T2	66.25 (8.5719)	67.834 (9.8514)	0.669 (0.0842)	0.4062 (0.0891)	5
T2-FLAIR	66.25 (7.9786)	67.7664 (10.1285)	0.6679 (0.0777)	0.3612 (0.1229)	5.5
SWI	63.5833 (9.1483)	63.4589 (11.2531)	0.6499 (0.0901)	0.1506 (0.1256)	7
T1, T2-FLAIR, SWI, T2	54.25 (9.5122)	59.609 (10.1704)	0.5319 (0.0989)	0.0001 (0.1507)	8
T1, SWI, T2	49.5833 (11.26)	58.3576 (10.713)	0.4716 (0.1155)	-0.0948 (0.1625)	10
T1, T2	49.5833 (11.26)	58.3576 (10.713)	0.4716 (0.1155)	-0.2917 (0.221)	10.5
T1, T2-FLAIR	49.5833 (9.5768)	58.2196 (9.7141)	0.4716 (0.0983)	-0.1269 (0.213)	10.75
T1, T2-FLAIR, T2	47.3333 (10.783)	53.6804 (11.0455)	0.4609 (0.1126)	-0.0959 (0.2104)	11.75
T1, T2-FLAIR, SWI	45.5833 (10.6241)	53.4122 (11.071)	0.4373 (0.1086)	-0.1026 (0.1754)	13
T1, SWI	46.0833 (11.6326)	56.9367 (10.7016)	0.4287 (0.1181)	-0.1993 (0.2476)	13
T1	36.5833 (9.973)	48.1675 (9.7548)	0.3364 (0.101)	-0.4115 (0.1882)	15

5.4.1.2 Comparison of performance of unstandardized voxel-level features

Feature standardization makes the mean as 0 and standard deviation as 1 for each feature. The performance is poor overall modalities when the features are standardized. This could possibly be because the feature normalization or standardization could possibly restrict the outcome measure to a specific range of values. Table. 4 show the performance of amyloid change prediction within subject

Table 4 Prediction performance of amyloid change prediction within subject (with standardization of feature vectors) (N=20)

Modality	Accuracy (Mean(SD))	F-score (Mean(SD))	AUC (Mean(SD))	Correlation (Mean(SD))	Rank
T1, SWI, T2	61.0077 (12.4862)	57.9167 (11.3023)	0.5793 (0.1139)	0.2059 (0.1546)	4.25
T1, SWI	55.4995 (12.3661)	53.75 (10.6359)	0.5436 (0.1081)	0.2717 (0.1437)	4.5
SWI	62.9414 (10.6213)	62.0833 (7.8709)	0.6293 (0.0831)	0.1063 (0.1464)	4.5
SWI, T2	65.9817 (9.8925)	62.9167 (8.7505)	0.6279 (0.0964)	0.0479 (0.1692)	4.5
T2-FLAIR, SWI	55.4216 (11.1)	53.3333 (7.836)	0.5357 (0.0744)	0.2493 (0.1405)	5.75
T2-FLAIR	57.8251 (12.7447)	56.6667 (10.3308)	0.5729 (0.1064)	0.1273 (0.148)	6
T1, T2-FLAIR, SWI, T2	55.4216 (11.1)	53.3333 (7.836)	0.5357 (0.0744)	0.2678 (0.1604)	6.25
T1, T2-FLAIR, T2	53.6971 (11.7193)	52.5 (9.7857)	0.5329 (0.0995)	0.2276 (0.1405)	7.75
T1, T2-FLAIR, SWI	48.5085 (13.5847)	49.1667 (9.7107)	0.5043 (0.097)	0.3157 (0.1598)	8
T2-FLAIR, SWI, T2	51.2368 (12.8033)	50.4167 (9.9248)	0.5107 (0.108)	0.1629 (0.1322)	9.75
T1, T2-FLAIR	47.7003 (13.6701)	47.0833 (9.0785)	0.4779 (0.0861)	0.2822 (0.1324)	10
T1	47.7003 (13.6701)	47.0833 (9.0785)	0.4779 (0.0861)	0.2262 (0.1124)	10.5
T2	54.0003 (12.5513)	48.75 (8.6666)	0.4764 (0.0803)	-0.1657 (0.1091)	11.75
T1, T2	47.1591 (11.9243)	44.5833 (10.5669)	0.4479 (0.1131)	0.1801 (0.1349)	12.75
T2-FLAIR, T2	45.5173 (13.3897)	43.75 (9.3169)	0.4393 (0.0974)	0.1633 (0.1473)	13.75

5.4.2 Amyloid status prediction

Image texture features from T1-weighted image modality alone performed the best [Average over 20 subsets: F-score (Mean (SD)): 68.2515 (7.5785), Accuracy (Mean (SD)): 66.3889 (8.156), AUC 0.6639 (0.0816); Spearman correlation coefficient (Mean (SD)): 0.4062 (0.1304)] when compared to the other modalities in the prediction of amyloid status. Figure 15 shows the mean original and the predicted amyloid for one subset (18 subjects) where each subject shown is a left out test data. Figure 16 shows the predicted amyloid change for one subject (voxels within ROIs) where each subject shown is a left out test data. The threshold is predicted for each left-out subject using the nested LOOCV, for figure representation the mean predicted threshold is used (0.64).
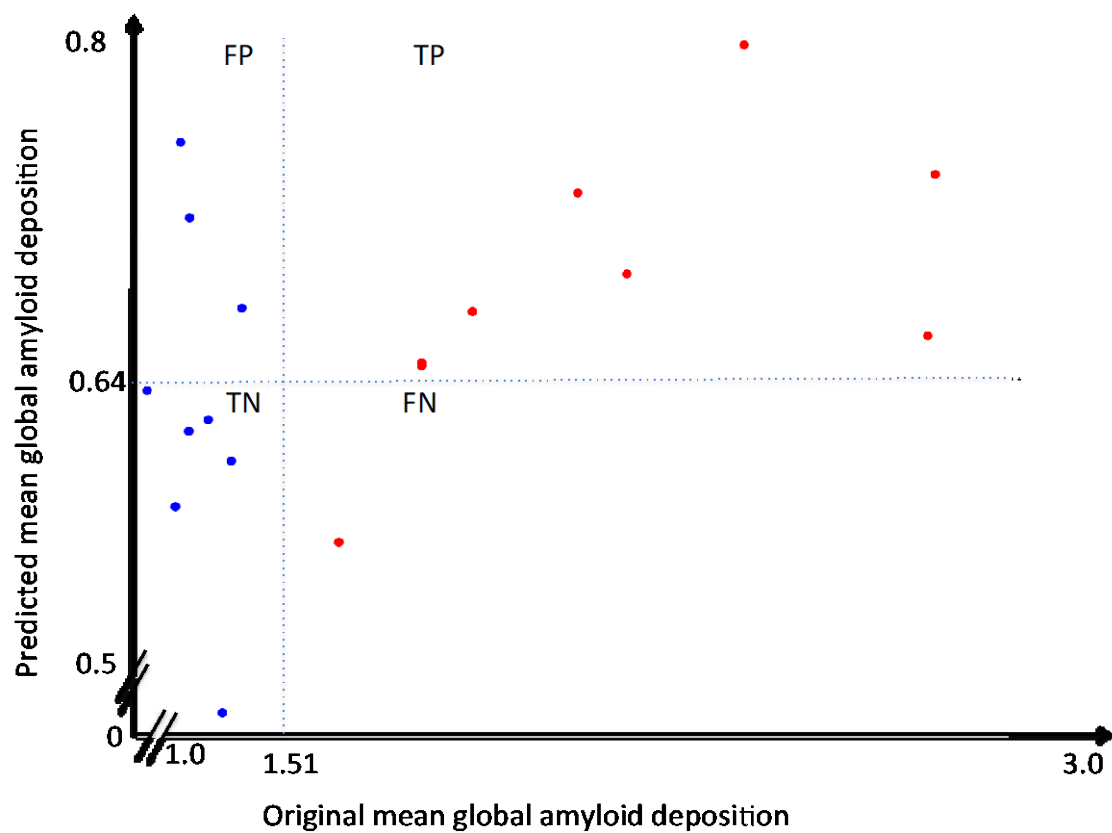
Figure 15 Mean global amyloid (within 6 ROIs)

Deposition in original and predicted, original threshold (1.51) and predicted threshold (0.64) for

classification. Colors represent the ground truth: original PiB- (blue) original PiB+
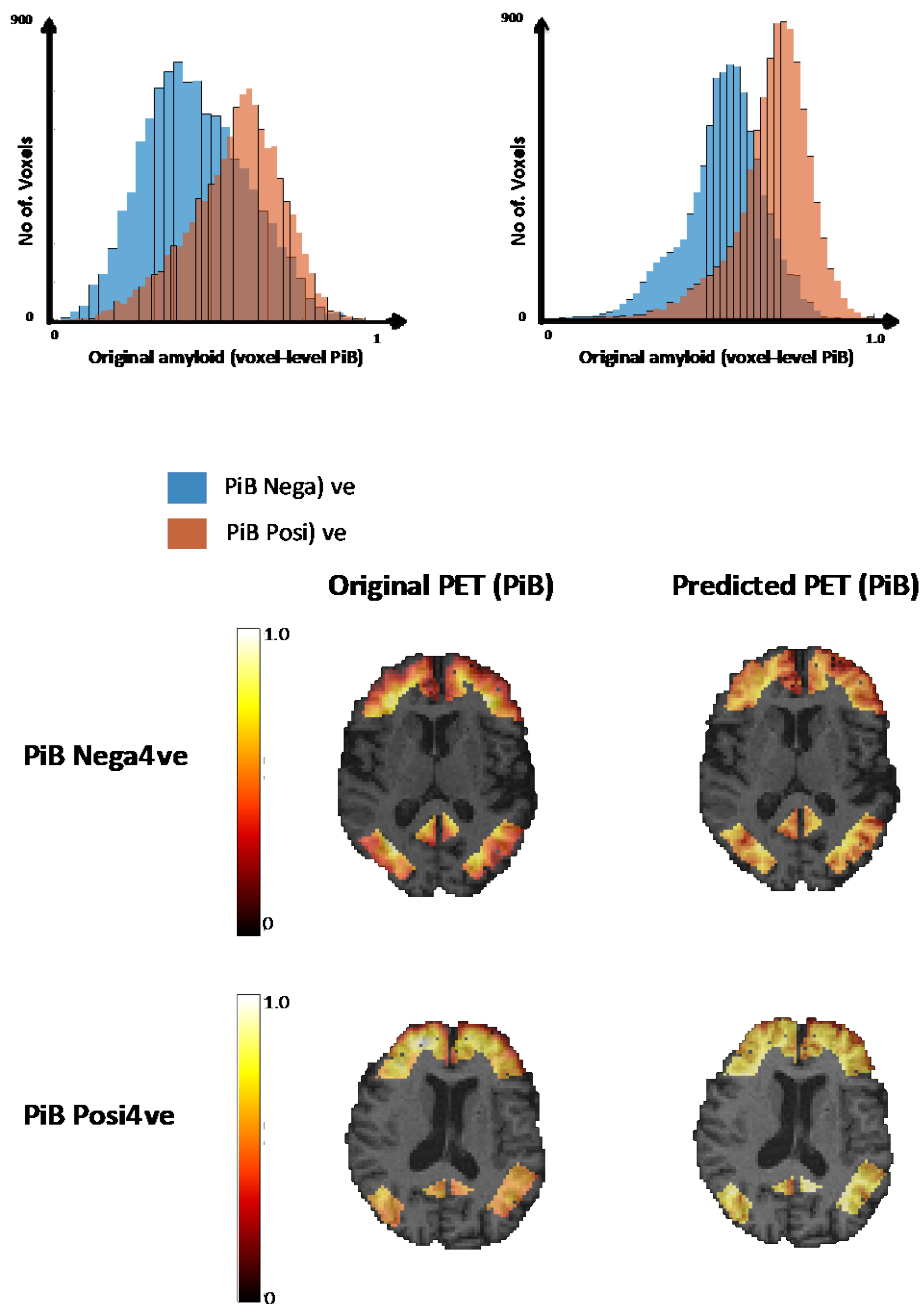
Figure 16 Amyloid prediction voxel-level for PiB + and PiB-

For subjects using T1-weighted, T2-FLAIR and SWI modality combination

5.4.2.1 Evaluation of amyloid status prediction across subject for varying subsets

Subsets were created for N=20 (Table. 6), 50 (Table. 7), 100 (Table. 8), for evaluating the within subject model. The results show that the combination of modalities of T1, T2-FLAIR, and SWI has produced the best prediction for amyloid status prediction.

Table 5 Prediction performance of amyloid status prediction across subjects (N=20)

Modality	Accuracy (Mean (SD))	F-score (Mean (SD))	AUC (Mean (SD))	Correlation (Mean (SD))	Rank
T1, T2-FLAIR, SWI	66.3889 (8.156)	68.2515 (7.5785)	0.6639 (0.0816)	0.4062 (0.1304)	1.75
T1, T2-FLAIR, SWI, T2	62.5 (5.944)	65.2339 (5.8338)	0.625 (0.0594)	0.5149 (0.1182)	1.75
T1, SWI, T2	61.6667 (8.4351)	62.7281 (7.8413)	0.6167 (0.0844)	0.4331 (0.0929)	2.75
T1, SWI	60 (5.8684)	62.5059 (5.0989)	0.6 (0.0587)	0.4234 (0.1102)	3.75
T1, T2-FLAIR	57.7778 (4.5599)	60.8743 (3.4693)	0.5778 (0.0456)	0.2151 (0.1446)	5.25
T1, T2-FLAIR, T2	56.3889 (6.315)	59.2849 (5.0149)	0.5639 (0.0632)	0.2147 (0.1534)	6.75
T1	57.5 (11.58)	59.058 (12.7522)	0.575 (0.1158)	0.2026 (0.1882)	6.75
T1, T2	54.1667 (9.8519)	56.9431 (10.9666)	0.5417 (0.0985)	0.2465 (0.162)	7.25
T2-FLAIR, T2	47.7778 (7.2994)	48.1942 (7.7464)	0.4778 (0.073)	-0.0146 (0.1499)	9.75
T2-FLAIR, SWI	42.7778 (6.0052)	47.1967 (5.0279)	0.4278 (0.0601)	0.1305 (0.1003)	11.25
T2-FLAIR	44.7222 (6.3663)	46.4126 (5.026)	0.4472 (0.0637)	0.0659 (0.1509)	11.25
T2-FLAIR, SWI, T2	43.0556 (7.4044)	47.0802 (9.0374)	0.4306 (0.074)	0.0293 (0.1057)	11.5
T2	45 (11.3855)	42.5152 (13.8145)	0.45 (0.1139)	-0.1788 (0.1781)	12.5
SWI, T2	41.6667 (8.5498)	46.5526 (8.4107)	0.4167 (0.0855)	-0.064 (0.1425)	13.75
SWI	41.9444 (7.7474)	44.2675 (9.1098)	0.4194 (0.0775)	-0.086 (0.1875)	14

Table 6 Prediction performance of amyloid status prediction across subjects (N=50)

Modality	Accuracy (Mean (SD))	F-Score (Mean (SD))	AUC (Mean (SD))	Corr (Mean (SD))	Rank
T1, T2, FLAIR, SWI	58.11 (7.29)	60.47 (7.10)	0.58 (0.07)	0.46 (0.11)	1.75
T1, FLAIR, SWI	60.00 (6.92)	61.57 (6.28)	0.60 (0.07)	0.39 (0.13)	1.75
T1, SWI	56.78 (7.04)	59.29 (6.68)	0.57 (0.07)	0.41 (0.12)	3
T1, T2 SWI	56.44 (8.50)	57.18 (8.84)	0.56 (0.09)	0.41 (0.10)	3.75
T1	55.56 (8.98)	58.14 (8.83)	0.56 (0.09)	0.22 (0.16)	5.25
T1, T2	53.44 (8.09)	56.13 (8.14)	0.53 (0.08)	0.28 (0.17)	6.5
T1, FLAIR	55.11 (5.36)	57.12 (4.66)	0.55 (0.05)	0.20 (0.15)	6.5
T1, T2, FLAIR	53.11 (6.93)	56.07 (5.96)	0.53 (0.07)	0.25 (0.14)	7.5
T2, FLAIR	46.89 (7.20)	48.94 (6.60)	0.47 (0.07)	0.02 (0.14)	10.25
FLAIR	45.56 (6.04)	47.11 (4.97)	0.46 (0.06)	0.11 (0.13)	10.5
T2, FLAIR, SWI	42.67 (8.94)	46.26 (10.11)	0.43 (0.09)	0.03 (0.11)	11.75
T2	47.67 (9.06)	44.50 (12.01)	0.48 (0.09)	-0.16 (0.17)	11.75
T2, SWI	41.56 (7.47)	46.66 (8.27)	0.42 (0.07)	-0.04 (0.13)	12.5
FLAIR, SWI	41.44 (5.17)	45.96 (5.12)	0.41 (0.05)	0.13 (0.10)	12.75
SWI	41.44 (6.94)	44.34 (6.99)	0.41 (0.07)	-0.09 (0.16)	14.5

Table 7 Prediction performance of amyloid status prediction across subjects (N=100)

Modality	Accuracy (Mean (SD))	F score (Mean (SD))	AUC (Mean (SD))	Corr (Mean (SD))	Rank
T1, FLAIR, SWI	61.39 (7.91)	62.52 (7.69)	0.61 (0.08)	0.45 (0.13)	1.5
T1, T2, FLAIR, SWI	60.17 (8.36)	62.47 (8.08)	0.60 (0.08)	0.51 (0.10)	2
T1, SWI	59.39 (8.68)	62.13 (7.96)	0.59 (0.09)	0.46 (0.14)	3.5
T1	60.06 (9.06)	62.48 (8.95)	0.60 (0.09)	0.27 (0.14)	3.75
T1, T2, SWI	57.44 (8.77)	58.47 (8.34)	0.57 (0.09)	0.45 (0.10)	4.75
T1, FLAIR	55.78 (5.58)	58.26 (4.66)	0.56 (0.06)	0.26 (0.12)	6.5
T1, T2, FLAIR	55.50 (6.68)	58.09 (5.76)	0.56 (0.07)	0.31 (0.14)	6.75
T1, T2	53.89 (8.78)	56.68 (9.08)	0.54 (0.09)	0.32 (0.15)	7.25
T2, FLAIR	48.33 (6.58)	50.06 (5.90)	0.48 (0.07)	0.08 (0.12)	9.5
FLAIR	46.44 (5.09)	47.80 (4.42)	0.46 (0.05)	0.16 (0.11)	10.5
T2, FLAIR, SWI	44.00 (8.04)	48.70 (9.52)	0.44 (0.08)	0.04 (0.11)	11.5
T2	46.94 (8.18)	44.31 (10.72)	0.47 (0.08)	-0.14 (0.17)	12.25
FLAIR, SWI	40.83 (6.67)	44.68 (7.19)	0.41 (0.07)	0.14 (0.11)	12.75
T2, SWI	42.00 (6.57)	46.98 (6.78)	0.42 (0.07)	-0.04 (0.12)	12.75
SWI	40.72 (7.02)	43.65 (7.40)	0.41 (0.07)	-0.10 (0.15)	14.75

5.4.2.2 Feature ranking of textural features

The voxel level features are unstandardized hence the model comparison is performed using feature ranking through forward selection. It can be seen in Table. 7, that T1-weighted textural features alone shows high performance but with the help of additional SWI and T2-weighted FLAIR the correlation is also higher between the original and prediction mean amyloid deposition.

Table 8 Ranking of features T1, T2-weighted FLAIR, SWI modalities for amyloid status prediction

Feature	Accuracy (Mean (SD))	F-score (Mean (SD))	AUC (Mean (SD))	Corr (Mean(SD))	Rank
T1(all), flair(all), swi(int, G[4,0:270], G[8,0:270])	62.22 (7.56)	63.49 (7.00)	0.62 (0.08)	0.40 (0.15)	3.25
T1(all), flair(all), swi(int, G[4,0:270], G[8,0:180])	61.94 (7.71)	63.32 (7.09)	0.62 (0.08)	0.40 (0.14)	4.5
T1(all), flair(all), swi(int, G[4,0:90], G[8,0:90])	61.67 (7.63)	63.15 (7.04)	0.62 (0.08)	0.41 (0.13)	4.75
T1 (int, G[4,0:360], G[8,0:360], Gaz, Gelev, Gmag)	62.22 (7.34)	65.69 (7.13)	0.62 (0.07)	0.27 (0.15)	5.25
T1(all), flair(all), swi(int, G[4,0:180], G[8,0:90])	61.67 (7.63)	63.15 (7.04)	0.62 (0.08)	0.41 (0.14)	5.75
T1(all), flair(all), swi(int, G[4,0:180], G[8,0:180])	61.67 (7.63)	63.15 (7.04)	0.62 (0.08)	0.40 (0.14)	7.25
T1 (int, G[4,0:360], G[8,0:360], Gaz, Gelev, Gmag, LBP)	61.67 (10.02)	65.03 (9.39)	0.62 (0.10)	0.26 (0.17)	7.25
T1(all), flair(all), swi(int, G[4,0:360], G[8,0:270])	61.67 (7.63)	63.15 (7.04)	0.62 (0.08)	0.41 (0.13)	7.5
T1(all), flair(all), swi(int, G[4,0:90], G[8,0:45])	60.00 (6.40)	61.91 (5.88)	0.60 (0.06)	0.42 (0.12)	9.25
T1(all), flair(all), swi(int, G[4,0:360], G[8,0:360])	61.67 (7.63)	63.15 (7.04)	0.62 (0.08)	0.40 (0.14)	9.25
T1(all), flair(int, G[4,0], G[8,0])	60.00 (7.34)	63.26 (6.70)	0.60 (0.07)	0.36 (0.12)	9.5
T1(all), flair(all), swi(int, G[4,0:45], G[8,0:45])	58.61 (6.11)	60.65 (5.73)	0.59 (0.06)	0.39 (0.11)	12.5
T1 (int, G[4,0:45], G[8,0:45])	60.83 (7.09)	64.22 (6.77)	0.61 (0.07)	0.16 (0.16)	13.25
T1(all), flair(all), swi(int, G[4,0])	58.33 (7.54)	60.91 (7.04)	0.58 (0.08)	0.35 (0.10)	13.5
T1(all), flair(int, G[4,0:45], G[8,0])	58.06 (7.75)	61.60 (6.80)	0.58 (0.08)	0.33 (0.11)	14.5
T1(all), flair(int, G[4,0])	57.50 (9.24)	60.21 (8.66)	0.58 (0.09)	0.30 (0.15)	16.5
T1(all), flair(Int)	57.50 (9.58)	60.03 (9.62)	0.58 (0.10)	0.30 (0.16)	17
T1(all), flair(int, G[4,0:180], G[8,0:90])	56.94 (6.71)	59.40 (5.60)	0.57 (0.07)	0.25 (0.14)	20
T1(all), flair(int, G[4,0:90], G[8,0:90])	56.67 (6.40)	59.22 (5.41)	0.57 (0.06)	0.25 (0.14)	22.25
T1(all), flair(int, G[4,0:270], G[8,0:180])	56.67 (6.40)	59.22 (5.41)	0.57 (0.06)	0.25 (0.14)	23.5
T1(all), flair(int, G[4,0:180], G[8,0:180])	56.67 (6.40)	59.22 (5.41)	0.57 (0.06)	0.24 (0.14)	23.75
T1 (int, G[4,0])	58.06 (9.95)	58.21 (10.55)	0.58 (0.10)	0.23 (0.17)	24
T1(all), flair(int, G[4,0:270], G[8,0:270])	56.67 (6.40)	59.22 (5.41)	0.57 (0.06)	0.25 (0.14)	25
T1(all), flair(int, G[4,0:360], G[8,0:360])	56.67 (6.40)	59.22 (5.41)	0.57 (0.06)	0.25 (0.14)	25.75
T1(all), flair(int, G[4,0:360], G[8,0:270])	56.67 (5.87)	59.19 (5.06)	0.57 (0.06)	0.24 (0.14)	26.75
T1(all), flair(all), swi(Int)	56.11 (6.72)	58.49 (5.41)	0.56 (0.07)	0.36 (0.10)	27.25
T1 (int, G[4,0:45], G[8,0])	56.11 (6.22)	59.82 (5.84)	0.56 (0.06)	0.13 (0.18)	27.25
T1 (int, G[4,0:270], G[8,0:270])	56.39 (10.08)	59.98 (9.50)	0.56 (0.10)	0.10 (0.19)	27.25
T1 (int, G[4,0:360], G[8,0:360])	56.39 (9.92)	59.74 (9.44)	0.56 (0.10)	0.10 (0.20)	28
T1 (int, G[4,0:360], G[8,0:270])	56.11 (10.49)	59.86 (9.65)	0.56 (0.10)	0.10 (0.19)	28.25
T1(all), flair(all), swi(int, G[4,0:45], G[8,0])	55.83 (6.86)	59.03 (6.78)	0.56 (0.07)	0.33 (0.12)	29.25
T1 (int, G[4,0:90], G[8,0:45])	55.83 (8.16)	59.39 (6.75)	0.56 (0.08)	0.15 (0.19)	29.5
T1 (int, G[4,0:180], G[8,0:180])	56.11 (9.86)	59.36 (9.45)	0.56 (0.10)	0.10 (0.19)	30.75
T1 (int, G[4,0:360], G[8,0:360], Gaz)	55.83 (9.45)	59.36 (9.12)	0.56 (0.09)	0.11 (0.19)	31.5
T1 (int, G[4,0:360], G[8,0:360], Gaz, Gelev)	55.83 (10.43)	59.32 (10.35)	0.56 (0.10)	0.12 (0.18)	31.75
T1(all), flair(all), swi(int, G[4,0], G[8,0])	54.17 (6.71)	57.73 (6.15)	0.54 (0.07)	0.30 (0.11)	34.5
T1 (int, G[4,0:270], G[8,0:180])	55.56 (10.35)	59.10 (9.67)	0.56 (0.10)	0.10 (0.19)	35.75
T1(all), flair(int, G[4,0:45], G[8,0:45])	55.00 (5.38)	57.32 (4.95)	0.55 (0.05)	0.19 (0.14)	36.5
T1(all), flair(int, G[4,0:90], G[8,0:45])	54.72 (6.32)	57.05 (5.14)	0.55 (0.06)	0.18 (0.15)	37.5
T1 (int, G[4,0:90], G[8,0:90])	55.28 (9.10)	58.71 (8.75)	0.55 (0.09)	0.10 (0.19)	37.5
T1 (int, G[4,0:180], G[8,0:90])	55.28 (8.92)	58.42 (8.92)	0.55 (0.09)	0.09 (0.19)	38.75
T1 (int, G[4,0], G[8,0])	52.78 (6.86)	52.76 (6.43)	0.53 (0.07)	0.11 (0.13)	40.25
T1(Int)	52.22 (6.35)	55.38 (6.26)	0.52 (0.06)	-0.16 (0.17)	42.75

5.4.2.3 Comparison of performance of standardized and unstandardized feature vectors

Table 9 Prediction performance of amyloid status prediction across subjects (with standardization of voxel-level features) (subsets N = 20)

Modality	Accuracy (Mean (SD))	F-score (Mean (SD))	AUC (Mean (SD))	Correlation (Mean (SD))
T1	49.7222 (6.3663)	51.5003 (7.2656)	0.4972 (0.0637)	0.2683 (0.1469)
T2-FLAIR	45.2778 (4.5152)	50.1838 (2.7544)	0.4528 (0.0452)	-0.0415 (0.1545)
SWI	36.6667 (6.5981)	36.0238 (4.7305)	0.3667 (0.066)	-0.1261 (0.1649)
T2	59.4444 (9.3832)	57.9424 (10.7838)	0.5944 (0.0938)	0.0653 (0.1068)
T1, T2-FLAIR	50.8333 (8.8807)	54.0568 (8.0373)	0.5083 (0.0888)	0.1537 (0.143)
T1, SWI	42.7778 (5.4373)	43.4469 (4.3509)	0.4278 (0.0544)	0.1902 (0.0744)
T1, T2	46.3889 (8.507)	49.1988 (8.7596)	0.4639 (0.0851)	0.1453 (0.1554)
SWI, T2	48.3333 (11.6952)	50.8534 (10.5125)	0.4833 (0.117)	-0.0414 (0.152)
T2-FLAIR, T2	39.4444 (8.0407)	42.9754 (9.0404)	0.3944 (0.0804)	-0.1539 (0.1588)
T2-FLAIR, SWI	34.4444 (8.9399)	35.4315 (8.7638)	0.3444 (0.0894)	-0.0548 (0.172)
T1, SWI, T2	53.6111 (7.2715)	51.5686 (7.5605)	0.5361 (0.0727)	0.1633 (0.1322)
T1, T2-FLAIR, SWI	45.5556 (5.8684)	42.6909 (5.3114)	0.4556 (0.0587)	0.2168 (0.0874)
T1, T2-FLAIR, T2	53.8889 (7.8774)	58.2523 (5.7186)	0.5389 (0.0788)	0.1473 (0.1387)
T2-FLAIR, SWI, T2	43.3333 (8.7563)	44.514 (9.9204)	0.4333 (0.0876)	-0.1434 (0.1509)
T1, T2-FLAIR, SWI, T2	49.4444 (6.7201)	46.3276 (7.9058)	0.4944 (0.0672)	0.1903 (0.1172)

5.4.3 Amyloid prediction using subject-level features

The F-scores were less than the predicted amyloid from our method [F-score (Mean (SD)) (20 subsets): demographics only = 0.55(0.16), MR only = 0.57(0.16), Demographics and MR = 0.54(0.18)]. The other machine learning classifiers (SVM and Logistic regression) using demographics and MR as features were not effective, perhaps because there was insufficient data for learning.

5.5 DISCUSSION

The different MR imaging modalities carry complementary information about regional structural integrity. Several imaging features, from each of these modalities, were combined in a two-level approach (voxel-level and subject-level) to estimate amyloid status across subjects and estimate within-subject change in amyloid. Results of our analyses demonstrate that estimation of amyloid deposition could be successfully achieved using individual or a combination of MR modalities. In our approach subject-level learning involved generalizing the LASSO parameters across subjects, hence inter-subject registration using template normalization – which can introduce variability – was not required. The approach predicts voxel-level amyloid, which can aid in both qualitative and quantitative analysis of regional amyloid burden.

The combination of T2-weighted imaging and SWI had the highest prediction for amyloid change. SWI is a T2*-based contrast that exploits inherent magnetic inhomogeneity from magnetic susceptibility differences between tissues. T2 and T2* based contrast might capture the tissue changes (Haacke et al., 2009), including loss of integrity or iron deposition in neuritic plaques (Chamberlain et al., 2009; Meadowcroft, Connor, Smith, & Yang, 2009). Brain magnetic susceptibility studies involving quantitative susceptibility mapping have shown deep grey matter susceptibility differences in multiple sclerosis (Al-Radaideh et al., 2013, {Langkammer, 2013 #10), (Rudko, Solovey, Gati, Kremenchutzky, & Menon, 2014), and changes were also observed longitudinally over two years (Hagemeier et al., 2018). These studies further support that tissues changes cause susceptibility differences and could potentially influence longitudinal association of MR intensity changes with amyloid.

For across subject amyloid status prediction, the combination of T1-weighted, T2-weighted modality and SWI modality was most predictive. This could be because the summary

subject-features were most correlated with these modalities. The subject-level MR features like WMH and hippocampal volume are obtained from T1-weighted and T2-weighted FLAIR. Combining T2-weighted and SWI modalities with T1-weighted modality, the rank-correlation between the original and predicted mean amyloid deposition increased. The voxel-wise PiB prediction using both MR and summary subject-level features was significantly higher than using only summary subject-level measures. This suggests there is information in MR signal at the voxel-level that is associated with amyloid accumulation, which drives the prediction of amyloid.

Our key contribution in this work is to test whether there is a voxel-level association between MRI and amyloid and show how this can be leveraged for amyloid prediction. Previous studies have explored the use of machine learning for cerebral amyloid prediction. Catell et al. (2016) used 3D gradient changes in amyloid imaging to classify amyloid status, their approach improving the detection of amyloid status from the PET images. A limited number of prior studies have used MR imaging to predict amyloid positivity. Ten et al. (2018) used a combination of features as predictors for amyloid status prediction (Ten Kate et al., 2018). They used subject demographics, cognitive variables, regional estimates of volume and cortical thickness from MRI, and *APOE* ε4 information along with machine learning classifier called support vector machine (SVM) with nested 10-fold cross-validation to identify the best discriminating features between amyloid positive and amyloid negative groups. In our study however, we did not use any cognitive measures since we are focused on preclinical phase biomarkers and all the subjects are cognitively normal. To our knowledge, this is the first study that explores the use of MR imaging voxel-level features to predict amyloid imaging voxel-wise in additional to binary output (amyloid positive or amyloid negative) for cognitively normal subjects.

The current results are on a relatively small sample size. Nevertheless, are significant with appropriate cross-validation, thus the results suggest the voxel-level MR features can predict regional amyloid. We suspect with more modalities, more features, including asymmetry filters, and a larger set of images the learning would be much better. Deep learning approaches, such as convolution neural networks on large data sets are a promising future direction. This result demonstrates how voxel-level imaging data can be leveraged for prediction across individuals, and across time.

6.0 A NON-LINEAR REGISTRATION METHOD FOR CO-REGISTRATION OF WHITE MATTER LESIONS DEFINED USING IN-VIVO WHOLE-BRAIN MRI WITH POST-MORTEM BRAIN MRI AND POST-MORTEM PHOTOGRAPHS

White matter hyperintensities (WMH) are commonly found on brain magnetic resonance imaging (MRI) in older subjects and in patients with stroke and dementia. In older adults, the hyperintense signal is often found in the cerebral white matter on T2-weighted MRI. These white matter lesions (WMLs) are found to be clinically associated with cognitive, mood, and functional disturbances. Moreover, these lesions are believed to have heterogenous etiology, including neurodegenerative, inflammatory and ischemic components. The alignment from in-vivo to post-mortem MRIs is essential for improved understanding of the histopathology of WMLs detectable by MRI in-vivo. However, it is a difficult challenge to align post-mortem tissue to the corresponding anatomical location detected ante-mortem due to tissue deformation at post-mortem. In the current study, we address this challenge by developing a non-linear alignment method using post-mortem brain MRI as an intermediate to register in-vivo MRI to histopathology.

6.1 INTRODUCTION

White matter lesions are considered a normal part of the aging brain but their prevalence also has clinical significance in patients with Alzheimer's (Gordon et al., 2015; Kandel et al., 2016; Scheltens et al., 1992) or vascular dementia (Breteler et al., 1994; Gootjes et al., 2004; Smith et al., 2016), multiple sclerosis (Hosseini et al., 2018), and stroke (Baik et al., 2017; Wen

& Sachdev, 2004). These lesions can be visualized as hyperintensities in white matter using T2-weighted fluid attenuated inversion recovery (FLAIR) magnetic resonance imaging sequence. WMH are associated with either being from an ischemic or demyelination origin. Classifying and understanding the lesion etiology is important for appropriate disease treatment (Leite, Rittner, Appenzeller, Ruocco, & Lotufo, 2015 Ruocco, & Lotufo, 2015). Pathological analysis reveals information about the lesions and, by correlating with in-vivo imaging. We can also further understand any imaging-detectable pathology by pathological analysis.

WMHs on MRIs have the potential to aid the neuropathological post mortem assessment of vascular disease in white matter. Post-mortem MR imaging is advantageous since there are no motion or physiological artifacts and there is less time constraint in the MR sequences, being possible to acquire images at higher resolutions when compared to in-vivo regular acquisitions. The correlation of changes observed in-vivo with post-mortem tissue can help to understand the lesion etiology (Leite et al., 2015). Previous studies that reported correlations of WMH between in-vivo and post-mortem histology analysis, relied on manual registration and correlation of post-mortem tissue sections using MRI and after histology analysis (Blezer, Bauer, Brok, Nicolay, & t Hart, 2007 Nicolay, & t Hart, 2007; Fernando et al., 2004; Fisher et al., 2007; Manners et al., 2009; Schmierer et al., 2003; Zhang et al., 2013). Registration of in-vivo MRI with post-mortem imaging is difficult due to limitations in sampling, fixation, and the significant deformations undergone by the brain tissue during dissection. The use of automated registration has been performed for comparison of in vivo and post-mortem total brain volumetric measurements for rat models (Oguz et al., 2013). There is limited research focused on co-registration of human white matter lesions seen on in-vivo MRI with the corresponding

postmortem MRI and digital photographs of the tissue slab (Black, Gao, & Bilbao, 2009 2009; Hornberger et al., 2012).

Post-mortem MRI has been used as an intermediate step for guiding pathological examination (Absinta et al., 2014). In this study we propose a novel method using intermediate ex-vivo brain MRI for accurate registration of in-vivo MRI and photographs of postmortem tissue slabs before histological analysis. The ex-vivo MRI accounts for the time lapse since the in-vivo MRI and contains the same structural distortions as the postmortem tissue slab, while being presented in the same MR space as the in-vivo MRI. We aim to produce an automated registration process that will improve the alignment between pre- and post-mortem imaging and aid in structural-pathological correlation.

6.2 METHODS

6.2.1 Study and Participants

This study was part of an ongoing longitudinal study (P01 AG025204 and R01 MH111265) at the University of Pittsburgh. Brains from participants in this study who received an in vivo MRI and provided consent for brain autopsy were used for postmortem MRI (N=4). The left hemisphere was fixed in 4% paraformaldehyde for three weeks prior to scanning while the right-hemisphere was micro dissected and frozen at -80 degrees Celsius. Age at the in-vivo scan was 70 (20.9) years (Mean (SD)) and age at death was 75(18) years (Mean (SD)). The time between in vivo MRI and death varied 55.62 (40.22) months (Mean (SD)).   Gender representation among the participants was equal (male (50%) and female (50%)).

6.2.2 Image Acquisition

Participants were imaged in-vivo using 3T MR scanner (Siemens MAGNETOM TRIO, Germany). An axial, whole brain (3D) MPRAGE was collected with echo time (TE)=2.98ms, repetition time (TR)=2300ms, flip angle (FA)=9, inversion time (TI) = 900ms, field of view (FOV)=256x240, 1.2x1.0x1.0 mm^3, and 160 slices. An axial, whole brain (2D) FLAIR was collected with TE=90ms, TR=9160ms, FA=150, TI=2500ms, FOV=256x212, 1x1x3 mm^3 resolution, and 48 slices. Post-mortem left hemisphere was scanned using the 7T human MRI scanner (Siemens MAGNETOM, Germany) and a 16-channel transmit radiofrequency coil based on the Tic-Tac-Toe design (Junghwan Kim et al., 2016; Junghwan Kim et al., 2017; Krishnamurthy et al., 2019; Santini, Kim, et al., 2018; Santini, Zhao, et al., 2018) with a 32-channel receive radiofrequency coil. The MPRAGE sequence was acquired with the following parameters: TI = 900ms, TR = 4500 ms, TE = 3.65 ms, and 256 slices. Slice thickness = 0.35mm, flip angle = 8 degrees, voxel size = 0.3x0.3x0.3 mm^3. The post-mortem brain fixed in 4% paraformaldehyde (PFA) was vacuum-sealed inside a plastic bag containing 4% PFA for scanning.

6.2.3 Image Pre-processing

Image pre-processing steps includes segmentation of voxels into tissue probability maps (gray matter, white matter, cerebrospinal fluid), obtaining deformation fields for normalization to Montreal Neurological Institute (MNI) template space, WMHs segmentation and removal of plastic bag from the post-mortem MRI.

6.2.3.1 In-vivo MRI segmentation and skull-stripping

The T1-weighted images were segmented into gray matter (GM), white matter (WM), cerebrospinal fluid (CSF), skull, soft-tissue, and air (outputs a probability map for each class) using SPM12 (Friston et al., 1994). The GM, WM, and CSF were threshold at a probability of 0.1, and added to create an initial intracranial volume mask, which was then refined using an image filling algorithm as well as an image-closing (disk structuring element of 1 voxel) algorithm in MATLAB (Thompson & Shure, 1995)(Soille, 2013). This ICV mask was applied to the in-vivo T1-weighted imaging for obtaining a skull-stripped image. SPM12 segmentation also provides the forward and inverse deformation fields into the standard brain space derived by the MNI template space (Friston et al., 1994).

6.2.3.2 In-vivo white-matter hyperintensity segmentation

We used the method described in (Minjie Wu et al., 2006) for the WMHs segmentation using T2-weighted FLAIR. The segmentation method includes a fuzzy seed based segmentation that identifies hyperintensities in the T2-weighted FLAIR image that corresponds to WMLs (Debette & Markus, 2010; Gorelick et al., 2011). This is an automated segmentation method, which is an iterative algorithm that involves an automated selection of "seeds" of possible WMH lesions and identifies the fuzzy connectedness, which clusters voxels based on their adjacency and affinity, to segment WMH lesions around the seeds. The fully automated WMH segmentation system was implemented in C++ and ITK (Jenkinson, Beckmann, Behrens, Woolrich, & Smith, 2012; H. J. Johnson, McCormick, & Ibanez, 2015; Yushkevich et al., 2006).

6.2.3.3 Post-mortem MR pre-processing

Using FSL BET (Jenkinson et al., 2012), a command designed for brain extraction, the post-mortem MRI signal was stripped from the plastic bag. The left-hemisphere post-mortem MRI was mirrored to create a whole brain MRI in order for applying SPM12 segmentation and normalization methods since it uses a whole brain template. The whole-brain MRI was segmented into GM, WM, and CSF, to obtain the forward and inverse deformation fields into the MNI template space.

6.2.4 Image Registration

6.2.4.1 Overview of registration process

Image co-registration of the in-vivo MRI and the post-mortem digital photographs used a combination of linear and nonlinear registration methods (Figure 17 shows the steps in detail). The steps involve alignment of post-mortem MRI (left hemisphere) to in-vivo MRI (left hemisphere) (steps 1-2), mirroring the left hemisphere to create a whole brain (step 3), normalization in-vivo and post-mortem MRI to MNI template (step 4), co-registration of in-vivo and post-mortem MRI (steps 5-6). The steps 4-6 are repeated for in-vivo T2-weighted FLAIR, along with the corresponding WMHs segmentation image (step 7). The post-mortem MRI axial slice is registered in a semi-automated approach using landmark based or control-point registration (steps 8-9).

6.2.4.2 Registration of In-vivo to Post-mortem MRI

A nonlinear registration method using SPM12 was used to register the T1-weighted in-vivo MR image to the T1-weighted post-mortem MR image, as it is more successful than linear registration methods in aligning structures that are significantly deformed. Normalization warps images to fit a standard template to co-register images that are fundamentally different in shape. The non-linear deformation was obtained from unified segmentation and normalization described in 3.4.2.1 (J. Ashburner & Friston, 1999).

The in-vivo and post-mortem MR images were normalized to the MNI space, a template created by nonlinear registration of 152 T1- weighted images, using their respective forward deformation fields. The post-mortem inverse deformation field was then applied to the normalized in-vivo and post-mortem image to co-register them. The deformation fields were applied using a resolution of 0.5x0.5x0.5 mm^3 and the bounding boxes were adjusted for better overlap. To achieve accurate registration, an additional normalization method was repeated or an additional linear co-registration step was included. The additional registration step used a rigid-body model based off the work by Collignon et al (Collignon et al., 1995). Similarly, in-vivo T2-weighted FLAIR and WMH segmentation obtained from T2-weighted FLAIR were co-registered to the post-mortem MR image.

6.2.4.3 Registration of Post-mortem MRI to Post-mortem Digital Photographs

Color digital photographs of post-mortem brain sections were resized and converted to gray-scale. They were matched manually to the axial section of co-registered left-hemisphere post-mortem MRI. The digital photograph and the corresponding MRI slice were registered using control point registration in MATLAB by selecting corresponding landmarks (vertices of the ventricles and significant ridges on the perimeter) on the moving image (the digital

photograph) and the fixed image (the MRI axial slice). The corresponding landmarks were used to generate the transform between the moving and the fixed image and were applied on all the axial slices from registered post-mortem MRI (T1-weighted) and in-vivo MRI (T1-weighted, T2-weighted FLAIR, WMHs segmentations). The final WMHs segmentation from in-vivo MR overlaid on the post-mortem photograph can be used for histological analysis.
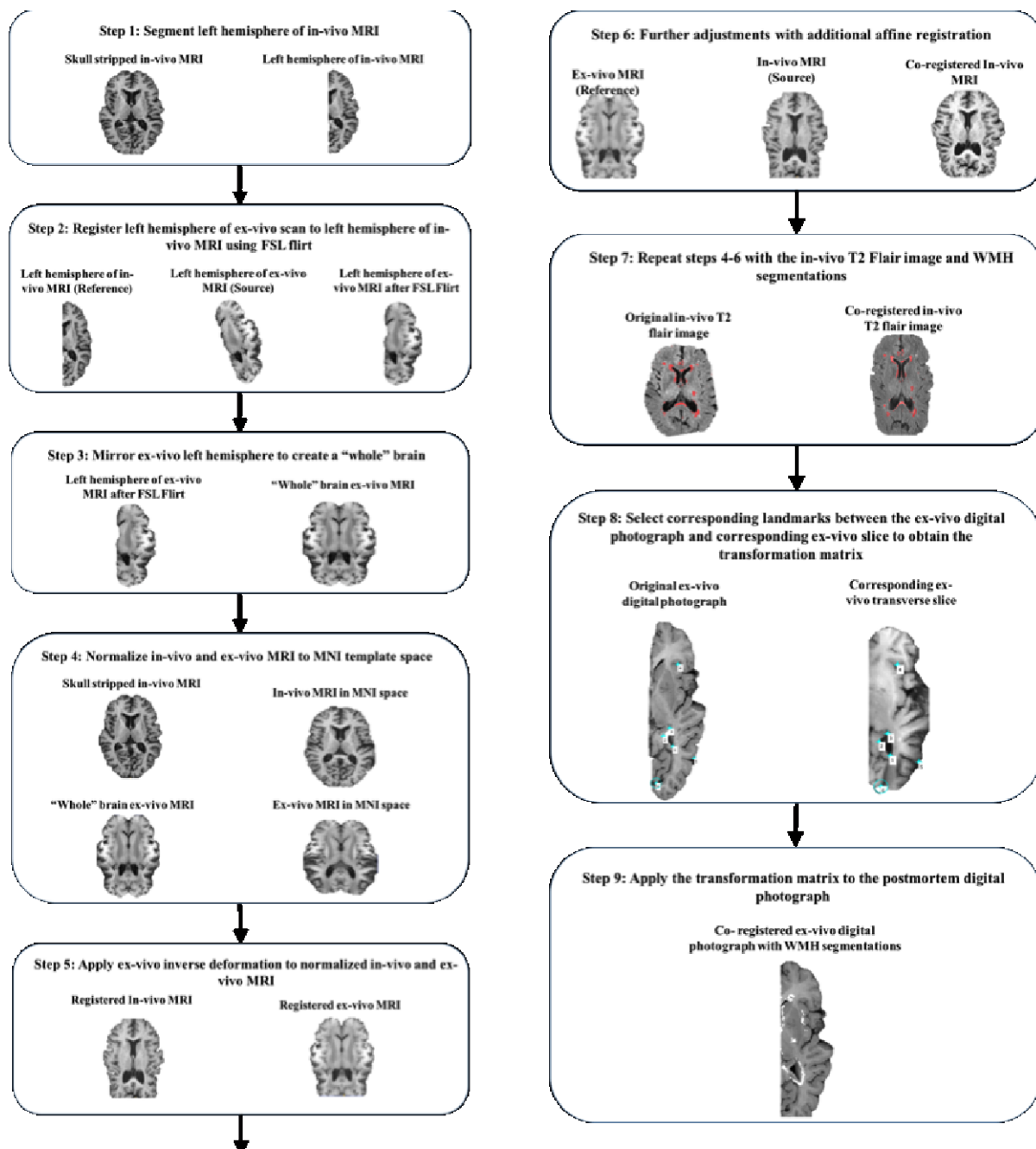
Figure 17 Schematic of registration method

6.3 RESULTS

Each of the post-mortem MRIs differed in ventricle size, atrophy, and degree of deformation during scanning. Figures 18-21 show left hemisphere co-registered images in the following order; in-vivo T1-weighted MRI (A), in-vivo T2- weighted FLAIR image (B), post-mortem T1-weighted MRI (C), in-vivo T1-weighted MRI overlaid onto post-mortem T1-weighted MRI (D), T2-FLAIR overlaid onto T1-weighted post-mortem MRI (E), and WMHs segmentations overlaid onto T1-weighted post-mortem MRI (F), onto T2-weighted in-vivo MRI (G), and onto post-mortem digital photograph (H). The described method yielded best registration for subject 1 (figure 18) and subject 3 (figure 20). Portions of post-mortem gray matter in the MR image were stripped during the process of removing the plastic bag (figure 18C). Although we adjusted the bounding box there were portions that were cut during the registration process. For subject 2 (figure 19), the co-registration improved after an additional step of normalization and control point registration to align the gyrus folds. The WMHs observed in T2-weighted FLAIR on the left hemisphere were very limited for subject 3. Subject 4 (figure 21) however did not have a perfect alignment with the WMH since the ventricles did not overlap perfectly.

Figure 18 Coregistered images for Subject 1

Left hemisphere of A. T1-weighted in-vivo MRI B. T2-weighted (FLAIR) in-vivo MRI C. T1-weighted post-mortem MRI D. In-vivo MRI overlaid onto post-mortem MRI E. FLAIR image overlaid onto post-mortem MRI F. WMHs Segmentations overlaid on T1-weighted post-mortem MRI G. Segmented WMHs overlaid on T2-weighted in-vivo

Figure 19 Coregistered images for Subject 2

Left hemisphere of A. T1-weighted in-vivo MRI B. T2-weighted (FLAIR) in-vivo MRI C. T1-weighted post-mortem MRI D. In-vivo MRI overlaid onto post-mortem MRI E. FLAIR image overlaid onto post-mortem MRI F. WMHs Segmentations overlaid on T1-weighted post-mortem MRI G. Segmented WMHs overlaid on T2-weighted in-vivo

Figure 20 Coregistered images for Subject 3

Left hemisphere of A. T1-weighted in-vivo MRI B. T2-weighted (FLAIR) in-vivo MRI C. T1-weighted

post-mortem MRI D. In-vivo MRI overlaid onto post-mortem MRI E. FLAIR image overlaid onto post-

mortem MRI F. WMHs Segmentations overlaid on T1-weighted post-mortem MRI G. Segmented WMHs

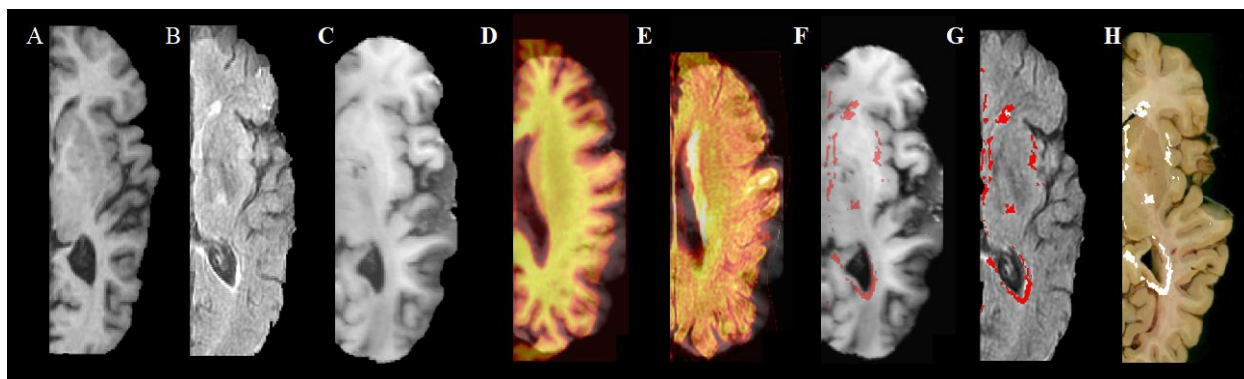overlaid on T2-weighted in-vivo

Figure 21 Coregistered images for Subject 4

Left hemisphere of A. T1-weighted in-vivo MRI B. T2-weighted (FLAIR) in-vivo MRI C. T1-weighted

post-mortem MRI D. In-vivo MRI overlaid onto post-mortem MRI E. FLAIR image overlaid onto post-

mortem MRI F. WMHs Segmentations overlaid on T1-weighted post-mortem MRI G. Segmented WMHs
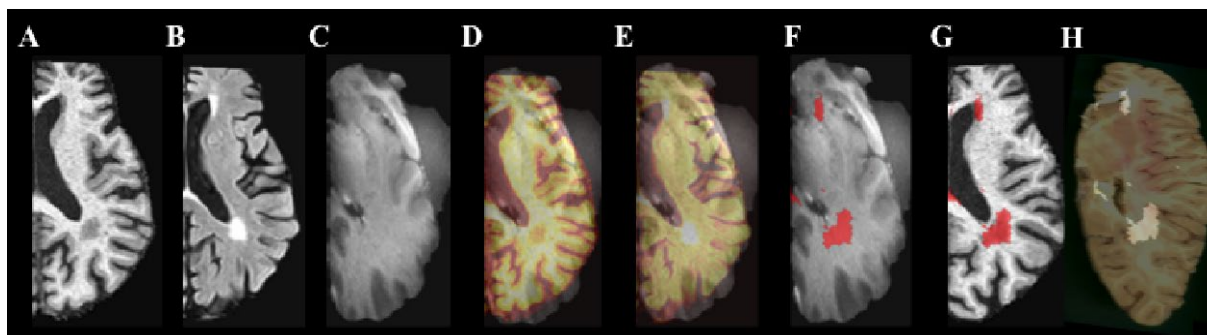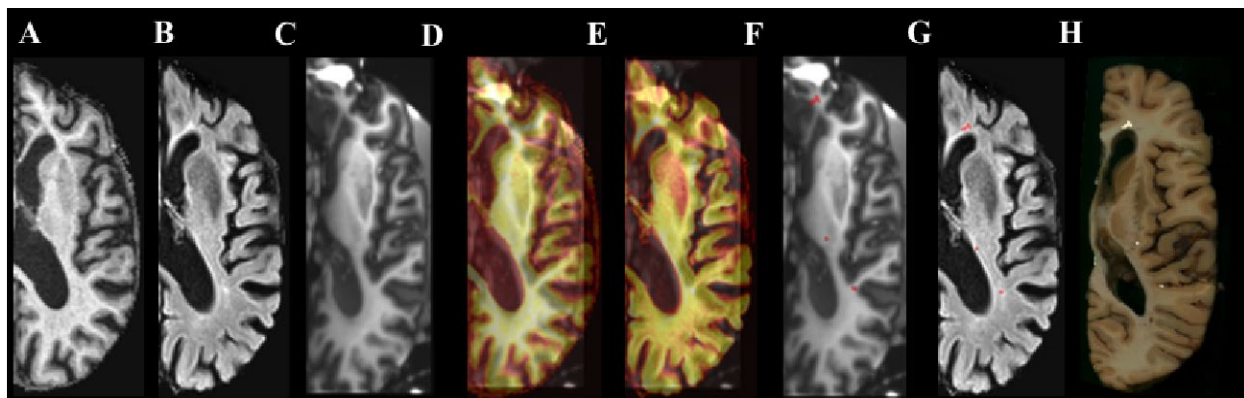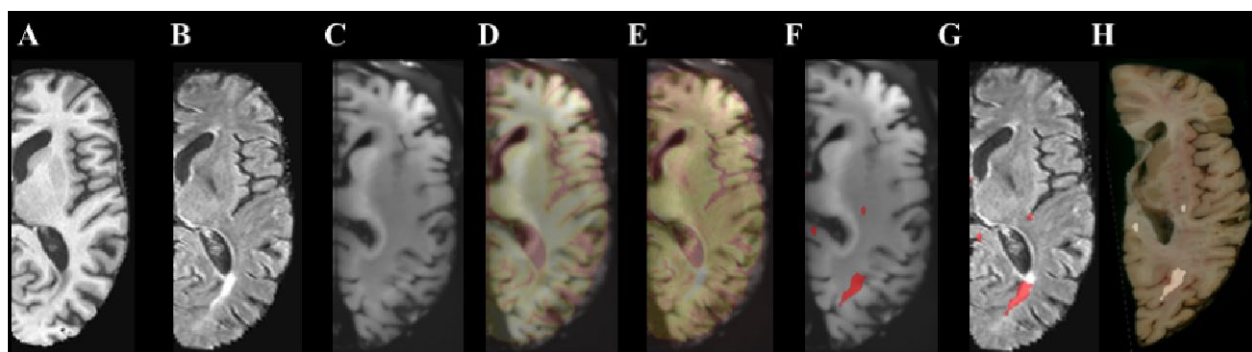
overlaid on T2-weighted in-vivo

6.4 DISCUSSIONS

A nonlinear registration method was developed in order to align pathology detected with an in-vivo MRI with the corresponding postmortem tissue slab by using an ex-vivo MRI as an intermediate. This method allows correlation of in-vivo changes with precise areas of the postmortem tissue slab, which provides guidance for postmortem histological evaluation of the in vivo changes. Our method utilizes an ex-vivo MRI as an intermediate step to guide the localization of in-vivo white matter lesions on the postmortem tissue slab. The ability to place the WMH segmentations from the in-vivo FLAIR image directly on the ex-vivo MRI and then the digital photograph of the hemisphere, allows individual lesions to be identified and studied.

Few studies have co-registered in vivo human brain MRI to histology using whole hemispheres, with most focusing on specific regions of the brain. Goubran et al. (2015) reported registering an ex-vivo scan of the anterior portion of the temporal lobe to in-vivo MRI scans using an automated initialization as well as a landmark- based rigid registration, followed by a deformable landmark registration. Their work is limited in region and by the fragmented tissue resulting from the temporal lobectomy (Goubran et al., 2015). There have been few publications describing algorithms for aligning in-vivo to ex-vivo brain MRIs that would address WMH localization for our post-mortem tissue processing protocol. Kim et al. registered postmortem human brain histology images to an in vivo MRI reference volume using non-linear polynomial transformations (T.-S. Kim, Singh, Sungkarat, Zarow, & Chui, 2000). A polynomial model allows for the compensation of global distortions between the pre- and post-mortem images but does not take local deformations into account. Our method combines a 3D- to- 3D registration between the in-vivo and ex-vivo MRIs with a 2D- to- 2D registration between the ex-vivo

photograph and a manually selected matching MRI slice, creating a successful alignment of WMHs across all modalities to serve as a guide to histology. However, for subjects when the ventricle shrinkage occurred the alignment near the ventricles between the in-vivo and postmortem tissue was not perfect (figures 11 and 13). We had to perform additional steps of control-point registration to correct but it was still not perfectly aligned to each other.

The present study had limitations preventing the development of a completely automated registration method. The postmortem brain undergoes natural tissue deformation upon brain removal and fixation. These external factors caused difficulty for registration of the postmortem tissue slab with the anatomical structures seen in-vivo. Since the tissue deformation of each subject was different, we needed to take a partially custom approach to each subject by adding some additional steps for better alignment between the in vivo MRI and digital photograph of the postmortem slab. There was variability in the placement of post-mortem MRI in the MR scanner, across subjects. Sometimes it was hard to distinguish between the coronal, sagittal and transverse planes. This variability had to be accounted for, by additional pre-processing steps that were different for each subject. This limitation may be resolved by 3D printing a skull model that can help fixate the brain similar to how in-vivo brain, making it more consistent across each subject. The plastic bag was a hindrance in the registration, as it created inhomogeneities in the overall intensities across the image and cut brain when removed. Neuropathology studies of post-mortem brains can provide information on the etiology and pathogenesis of the WM lesions and help to understand the image visualized on in-vivo MRI. Structural changes in WM integrity are regularly observed through MRI and can reveal the dynamic nature of WMHs as well as their interactions with other pathological features and contribution to overall brain damage. Combining the information obtained by MRI with the information from the post-mortem

pathology studies will not only assist in the understanding of the underlying mechanisms seen on the MRI, but also help improve the imaging-to-autopsy validation studies of PET radioligands and lead to more accurate diagnosis and development of better treatment plans.

Postmortem neuropathological studies can provide information on the etiology and pathophysiology of the white matter lesions and can help to understand abnormalities visualized on in-vivo MRI. Structural changes in white matter integrity are regularly observed with MRI and can reveal the dynamic nature of WMH as well as their interactions with other pathological features and contributions to overall brain damage. Combining the information obtained by MRI with the information from the postmortem pathological studies will not only assist in the understanding of the underlying abnormalities seen on the MRI, but could also help develop a deeper understanding of the etiology of these abnormalities. This understanding could ultimately lead to improvements in therapy aimed at preventing or treating these abnormalities.

7.0 CONCLUSIONS AND FUTURE WORK

7.1 SUMMARY CONCLUSIONS

This thesis represents novel contribution on the use of MRI for co-registration of whole brain MRI with the photographs through means of post-mortem whole hemisphere as an intermediate guide to registration. The other study on amyloid prediction is our major contribution and forms the basis for specific aims in this dissertation work. It also represents first work on prediction of voxel-level amyloid deposition in the brain using MRI and machine learning, which takes on a novel two level-approach on voxel-level and subject-level. Although the techniques used as established and widely used machine-learning techniques the combination and method employed is novel in the prediction of voxel-level amyloid. We have addressed the specific aims as follows.

In Aim 1, within subject analysis has been utilized for amyloid change prediction. MR signal from T2-weighted and susceptibility weighted imaging modalities have been shown to preform the best. It aids in the fact that these are useful for longitudinal studies and can be very useful in longitudinal monitoring of amyloid and utility as a possible screening tool. When there is more MRI data time points for an individual their corresponding PET (PiB) image can be predicted. Identifying these imaging biomarkers is helpful in studies especially longitudinal monitoring of patients and can pave way for better diagnostic tools.

In Aim 2, generalization helps in amyloid voxel-level prediction and also status classification. The use of T1-weighted, T2-weighted FLAIR and susceptibility weighted imaging can increase the prediction and also the correlation with the original PiB. This is indicative of the combination of features can aid in the prediction ad also provides an insight into how each of the modality combinations are associated with amyloid in the brain.

7.2 FUTURE WORK

In the first study the protocol design of photographs and post-mortem imaging of hemisphere. The MRI was not designed for Post-mortem brain characteristics of no skull. The photographs have to be taken at the same camera configuration. The hemisphere using 3D model of skull or fixation for the brain tissue will help to maintain a fixed position of the brain for consistent on the orientation. Using agarose gel instead of plastic bag will help in the issue with interference in the technique due to the presence of the plastic bag.

The present work confirms the MR signal is related to amyloid deposition and is useful in the prediction of amyloid. Future work in the prediction of voxel-level amyloid will involve a larger cohort or combination of cohort. Deep learning methods have shown promise in identifying features that are similar to textural features used. Deep learning also is more efficient with larger data. Convolution neural network is a type of neural network that uses several layers convolution filters. The outcome of each layer of convolution filter can help in identifying the landmarks and features that might help in better prediction of amyloid. It can be used for both feature extraction tool and for prediction. Also recurrent neural networks can make use of longitudinal data for prediction.

7.3 FUNDING SUPPORT

BIBLIOGRAPHY

Abbasian Ardakani, A., Gharbali, A., Saniei, Y., Mosarrezaii, A., & Nazarbaghi, S. (2015). Application of Texture Analysis in Diagnosis of Multiple Sclerosis by Magnetic Resonance Imaging. *Glob J Health Sci, 7*(6), 68-78. doi:10.5539/gjhs.v7n6p68

Absinta, M., Nair, G., Filippi, M., Ray-Chaudhury, A., Reyes-Mantilla, M. I., Pardo, C. A., & Reich, D. S. (2014). Postmortem magnetic resonance imaging to guide the pathologic cut: individualized, 3-dimensionally printed cutting boxes for fixed brains. *J Neuropathol Exp Neurol, 73*(8), 780-788. doi:10.1097/NEN.0000000000000096

Adams, R., & Bischof, L. (1994). Seeded region growing. *IEEE transactions on pattern analysis and machine intelligence, 16*(6), 641-647.

Adlard, P. A., Tran, B. A., Finkelstein, D. I., Desmond, P. M., Johnston, L. A., Bush, A. I., & Egan, G. F. (2014). A review of beta-amyloid neuroimaging in Alzheimer's disease. *Front Neurosci, 8*, 327. doi:10.3389/fnins.2014.00327

Aizenstein, H. J., Nebes, R. D., Saxton, J. A., Price, J. C., Mathis, C. A., Tsopelas, N. D., . . . Klunk, W. E. (2008). Frequent amyloid deposition without significant cognitive impairment among the elderly. *Arch Neurol, 65*(11), 1509-1517. doi:10.1001/archneur.65.11.1509

Al-Radaideh, A. M., Wharton, S. J., Lim, S. Y., Tench, C. R., Morgan, P. S., Bowtell, R. W., . . . Gowland, P. A. (2013). Increased iron accumulation occurs in the earliest stages of demyelinating disease: an ultra-high field susceptibility mapping study in Clinically Isolated Syndrome. *Mult Scler, 19*(7), 896-903. doi:10.1177/1352458512465135

Alsabti, K., Ranka, S., & Singh, V. (1997). An efficient k-means clustering algorithm.

Alzheimer's, A. (2016). 2016 Alzheimer's disease facts and figures. *Alzheimers Dement, 12*(4), 459-509.

Ashburner, J. VBM tutorial.

Ashburner, J., & Friston, K. J. (1999). Nonlinear spatial normalization using basis functions. *Hum Brain Mapp, 7*(4), 254-266.

Ashburner, J., & Friston, K. J. (2005). Unified segmentation. *Neuroimage, 26*(3), 839-851.

Bahadure, N. B., Ray, A. K., & Thethi, H. P. (2017). Image Analysis for MRI Based Brain Tumor Detection and Feature Extraction Using Biologically Inspired BWT and SVM. *Int J Biomed Imaging, 2017*, 9749108. doi:10.1155/2017/9749108

Baik, M., Kim, K., Yoo, J., Kim, H. C., Jeong, S. H., Kim, K. H., . . . Nam, H. S. (2017). Differential impact of white matter hyperintensities on long-term outcomes in ischemic stroke patients with large artery atherosclerosis. *PLoS One, 12*(12), e0189611. doi:10.1371/journal.pone.0189611

Beheshti, I., Demirel, H., Matsuda, H., & Alzheimer's Disease Neuroimaging, I. (2017). Classification of Alzheimer's disease and prediction of mild cognitive impairment-to-Alzheimer's conversion from structural magnetic resource imaging using feature ranking and a genetic algorithm. *Comput Biol Med, 83*, 109-119. doi:10.1016/j.compbiomed.2017.02.011

Bishop, C. M. (2006). *Pattern Recognition and Machine Learning (Information Science and Statistics)*: Springer-Verlag.

Black, S., Gao, F., & Bilbao, J. (2009). Understanding white matter disease: imaging-pathological correlations in vascular cognitive impairment. *Stroke, 40*(3 Suppl), S48-52. doi:10.1161/STROKEAHA.108.537704

Blezer, E. L., Bauer, J., Brok, H. P., Nicolay, K., & t Hart, B. A. (2007). Quantitative MRI-pathology correlations of brain white matter lesions developing in a non-human primate model of multiple sclerosis. *NMR Biomed, 20*(2), 90-103. doi:10.1002/nbm.1085

Bozzali, M., Serra, L., & Cercignani, M. (2016). Quantitative MRI to understand Alzheimer's disease pathophysiology. *Curr Opin Neurol, 29*(4), 437-444. doi:10.1097/WCO.0000000000000345

Breteler, M. M., van Swieten, J. C., Bots, M. L., Grobbee, D. E., Claus, J. J., van den Hout, J. H., . . . et al. (1994). Cerebral white matter lesions, vascular risk factors, and cognitive function in a population-based study: the Rotterdam Study. *Neurology, 44*(7), 1246-1252.

Brickman, A. M., Muraskin, J., & Zimmerman, M. E. (2009). Structural neuroimaging in Altheimer's disease: do white matter hyperintensities matter? *Dialogues Clin Neurosci, 11*(2), 181-190.

Brickman, A. M., Small, S. A., & Fleisher, A. (2009). Pinpointing synaptic loss caused by Alzheimer's disease with fMRI. *Behav Neurol, 21*(1), 93-100. doi:10.3233/BEN-2009-0240

Brix, G., Zaers, J., Adam, L. E., Bellemann, M. E., Ostertag, H., Trojan, H., . . . Lorenz, W. J. (1997). Performance evaluation of a whole-body PET scanner using the NEMA protocol. National Electrical Manufacturers Association. *J Nucl Med, 38*(10), 1614-1623.

Bruscoli, M., & Lovestone, S. (2004). Is MCI really just early dementia? A systematic review of conversion studies. *Int Psychogeriatr, 16*(2), 129-140.

Carpenter, A. P., Jr., Pontecorvo, M. J., Hefti, F. F., & Skovronsky, D. M. (2009). The use of the exploratory IND in the evaluation and development of 18F-PET radiopharmaceuticals for

amyloid imaging in the brain: a review of one company's experience. *Q J Nucl Med Mol Imaging, 53*(4), 387-393.

Cattell, L., Platsch, G., Pfeiffer, R., Declerck, J., Schnabel, J. A., Hutton, C., & Alzheimer's Disease Neuroimaging, I. (2016). Classification of amyloid status using machine learning with histograms of oriented 3D gradients. *Neuroimage Clin, 12*, 990-1003. doi:10.1016/j.nicl.2016.05.004

Chamberlain, R., Reyes, D., Curran, G. L., Marjanska, M., Wengenack, T. M., Poduslo, J. F., . . . Jack, C. R., Jr. (2009). Comparison of amyloid plaque contrast generated by T2-weighted, T2*-weighted, and susceptibility-weighted imaging methods in transgenic mouse models of Alzheimer's disease. *Magn Reson Med, 61*(5), 1158-1164. doi:10.1002/mrm.21951

Chandra, A., Dervenoulas, G., Politis, M., & Alzheimer's Disease Neuroimaging, I. (2018). Magnetic resonance imaging in Alzheimer's disease and mild cognitive impairment. *J Neurol*. doi:10.1007/s00415-018-9016-3

Chapelle, O., Scholkopf, B., & Zien, A. (2009). Semi-supervised learning (chapelle, o. et al., eds.; 2006)[book reviews]. *IEEE Transactions on Neural Networks, 20*(3), 542-542.

Chapman, R. M., Mapstone, M., McCrary, J. W., Gardner, M. N., Porsteinsson, A., Sandoval, T. C., . . . Reilly, L. A. (2011). Predicting conversion from mild cognitive impairment to Alzheimer's disease using neuropsychological tests and multivariate methods. *J Clin Exp Neuropsychol, 33*(2), 187-199. doi:10.1080/13803395.2010.499356

Cohen, A. D., & Klunk, W. E. (2014). Early detection of Alzheimer's disease using PiB and FDG PET. *Neurobiol Dis, 72 Pt A*, 117-122. doi:10.1016/j.nbd.2014.05.001

Cohen, A. D., Mowrey, W., Weissfeld, L. A., Aizenstein, H. J., McDade, E., Mountz, J. M., . . . Klunk, W. E. (2013). Classification of amyloid-positivity in controls: comparison of visual read and quantitative approaches. *Neuroimage, 71*, 207-215. doi:10.1016/j.neuroimage.2013.01.015

Cohen, A. D., Price, J. C., Weissfeld, L. A., James, J., Rosario, B. L., Bi, W., . . . Klunk, W. E. (2009). Basal cerebral metabolism may modulate the cognitive effects of Abeta in mild cognitive impairment: an example of brain reserve. *J Neurosci, 29*(47), 14770-14778. doi:10.1523/JNEUROSCI.3669-09.2009

Collignon, A., Maes, F., Delaere, D., Vandermeulen, D., Suetens, P., & Marchal, G. (1995). *Automated multi-modality image registration based on information theory.* Paper presented at the Information processing in medical imaging.

Dawood, M., Jiang, X., & Schäfers, K. (2012). *Correction Techniques in Emission Tomography*: CRC Press.

De Jong, S. (1993). SIMPLS: an alternative approach to partial least squares regression. *Chemometrics and intelligent laboratory systems, 18*(3), 251-263.

de Oliveira, M. S., Betting, L. E., Mory, S. B., Cendes, F., & Castellano, G. (2013). Texture analysis of magnetic resonance images of patients with juvenile myoclonic epilepsy. *Epilepsy Behav, 27*(1), 22-28. doi:10.1016/j.yebeh.2012.12.009

Debette, S., & Markus, H. S. (2010). The clinical importance of white matter hyperintensities on brain magnetic resonance imaging: systematic review and meta-analysis. *BMJ, 341*, c3666. doi:10.1136/bmj.c3666

Dehmelt, L., & Halpain, S. (2005). The MAP2/Tau family of microtubule-associated proteins. *Genome Biol, 6*(1), 204. doi:10.1186/gb-2004-6-1-204

Di Ieva, A., Lam, T., Alcaide-Leon, P., Bharatha, A., Montanera, W., & Cusimano, M. D. (2015). Magnetic resonance susceptibility weighted imaging in neurosurgery: current applications and future perspectives. *J Neurosurg, 123*(6), 1463-1475. doi:10.3171/2015.1.JNS142349

Fan, Y., Resnick, S. M., Wu, X., & Davatzikos, C. (2008). Structural and functional biomarkers of prodromal Alzheimer's disease: a high-dimensional pattern classification study. *Neuroimage, 41*(2), 277-285. doi:10.1016/j.neuroimage.2008.02.043

Farias, S. T., Mungas, D., Reed, B. R., Harvey, D., & DeCarli, C. (2009). Progression of mild cognitive impairment to dementia in clinic- vs community-based cohorts. *Arch Neurol, 66*(9), 1151-1157. doi:10.1001/archneurol.2009.106

Felzenszwalb, P. F., & Huttenlocher, D. P. (2004). Efficient graph-based image segmentation. *International journal of computer vision, 59*(2), 167-181.

Fernando, M. S., O'Brien, J. T., Perry, R. H., English, P., Forster, G., McMeekin, W., . . . Neuropathology Group of, M. C. (2004). Comparison of the pathology of cerebral white matter with post-mortem magnetic resonance imaging (MRI) in the elderly brain. *Neuropathol Appl Neurobiol, 30*(4), 385-395. doi:10.1111/j.1365-2990.2004.00550.x

Fisher, E., Chang, A., Fox, R. J., Tkach, J. A., Svarovsky, T., Nakamura, K., . . . Trapp, B. D. (2007). Imaging correlates of axonal swelling in chronic multiple sclerosis brains. *Ann Neurol, 62*(3), 219-228. doi:10.1002/ana.21113

Frisoni, G. B., Fox, N. C., Jack, C. R., Jr., Scheltens, P., & Thompson, P. M. (2010). The clinical use of structural MRI in Alzheimer disease. *Nat Rev Neurol, 6*(2), 67-77. doi:10.1038/nrneurol.2009.215

Frisoni, G. B., Testa, C., Zorzan, A., Sabattoli, F., Beltramello, A., Soininen, H., & Laakso, M. P. (2002). Detection of grey matter loss in mild Alzheimer's disease with voxel based morphometry. *J Neurol Neurosurg Psychiatry, 73*(6), 657-664.

Friston, K. J., Holmes, A. P., Worsley, K. J., Poline, J. P., Frith, C. D., & Frackowiak, R. S. (1994). Statistical parametric maps in functional imaging: a general linear approach. *Human brain mapping, 2*(4), 189-210.

Garali, I., Adel, M., Bourennane, S., & Guedj, E. (2018). Histogram-Based Features Selection and Volume of Interest Ranking for Brain PET Image Classification. *IEEE J Transl Eng Health Med, 6*, 2100212. doi:10.1109/JTEHM.2018.2796600

Gendron, T. F., & Petrucelli, L. (2009). The role of tau in neurodegeneration. *Mol Neurodegener, 4*, 13. doi:10.1186/1750-1326-4-13

Gootjes, L., Teipel, S. J., Zebuhr, Y., Schwarz, R., Leinsinger, G., Scheltens, P., . . . Hampel, H. (2004). Regional distribution of white matter hyperintensities in vascular dementia, Alzheimer's disease and healthy aging. *Dement Geriatr Cogn Disord, 18*(2), 180-188. doi:10.1159/000079199

Gordon, B. A., Najmi, S., Hsu, P., Roe, C. M., Morris, J. C., & Benzinger, T. L. (2015). The effects of white matter hyperintensities and amyloid deposition on Alzheimer dementia. *Neuroimage Clin, 8*, 246-252. doi:10.1016/j.nicl.2015.04.017

Gorelick, P. B., Scuteri, A., Black, S. E., Decarli, C., Greenberg, S. M., Iadecola, C., . . . Anesthesia. (2011). Vascular contributions to cognitive impairment and dementia: a statement for healthcare professionals from the american heart association/american stroke association. *Stroke, 42*(9), 2672-2713. doi:10.1161/STR.0b013e3182299496

Goshtasby, A. (1986). Piecewise linear mapping functions for image registration. *Pattern Recognition, 19*(6), 459-466.

Goubran, M., de Ribaupierre, S., Hammond, R. R., Currie, C., Burneo, J. G., Parrent, A. G., . . . Khan, A. R. (2015). Registration of in-vivo to ex-vivo MRI of surgically resected specimens: a pipeline for histology to in-vivo registration. *J Neurosci Methods, 241*, 53-65. doi:10.1016/j.jneumeth.2014.12.005

Graff-Radford, J., Botha, H., Rabinstein, A. A., Gunter, J. L., Przybelski, S. A., Lesnick, T., . . . Kantarci, K. (2018). Cerebral microbleeds: Prevalence and relationship to amyloid burden. *Neurology*. doi:10.1212/WNL.0000000000006780

Guo, Y., Zhang, Z., Zhou, B., Wang, P., Yao, H., Yuan, M., . . . Liu, Y. (2014). Grey-matter volume as a potential feature for the classification of Alzheimer's disease and mild cognitive impairment: an exploratory study. *Neurosci Bull, 30*(3), 477-489. doi:10.1007/s12264-013-1432-x

Haacke, E. M., Mittal, S., Wu, Z., Neelavalli, J., & Cheng, Y. C. (2009). Susceptibility-weighted imaging: technical aspects and clinical applications, part 1. *AJNR Am J Neuroradiol, 30*(1), 19-30. doi:10.3174/ajnr.A1400

Hagemeier, J., Zivadinov, R., Dwyer, M. G., Polak, P., Bergsland, N., Weinstock-Guttman, B., . . . Schweser, F. (2018). Changes of deep gray matter magnetic susceptibility over 2 years in multiple sclerosis and healthy control brain. *Neuroimage Clin, 18*, 1007-1016. doi:10.1016/j.nicl.2017.04.008

Halefoglu, A. M., & Yousem, D. M. (2018). Susceptibility weighted imaging: Clinical applications and future directions. *World J Radiol, 10*(4), 30-45. doi:10.4329/wjr.v10.i4.30

Harrison, L. C., Raunio, M., Holli, K. K., Luukkaala, T., Savio, S., Elovaara, I., . . . Dastidar, P. (2010). MRI texture analysis in multiple sclerosis: toward a clinical analysis protocol. *Acad Radiol, 17*(6), 696-707. doi:10.1016/j.acra.2010.01.005

Henneman, W. J., Sluimer, J. D., Barnes, J., van der Flier, W. M., Sluimer, I. C., Fox, N. C., . . . Barkhof, F. (2009). Hippocampal atrophy rates in Alzheimer disease: added value over whole brain volume measures. *Neurology, 72*(11), 999-1007. doi:10.1212/01.wnl.0000344568.09360.31

Hilbert, K., Pine, D. S., Muehlhan, M., Lueken, U., Steudte-Schmiedgen, S., & Beesdo-Baum, K. (2015). Gray and white matter volume abnormalities in generalized anxiety disorder by categorical and dimensional characterization. *Psychiatry Res, 234*(3), 314-320. doi:10.1016/j.pscychresns.2015.10.009

Hirata, Y., Matsuda, H., Nemoto, K., Ohnishi, T., Hirao, K., Yamashita, F., . . . Samejima, H. (2005). Voxel-based morphometry to discriminate early Alzheimer's disease from controls. *Neurosci Lett, 382*(3), 269-274. doi:10.1016/j.neulet.2005.03.038

Hornberger, M., Wong, S., Tan, R., Irish, M., Piguet, O., Kril, J., . . . Halliday, G. (2012). In vivo and post-mortem memory circuit integrity in frontotemporal dementia and Alzheimer's disease. *Brain, 135*(Pt 10), 3015-3025. doi:10.1093/brain/aws239

Hosseini, Z., Matusinec, J., Rudko, D. A., Liu, J., Kwan, B. Y. M., Salehi, F., . . . Drangova, M. (2018). Morphology-Specific Discrimination between MS White Matter Lesions and Benign White Matter Hyperintensities Using Ultra-High-Field MRI. *AJNR Am J Neuroradiol, 39*(8), 1473-1479. doi:10.3174/ajnr.A5705

Hsu, C. C., Kwan, G. N. C., Hapugoda, S., Craigie, M., Watkins, T. W., & Haacke, E. M. (2017). Susceptibility weighted imaging in acute cerebral ischemia: review of emerging technical concepts and clinical applications. *Neuroradiol J, 30*(2), 109-119. doi:10.1177/1971400917690166

Hush, D. R., & Horne, B. G. (1993). Progress in supervised neural networks. *IEEE signal processing magazine, 10*(1), 8-39.

Ikonomovic, M. D., Klunk, W. E., Abrahamson, E. E., Mathis, C. A., Price, J. C., Tsopelas, N. D., . . . DeKosky, S. T. (2008). Post-mortem correlates of in vivo PiB-PET amyloid imaging in a typical case of Alzheimer's disease. *Brain, 131*(Pt 6), 1630-1645. doi:10.1093/brain/awn016

Iqbal, K., Liu, F., Gong, C. X., & Grundke-Iqbal, I. (2010). Tau in Alzheimer disease and related tauopathies. *Curr Alzheimer Res, 7*(8), 656-664.

Irvine, G. B., El-Agnaf, O. M., Shankar, G. M., & Walsh, D. M. (2008). Protein aggregation in the brain: the molecular basis for Alzheimer's and Parkinson's diseases. *Mol Med, 14*(7-8), 451-464. doi:10.2119/2007-00100.Irvine

Islam, J., & Zhang, Y. (2017). An Ensemble of Deep Convolutional Neural Networks for Alzheimer's Disease Detection and Classification. *arXiv preprint arXiv:1712.01675*.

Jack, C. R., Jr., Knopman, D. S., Jagust, W. J., Shaw, L. M., Aisen, P. S., Weiner, M. W., . . . Trojanowski, J. Q. (2010). Hypothetical model of dynamic biomarkers of the Alzheimer's pathological cascade. *Lancet Neurol, 9*(1), 119-128. doi:10.1016/S1474-4422(09)70299-6

Jack, C. R., Jr., Knopman, D. S., Weigand, S. D., Wiste, H. J., Vemuri, P., Lowe, V., . . . Petersen, R. C. (2012). An operational approach to National Institute on Aging-Alzheimer's Association criteria for preclinical Alzheimer disease. *Ann Neurol, 71*(6), 765-775. doi:10.1002/ana.22628

Jenkinson, M., Beckmann, C. F., Behrens, T. E., Woolrich, M. W., & Smith, S. M. (2012). Fsl. *Neuroimage, 62*(2), 782-790.

Johnson, H. J., McCormick, M. M., & Ibanez, L. (2015). *The ITK Software Guide Book 1: Introduction and Development Guidelines-Volume 1*: Kitware, Inc.

Johnson, K. A., Fox, N. C., Sperling, R. A., & Klunk, W. E. (2012). Brain imaging in Alzheimer disease. *Cold Spring Harb Perspect Med, 2*(4), a006213. doi:10.1101/cshperspect.a006213

Kambeitz, J., Cabral, C., Sacchet, M. D., Gotlib, I. H., Zahn, R., Serpa, M. H., . . . Koutsouleris, N. (2017). Detecting Neuroimaging Biomarkers for Depression: A Meta-analysis of Multivariate Pattern Recognition Studies. *Biol Psychiatry, 82*(5), 330-338. doi:10.1016/j.biopsych.2016.10.028

Kambeitz, J., Kambeitz-Ilankovic, L., Leucht, S., Wood, S., Davatzikos, C., Malchow, B., . . . Koutsouleris, N. (2015). Detecting neuroimaging biomarkers for schizophrenia: a meta-analysis of multivariate pattern recognition studies. *Neuropsychopharmacology, 40*(7), 1742-1751. doi:10.1038/npp.2015.22

Kandel, B. M., Avants, B. B., Gee, J. C., McMillan, C. T., Erus, G., Doshi, J., . . . Wolk, D. A. (2016). White matter hyperintensities are more highly associated with preclinical Alzheimer's disease than imaging and cognitive markers of neurodegeneration. *Alzheimers Dement (Amst), 4*, 18-27. doi:10.1016/j.dadm.2016.03.001

Karantzoulis, S., & Galvin, J. E. (2011). Distinguishing Alzheimer's disease from other major forms of dementia. *Expert Rev Neurother, 11*(11), 1579-1591. doi:10.1586/ern.11.155

Kile, S. J., & Olichney, J. M. (2007). Amyloid Clearing Immunotherapy for Alzheimer's Disease and the Risk of Cerebral Amyloid Angiopathy. *Alzheimers Dis Res J, 1*(1-2), 5-12.

Kim, J., & Fessler, J. A. (2004). Intensity-based image registration using robust correlation coefficients. *IEEE transactions on medical imaging, 23*(11), 1430-1444.

Kim, J., Krishnamurthy, N., Santini, T., Zhao, Y., Zhao, T., Bae, K. T., & Ibrahim, T. S. (2016). Experimental and numerical analysis of B1+ field and SAR with a new transmit array design for 7 T breast MRI. *Journal of Magnetic Resonance, 269*, 55-64.

Kim, J., Santini, T., Bae, K. T., Krishnamurthy, N., Zhao, Y., Zhao, T., & Ibrahim, T. S. (2017). Development of a 7 T RF coil system for breast imaging. *NMR in biomedicine, 30*(1), e3664.

Kim, T.-S., Singh, M., Sungkarat, W., Zarow, C., & Chui, H. (2000). Automatic registration of postmortem brain slices to MRI reference volume. *IEEE Transactions on Nuclear Science, 47*(4), 1607-1613.

Kinahan, P. E., & Fletcher, J. W. (2010). Positron emission tomography-computed tomography standardized uptake values in clinical practice and assessing response to therapy. *Semin Ultrasound CT MR, 31*(6), 496-505. doi:10.1053/j.sult.2010.10.001

Klunk, W. E. (2011). Amyloid imaging as a biomarker for cerebral beta-amyloidosis and risk prediction for Alzheimer dementia. *Neurobiol Aging, 32 Suppl 1*, S20-36. doi:10.1016/j.neurobiolaging.2011.09.006

Klunk, W. E., Engler, H., Nordberg, A., Wang, Y., Blomqvist, G., Holt, D. P., . . . Langstrom, B. (2004). Imaging brain amyloid in Alzheimer's disease with Pittsburgh Compound-B. *Ann Neurol, 55*(3), 306-319. doi:10.1002/ana.20009

Kohonen, T. (1990). The self-organizing map. *Proceedings of the IEEE, 78*(9), 1464-1480.

Kotsiantis, S. B., Zaharakis, I., & Pintelas, P. (2007). Supervised machine learning: A review of classification techniques. *Emerging artificial intelligence applications in computer engineering, 160*, 3-24.

Krishnamurthy, N., Santini, T., Wood, S., Kim, J., Zhao, T., Aizenstein, H. J., & Ibrahim, T. S. (2019). Computational and experimental evaluation of the Tic-Tac-Toe RF coil for 7 Tesla MRI. *PLoS One, 14*(1), e0209663.

Leite, M., Rittner, L., Appenzeller, S., Ruocco, H. H., & Lotufo, R. (2015). Etiology-based classification of brain white matter hyperintensity on magnetic resonance imaging. *J Med Imaging (Bellingham), 2*(1), 014002. doi:10.1117/1.JMI.2.1.014002

Liu, F., Zhou, L., Shen, C., & Yin, J. (2014). Multiple kernel learning in the primal for multimodal Alzheimer's disease classification. *IEEE journal of biomedical and health informatics, 18*(3), 984-990.

Liu, S., Buch, S., Chen, Y., Choi, H. S., Dai, Y., Habib, C., . . . Haacke, E. M. (2017). Susceptibility-weighted imaging: current status and future directions. *NMR Biomed, 30*(4). doi:10.1002/nbm.3552

Loeffler, D. A. (2013). Intravenous immunoglobulin and Alzheimer's disease: what now? *J Neuroinflammation, 10*, 70. doi:10.1186/1742-2094-10-70

Maani, R., Kalra, S., & Yang, Y. H. (2014). Robust volumetric texture classification of magnetic resonance images of the brain using local frequency descriptor. *IEEE Trans Image Process, 23*(10), 4625-4636. doi:10.1109/TIP.2014.2351620

Maani, R., Yang, Y. H., & Kalra, S. (2015). Voxel-based texture analysis of the brain. *PLoS One, 10*(3), e0117759. doi:10.1371/journal.pone.0117759

Magnin, B., Mesrob, L., Kinkingnehun, S., Pelegrini-Issac, M., Colliot, O., Sarazin, M., . . . Benali, H. (2009). Support vector machine-based classification of Alzheimer's disease from whole-brain anatomical MRI. *Neuroradiology, 51*(2), 73-83. doi:10.1007/s00234-008-0463-x

Manners, D. N., Parchi, P., Tonon, C., Capellari, S., Strammiello, R., Testa, C., . . . Barbiroli, B. (2009). Pathologic correlates of diffusion MRI changes in Creutzfeldt-Jakob disease. *Neurology, 72*(16), 1425-1431. doi:10.1212/WNL.0b013e3181a18846

Marcus, C., Mena, E., & Subramaniam, R. M. (2014). Brain PET in the diagnosis of Alzheimer's disease. *Clin Nucl Med, 39*(10), e413-422; quiz e423-416. doi:10.1097/RLU.0000000000000547

Mardia, K. V., & Hainsworth, T. (1988). A spatial thresholding method for image segmentation. *IEEE transactions on pattern analysis and machine intelligence, 10*(6), 919-927.

Mathotaarachchi, S., Pascoal, T. A., Shin, M., Benedet, A. L., Kang, M. S., Beaudry, T., . . . Alzheimer's Disease Neuroimaging, I. (2017). Identifying incipient dementia individuals using machine learning and amyloid imaging. *Neurobiol Aging*. doi:10.1016/j.neurobiolaging.2017.06.027

Maurer, K., Volk, S., & Gerbaldo, H. (1997). Auguste D and Alzheimer's disease. *Lancet, 349*(9064), 1546-1549. doi:10.1016/S0140-6736(96)10203-8

Meadowcroft, M. D., Connor, J. R., Smith, M. B., & Yang, Q. X. (2009). MRI and histological analysis of beta-amyloid plaques in both human Alzheimer's disease and APP/PS1 transgenic mice. *J Magn Reson Imaging, 29*(5), 997-1007. doi:10.1002/jmri.21731

Meier, I. B., Manly, J. J., Provenzano, F. A., Louie, K. S., Wasserman, B. T., Griffith, E. Y., . . . Brickman, A. M. (2012). White matter predictors of cognitive functioning in older adults. *J Int Neuropsychol Soc, 18*(3), 414-427. doi:10.1017/S1355617712000227

Miller, M. D., Paradis, C. F., Houck, P. R., Mazumdar, S., Stack, J. A., Rifai, A. H., . . . Reynolds, C. F., 3rd. (1992). Rating chronic medical illness burden in geropsychiatric practice and research: application of the Cumulative Illness Rating Scale. *Psychiatry Res, 41*(3), 237-248.

Mishra, S., Gordon, B. A., Su, Y., Christensen, J., Friedrichsen, K., Jackson, K., . . . Benzinger, T. L. S. (2017). AV-1451 PET imaging of tau pathology in preclinical Alzheimer disease: Defining a summary measure. *Neuroimage, 161*, 171-178. doi:10.1016/j.neuroimage.2017.07.050

Mitchell, T. M. (1997). *Machine Learning*: McGraw-Hill, Inc.

Moller, C., Hafkemeijer, A., Pijnenburg, Y. A. L., Rombouts, S., van der Grond, J., Dopper, E., . . . van der Flier, W. M. (2016). Different patterns of cortical gray matter loss over time in behavioral variant frontotemporal dementia and Alzheimer's disease. *Neurobiol Aging, 38*, 21-31. doi:10.1016/j.neurobiolaging.2015.10.020

Moon, T. K. (1996). The expectation-maximization algorithm. *IEEE signal processing magazine, 13*(6), 47-60.

Mosconi, L., Berti, V., Glodzik, L., Pupi, A., De Santi, S., & de Leon, M. J. (2010). Pre-clinical detection of Alzheimer's disease using FDG-PET, with or without amyloid imaging. *J Alzheimers Dis, 20*(3), 843-854. doi:10.3233/JAD-2010-091504

Mucherino, A., Papajorgji, P. J., & Pardalos, P. M. (2009). K-nearest neighbor classification *Data mining in agriculture* (pp. 83-106): Springer.

Mucke, L., & Selkoe, D. J. (2012). Neurotoxicity of amyloid beta-protein: synaptic and network dysfunction. *Cold Spring Harb Perspect Med, 2*(7), a006338. doi:10.1101/cshperspect.a006338

Myronenko, A., & Song, X. (2010). Intensity-based image registration by minimizing residual complexity. *IEEE transactions on medical imaging, 29*(11), 1882-1891.

Nelson, P. T., Alafuzoff, I., Bigio, E. H., Bouras, C., Braak, H., Cairns, N. J., . . . Beach, T. G. (2012). Correlation of Alzheimer disease neuropathologic changes with cognitive status: a review of the literature. *J Neuropathol Exp Neurol, 71*(5), 362-381. doi:10.1097/NEN.0b013e31825018f7

Nelson, P. T., Braak, H., & Markesbery, W. R. (2009). Neuropathology and cognitive impairment in Alzheimer disease: a complex but coherent relationship. *J Neuropathol Exp Neurol, 68*(1), 1-14. doi:10.1097/NEN.0b013e3181919a48

Noh, Y., Seo, S. W., Jeon, S., Lee, J. M., Kim, J. H., Kim, G. H., . . . Na, D. L. (2014). White matter hyperintensities are associated with amyloid burden in APOE4 non-carriers. *J Alzheimers Dis, 40*(4), 877-886. doi:10.3233/JAD-130461

Nolen-Hoeksema, S., Morrow, J., & Fredrickson, B. L. (1993). Response styles and the duration of episodes of depressed mood. *J Abnorm Psychol, 102*(1), 20-28.

O'Brien, R. J., & Wong, P. C. (2011). Amyloid precursor protein processing and Alzheimer's disease. *Annu Rev Neurosci, 34*, 185-204. doi:10.1146/annurev-neuro-061010-113613

Oguz, I., Yaxley, R., Budin, F., Hoogstoel, M., Lee, J., Maltbie, E., . . . Crews, F. T. (2013). Comparison of magnetic resonance imaging in live vs. post mortem rat brains. *PLoS One, 8*(8), e71027. doi:10.1371/journal.pone.0071027

Okamura, N., & Yanai, K. (2010). Florbetapir (18F), a PET imaging agent that binds to amyloid plaques for the potential detection of Alzheimer's disease. *IDrugs, 13*(12), 890-899.

Oppedal, K., Eftestol, T., Engan, K., Beyer, M. K., & Aarsland, D. (2015). Classifying dementia using local binary patterns from different regions in magnetic resonance images. *Int J Biomed Imaging, 2015*, 572567. doi:10.1155/2015/572567

Panza, F., Frisardi, V., Imbimbo, B. P., Seripa, D., Solfrizzi, V., & Pilotto, A. (2011). Monoclonal antibodies against beta-amyloid (Abeta) for the treatment of Alzheimer's disease: the Abeta target at a crossroads. *Expert Opin Biol Ther, 11*(6), 679-686. doi:10.1517/14712598.2011.579099

Park, J. H., Seo, S. W., Kim, C., Kim, S. H., Kim, G. H., Kim, S. T., . . . Na, D. L. (2014). Effects of cerebrovascular disease and amyloid beta burden on cognition in subjects with subcortical vascular cognitive impairment. *Neurobiol Aging, 35*(1), 254-260. doi:10.1016/j.neurobiolaging.2013.06.026

Pedregosa, F., Varoquaux, G., Gramfort, A., Michel, V., Thirion, B., Grisel, O., . . . Dubourg, V. (2011). Scikit-learn: Machine learning in Python. *Journal of machine learning research, 12*(Oct), 2825-2830.

Perl, D. P. (2010). Neuropathology of Alzheimer's disease. *Mt Sinai J Med, 77*(1), 32-42. doi:10.1002/msj.20157

Pluim, J. P., Maintz, J. A., & Viergever, M. A. (2003). Mutual-information-based registration of medical images: a survey. *IEEE transactions on medical imaging, 22*(8), 986-1004.

Quinlan, J. R. (1986). Induction of decision trees. *Machine learning, 1*(1), 81-106.

Quinlan, J. R. (1996). *Bagging, boosting, and C4. 5.* Paper presented at the AAAI/IAAI, Vol. 1.

Relkin, N. (2014). Intravenous immunoglobulin for Alzheimer's disease. *Clin Exp Immunol, 178 Suppl 1*, 27-29. doi:10.1111/cei.12500

Richard, E., Schmand, B. A., Eikelenboom, P., Van Gool, W. A., & Alzheimer's Disease Neuroimaging, I. (2013). MRI and cerebrospinal fluid biomarkers for predicting progression to Alzheimer's disease in patients with mild cognitive impairment: a diagnostic accuracy study. *BMJ Open, 3*(6). doi:10.1136/bmjopen-2012-002541

Rudko, D. A., Solovey, I., Gati, J. S., Kremenchutzky, M., & Menon, R. S. (2014). Multiple sclerosis: improved identification of disease-relevant changes in gray and white matter by using susceptibility-based MR imaging. *Radiology, 272*(3), 851-864. doi:10.1148/radiol.14132475

Saaidi, R., Toufique, Y., Merouani, A., Elbouhali, O., & El Moursli, R. C. (2016). A Monte Carlo Study of Clinical PET ECAT EXACT HR+ Using GATE *Basic Concepts in Nuclear Physics: Theory, Experiments and Applications* (pp. 223-225): Springer.

Santini, T., Kim, J., Wood, S., Krishnamurthy, N., Farhat, N., Maciel, C., . . . Ibrahim, T. S. (2018). A new RF transmit coil for foot and ankle imaging at 7T MRI. *Magnetic resonance imaging, 45*, 1-6.

Santini, T., Zhao, Y., Wood, S., Krishnamurthy, N., Kim, J., Farhat, N., . . . Zhao, T. (2018). In-vivo and numerical analysis of the eigenmodes produced by a multi-level Tic-Tac-Toe head transmit array for 7 Tesla MRI. *PLoS One, 13*(11), e0206127.

Scheltens, P., Barkhof, F., Valk, J., Algra, P. R., van der Hoop, R. G., Nauta, J., & Wolters, E. C. (1992). White matter lesions on magnetic resonance imaging in clinically diagnosed Alzheimer's disease. Evidence for heterogeneity. *Brain, 115 (Pt 3)*, 735-748.

Schmierer, K., Scaravilli, F., Barker, G. J., Gordon, R., MacManus, D. G., & Miller, D. H. (2003). Stereotactic co-registration of magnetic resonance imaging and histopathology in post-mortem multiple sclerosis brain. *Neuropathol Appl Neurobiol, 29*(6), 596-601.

Scholkopf, B., & Smola, A. J. (2001). *Learning with Kernels: Support Vector Machines, Regularization, Optimization, and Beyond*: MIT Press.

Seo, S. W., Ayakta, N., Grinberg, L. T., Villeneuve, S., Lehmann, M., Reed, B., . . . Rabinovici, G. D. (2017). Regional correlations between [(11)C]PIB PET and post-mortem burden of amyloid-beta pathology in a diverse neuropathological cohort. *Neuroimage Clin, 13*, 130-137. doi:10.1016/j.nicl.2016.11.008

Sepehry, A. A., Lang, D., Hsiung, G. Y., & Rauscher, A. (2016). Prevalence of Brain Microbleeds in Alzheimer Disease: A Systematic Review and Meta-Analysis on the Influence of Neuroimaging Techniques. *AJNR Am J Neuroradiol, 37*(2), 215-222. doi:10.3174/ajnr.A4525

Serrano-Pozo, A., Frosch, M. P., Masliah, E., & Hyman, B. T. (2011). Neuropathological alterations in Alzheimer disease. *Cold Spring Harb Perspect Med, 1*(1), a006189. doi:10.1101/cshperspect.a006189

Shafarenko, L., Petrou, M., & Kittler, J. (1997). Automatic watershed segmentation of randomly textured color images. *IEEE transactions on Image Processing, 6*(11), 1530-1544.

Smith, C. D., Johnson, E. S., Van Eldik, L. J., Jicha, G. A., Schmitt, F. A., Nelson, P. T., . . . Wellnitz, C. V. (2016). Peripheral (deep) but not periventricular MRI white matter hyperintensities are increased in clinical vascular dementia compared to Alzheimer's disease. *Brain Behav, 6*(3), e00438. doi:10.1002/brb3.438

Sojkova, J., & Resnick, S. M. (2011). In vivo human amyloid imaging. *Curr Alzheimer Res, 8*(4), 366-372.

Spasov, S., Passamonti, L., Duggento, A., Lio, P., & Toschi, N. (2018). A parameter-efficient deep learning approach to predict conversion from mild cognitive impairment to Alzheimer's disease within three years. *bioRxiv*, 383687. doi:10.1101/383687

Sperling, R. A., Aisen, P. S., Beckett, L. A., Bennett, D. A., Craft, S., Fagan, A. M., . . . Phelps, C. H. (2011). Toward defining the preclinical stages of Alzheimer's disease: recommendations from the National Institute on Aging-Alzheimer's Association workgroups on diagnostic guidelines for Alzheimer's disease. *Alzheimers Dement, 7*(3), 280-292. doi:10.1016/j.jalz.2011.03.003

Suoranta, S., Holli-Helenius, K., Koskenkorva, P., Niskanen, E., Kononen, M., Aikia, M., . . . Vanninen, R. (2013). 3D texture analysis reveals imperceptible MRI textural alterations in the thalamus and putamen in progressive myoclonic epilepsy type 1, EPM1. *PLoS One, 8*(7), e69905. doi:10.1371/journal.pone.0069905

Sutton, R. S., & Barto, A. G. (1998). *Introduction to Reinforcement Learning*: MIT Press.

Tang, E. Y., Harrison, S. L., Errington, L., Gordon, M. F., Visser, P. J., Novak, G., . . . Stephan, B. C. (2015). Current Developments in Dementia Risk Prediction Modelling: An Updated Systematic Review. *PLoS One, 10*(9), e0136181. doi:10.1371/journal.pone.0136181

Tapiola, T., Alafuzoff, I., Herukka, S. K., Parkkinen, L., Hartikainen, P., Soininen, H., & Pirttila, T. (2009). Cerebrospinal fluid {beta}-amyloid 42 and tau proteins as biomarkers of Alzheimer-type pathologic changes in the brain. *Arch Neurol, 66*(3), 382-389. doi:10.1001/archneurol.2008.596

Ten Kate, M., Redolfi, A., Peira, E., Bos, I., Vos, S. J., Vandenberghe, R., . . . Barkhof, F. (2018). MRI predictors of amyloid pathology: results from the EMIF-AD Multimodal Biomarker Discovery study. *Alzheimers Res Ther, 10*(1), 100. doi:10.1186/s13195-018-0428-1

Thompson, C. M., & Shure, L. (1995). *Image Processing Toolbox: For Use with MATLAB;[user's Guide]*: MathWorks.

Tong, S., Alessio, A. M., & Kinahan, P. E. (2010). Image reconstruction for PET/CT scanners: past achievements and future challenges. *Imaging Med, 2*(5), 529-545. doi:10.2217/iim.10.49

van Dyck, C. H. (2018). Anti-Amyloid-beta Monoclonal Antibodies for Alzheimer's Disease: Pitfalls and Promise. *Biol Psychiatry, 83*(4), 311-319. doi:10.1016/j.biopsych.2017.08.010

Vemuri, N. V., Karanam, L. S. P., Manchikanti, V., Dandamudi, S., Puvvada, S. K., & Vemuri, V. K. (2017). Imaging review of cerebrospinal fluid leaks. *Indian J Radiol Imaging, 27*(4), 441-446. doi:10.4103/ijri.IJRI_380_16

Villemagne, V. L. (2016). Amyloid imaging: Past, present and future perspectives. *Ageing Res Rev, 30*, 95-106. doi:10.1016/j.arr.2016.01.005

Walhovd, K. B., Fjell, A. M., Brewer, J., McEvoy, L. K., Fennema-Notestine, C., Hagler, D. J., Jr., . . . Alzheimer's Disease Neuroimaging, I. (2010). Combining MR imaging, positron-emission tomography, and CSF biomarkers in the diagnosis and prognosis of Alzheimer disease. *AJNR Am J Neuroradiol, 31*(2), 347-354. doi:10.3174/ajnr.A1809

Wang, J., Shen, X., & Pan, W. (2007). On transductive support vector machines.

Wang, W.-H., & Chen, Y.-C. (1997). Image registration by control points pairing using the invariant properties of line segments. *Pattern Recognition Letters, 18*(3), 269-281.

Wattjes, M. P. (2011). Structural MRI. *Int Psychogeriatr, 23 Suppl 2*, S13-24. doi:10.1017/S1041610211000913

Wen, W., & Sachdev, P. S. (2004). Extent and distribution of white matter hyperintensities in stroke patients: the Sydney Stroke Study. *Stroke, 35*(12), 2813-2819. doi:10.1161/01.STR.0000147034.25760.3d

Weninger, S., Carrillo, M. C., Dunn, B., Aisen, P. S., Bateman, R. J., Kotz, J. D., . . . Welsh-Bohmer, K. A. (2016). Collaboration for Alzheimer's Prevention: Principles to guide data and sample sharing in preclinical Alzheimer's disease trials. *Alzheimers Dement, 12*(5), 631-632. doi:10.1016/j.jalz.2016.04.001

Weygandt, M., Hackmack, K., Pfuller, C., Bellmann-Strobl, J., Paul, F., Zipp, F., & Haynes, J. D. (2011). MRI pattern recognition in multiple sclerosis normal-appearing brain areas. *PLoS One, 6*(6), e21138. doi:10.1371/journal.pone.0021138

Woods, R. P., Mazziotta, J. C., & Cherry, S. R. (1993). MRI-PET registration with automated algorithm. *J Comput Assist Tomogr, 17*(4), 536-546.

Wu, M., Rosano, C., Butters, M., Whyte, E., Nable, M., Crooks, R., . . . Aizenstein, H. J. (2006). A fully automated method for quantifying and localizing white matter hyperintensities on MR images. *Psychiatry Res, 148*(2-3), 133-142. doi:10.1016/j.pscychresns.2006.09.003

Wu, M., Rosano, C., Butters, M., Whyte, E., Nable, M., Crooks, R., . . . Aizenstein, H. J. (2006). A fully automated method for quantifying and localizing white matter hyperintensities on MR images. *Psychiatry Research: Neuroimaging, 148*(2-3), 133-142.

Yasuno, F., Kazui, H., Morita, N., Kajimoto, K., Ihara, M., Taguchi, A., . . . Nagatsuka, K. (2017). Use of T1-weighted/T2-weighted magnetic resonance ratio to elucidate changes due to amyloid beta accumulation in cognitively normal subjects. *Neuroimage Clin, 13*, 209-214. doi:10.1016/j.nicl.2016.11.029

Yoshita, M., Fletcher, E., Harvey, D., Ortega, M., Martinez, O., Mungas, D. M., . . . DeCarli, C. S. (2006). Extent and distribution of white matter hyperintensities in normal aging, MCI, and AD. *Neurology, 67*(12), 2192-2198. doi:10.1212/01.wnl.0000249119.95747.1f

Yushkevich, P. A., Piven, J., Hazlett, H. C., Smith, R. G., Ho, S., Gee, J. C., & Gerig, G. (2006). User-guided 3D active contour segmentation of anatomical structures: significantly improved efficiency and reliability. *Neuroimage, 31*(3), 1116-1128.

Zacharaki, E. I., Wang, S., Chawla, S., Soo Yoo, D., Wolf, R., Melhem, E. R., & Davatzikos, C. (2009). Classification of brain tumor type and grade using MRI texture and shape in a machine learning scheme. *Magn Reson Med, 62*(6), 1609-1618. doi:10.1002/mrm.22147

Zhang, Y., Moore, G. R., Laule, C., Bjarnason, T. A., Kozlowski, P., Traboulsee, A., & Li, D. K. (2013). Pathological correlates of magnetic resonance imaging texture heterogeneity in multiple sclerosis. *Ann Neurol, 74*(1), 91-99. doi:10.1002/ana.23867